Electrospray Ionization Source for the Deposition of Large Molecules and Clusters

vorgelegt von

FRANK LOUIS STADLER

Zusammenfassung

Für gewöhnlich erfolgt das Aufbringen kleiner organischer Moleküle auf ein sich im Ultrahochvakuum (UHV: ultra high vacuum) befindendes Substrat mittels organischer Molekularstrahlepitaxie (OMBE: organic molecular beam epitaxy). Jedoch ist mit dieser Technik die Deposition großer biologischer Moleküle nur bedingt möglich, da diese oft zu fragil sind um zerstörungsfrei sublimiert zu werden, was sich in einem zu niedrigen Dampfdruck biologischer Substanzen äußert.

Diese Problematik bildet das thematische Umfeld dieser Arbeit, die sich mit der Entwicklung, dem Aufbau, und der Charakterisierung einer neuartigen Depositionsquelle zur zerstörungsfreien in-vacuo Depostion empfindlicher organischer und biologischer Substanzen beschäftigt. Unter Verwendung der Elektrospray Ionisations Technik (ESI-Technik) werden hierbei anfänglich in Lösung vorhandene Analytmoleküle auf sanfte Weise in die ionisierte Gasphase überführt, anschließend schrittweise in stetig besser werdende Umgebungsvakua transportiert, sowie abschließend auf einem Substrat deponiert.

Für den Transport der Analytionen in Richtung Substrat, der über mehrere differentielle Pumpstufen hinweg erfolgt, kommen sowohl elektrostatische als auch elektrodynamische Komponenten zum Einsatz. Ihre gleichzeitig ionenführende als auch strahlformende Wirkung ermöglicht es, nicht zu vermeidende Transportverluste zu minimieren. Unmittelbar vor der Deposition der Ionen auf der Substratoberfläche findet eine letzte elektrostatische Abbremsung statt, welche ein zerstörungsfreies Aufbringen der Analytionen erlaubt. Für das Erreichen der langfristigen Zielsetzung, einer zerstörungsfreien Deposition empfindlicher Analyte unter wohldefinierten UHV Umgebungsbedingungen, sind allerdings noch zwei weitere Pumpstufen nötig, wobei die UHV Präparationskammer selbst als abschließende Pumpstufe fungiert. Jedoch

können mit dem gegenwärtigen Stadium der ESI Depositionsquelle bereits erste Depositionsexperimente durchgeführt werden.

Diese Arbeit gliedert sich wie folgt: An eine kurze Einführung in die Thematik der ESI-Technik, in der sowohl die konzeptionellen Grundlagen als auch die im ESI-Prozess zur Freisetzung der Analytionen verantwortlichen Prozesse vorgestellt werden, schließt sich die Charakterisierung der Depositionsquelle an. Dieser Abschnitt gibt einen Überblick auf das technische Gesamtkonzept der ESI Depositionsapparatur, und beinhaltet die detailierte Charakterisierung des ESI-Kopfes sowie der nachfolgenden ionenstrahlformenden Stufe. Es werden die jeweiligen Funktionsprinzipien diskutiert, und die Abhängigkeit der Strahlintensität von verschiedenen Parametern wie anliegenden Hoch- und Steuerspannungen, oder den in Teilbereichen der ionenstrahlformenden Stufe vorliegenden Drücken vorgestellt.

Der experimentelle Ergebnisteil der Arbeit demonstriert die Umsetzung der neuartigen in-vacuo ESI Deposition am Beispiel mehrerer kolloidaler, organischer und biologischer Analyte (Au colloid, Rhodamine 6G, Bovine Serum Albumin, Horse Spleen Ferritin). Diese Substanzen wurden unter Verwendung der ESI Depositionsquelle auf ein leitfähiges Substrat bei $1 \cdot 10^{-6}$ mbar Hintergrunddruck aufgebracht, und anschließend unter Umgebungsbedingungen an Atmosphäre mittels Rasterkraftmikroskopie (AFM: atomic froce microscopy) charakterisiert. Ein Vergleich der Morphologie der ESI-Proben, mit Proben die in flüssiger Phase adsorbiert wurden, zeigt, daß das Aufbringen lösungsmittelfreier Analytionen unter Verwendung der ESI Depositionsquelle große Vorteile aufweist.

Um zu demonstrieren, welche Vielfalt an Informationen gewonnen werden kann, wenn man von AFM unter Umgebungsbedingungen zur Rastertunnelmikroskopie (STM: scanning tunneling microscopy) unter wohldefinierten UHV Bedingungen übergeht, werden im abschließende Kapitel in-vacuo STM Untersuchungen an einem kleinen biologischen Molekül vorgestellt, welches noch mittels OMBE auf eine Einkristalloberfläche aufgebracht werden kann, aber bereits nahe am Limit dieser Technik liegt. Genauer untersucht werden hierbei die Wechselwirkungen der Adsorbatmoleküle untereinander, zwischen Adsorbat und Substrat, sowie der Einfluß der Chiralität des biologischen Adsorbates auf die Ausbildung supramolekularer Struk-

turen. Anhand dieses Experiments wird gezeigt, welche vielfältigen experimentellen Möglichkeiten bereits eine konventionelle Deposition kleiner biologischer Moleküle in Kombination mit einer rastersondenmikroskopischen Charakterisierung der Proben bietet. Sobald die ESI Depositionsquelle komplett aufgebaut und mit der UHV Präparationskammer verbunden ist, kann die gleiche Art von Experimenten an komplexeren Molekülen durchgeführt werden.

Einerseits ist der Einsatzbereich einer sanften, auf der ESI-Technik basierenden, UHV Depositionsquelle nahezu maßgeschneidert für den Forschungszweig der biologischen Oberflächenwissenschaften, andererseits wird diese neuartige Depositionsquelle immer dann zum Einsatz kommen, wenn empfindliche Moleküle nicht durch thermisches Verdampfen auf eine Oberfläche aufgebracht werden können.

Contents

Chapter 1

Motivation and Introduction

The maturing field of biological surface science [1] aims for an appropriate deposition technique enabling the soft deposition of large but fragile biological molecules onto atomically defined and chemically clean substrates. Such a technique would allow the enlargement of the research field of supramolecular nanostructures at surfaces toward biologically significant adsorbate-substrate systems. Moreover, it would permit the investigation of fundamental problems of the interaction of biomolecules with surfaces, such as biological self-recognition phenomena as well as the conformation modifications of proteins induced by co-deposits and/or protein-substrate interactions, being examined in a fully controlled environment.

On one side, conventional liquid phase based deposition techniques are able to accomplish a soft deposition, but on the other side, all fundamental interactions such as the interaction of the adsorbate with the underlying substrate are at least partially mediated by remaining solvent molecules. Regarding the desired purity of the deposition environment, **o**rganic **m**olecular **b**eam **e**pitaxy (**OMBE**) is known to be well defined, but is problematic for larger biological molecules due to the thermal nature of the underlying analyte sublimation process.

The absence of a deposition technique circumventing this thermal limitation, but using an **u**ltra **h**igh **v**acuum (**UHV**) as deposition environment, is a problem which is left to the scientific community. Some attempts have been made in this direction: A first is the 'wire deposition method', where a small amount of analyte powder is put on a filament, that is heated via a short current pulse that desorbes the analyte

molecules. This technique is only a small variant of OMBE and cannot extend the class of amenable analytes much further. The (liquid) pulse injection method [2] is another attempt, where solvent and analyte molecules are simultaneously provided to and deposited onto the substrate, which is disadvantageous for a clear division between the possible origins of an observed effect.

In contrast, the field of **m**ass **s**pectrometry (**MS**) offers technological solutions of the volatilization and ionization problem of large biomolecules: **L**aser **I**nduced **L**iquid **B**eam **I**onization/**D**esorption (**LILBID**) [3, 4], **M**atrix **A**ssisted **L**aser **D**esorption/**I**onization (**MALDI**) [5], and **E**lectro**s**pray **I**onization (**ESI**) [6]. Unlike the (liquid) pulse injection method mentioned above, these techniques allow the separation of neutral solvent molecules from the desired charged analyte ions. Moreover, they allow the full control over the composition of the analyte ion beam that might be used for deposition experiments. Therefore, it is natural to extend these MS techniques toward new deposition techniques that are able to achieve the challenging goal of a destruction-free deposition of large biomolecules.

We decided for ESI as linking technique between the analyte molecules in solution and the free gas phase ions (see section 3.1) because of its very broad range of applicability that extends even beyond the research field of (large) biomolecules. In addition, the ESI technique is relatively simple when compared with e.g. MALDI, where a laser is needed for the ionization of the analyte.

Initial experiments by J. Zeleny (1917) preceded the first description of electrohydrodynamic dispersion of liquids by M. Dole et al. (1968) for the use as electrospray ionization method[1]. Based on their observations, M. L. Aleksandrov et al. and J. B. Fenn et al. contributed the most to the development and establishment of the ESI technique [7]. Within the last decades the steady progress in the field of ESI-MS lead to a revolution in the analysis of biological macromolecules, that has been recognized by awarding J. B. Fenn with the Nobel Prize in Chemistry 2002 for the invention of ESI-MS.

The possibility of transforming ESI into a deposition technique has been recently demonstrated by Z. Ouyang et al. [8] who showed that a gentle deposition of protein

---

[1]For a brief historical perspective on the early days of ESI-MS see [7].

ions after ESI and **t**ime-**o**f-**f**light (**TOF**) mass separation is possible while keeping them intact. Our goal is one step further: "Soft-landing and characterization of thermolabile analytes under well defined UHV conditions." Figure 1.1 depicts the corresponding underlying technological challenge. At ambient pressure conditions an
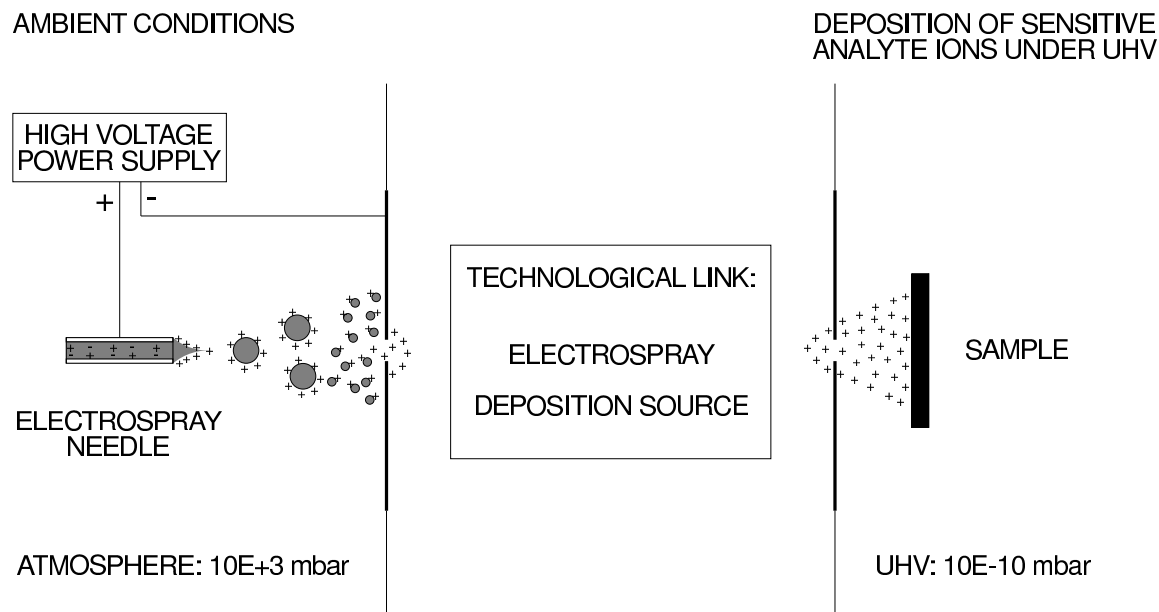
AMBIENT CONDITIONS

DEPOSITION OF SENSITIVE
ANALYTE IONS UNDER UHV

HIGH VOLTAGE
POWER SUPPLY

+ -

TECHNOLOGICAL LINK:

ELECTROSPRAY

DEPOSITION SOURCE

SAMPLE

ELECTROSPRAY
NEEDLE

ATMOSPHERE: 10E+3 mbar

UHV: 10E-10 mbar

Figure 1.1: Schematic drawing of the ESI-deposition circuit: After the generation of a charged aerosol and successive ESI in atmospheric conditions, the electrospray deposition source acts as vacuum technological link between atmosphere and UHV, where the deposition of the charged analyte ions takes place.

aerosol of charged droplets is created by means of electrohydrodynamic dispersion of the analyte spray solution. This is followed by the release of in general multiply charged analyte ions which are vaporized into the atmospheric gas phase during the course of ESI. The right hand side of figure 1.1 shows the deposition of analyte ions onto the substrate, e.g. an atomically defined single crystal surface within an UHV environment.

In order to deposit the analyte ions successfully on the substrate, in total 13 orders of magnitude in pressure have to be bridged between the region of nebulization at atmospheric pressure and the UHV-side deposition onto the substrate. This is accomplished by the ESI deposition source, also operating as vacuum-technological interface. It was the task of my PhD work to solve this technological challenge.

After a short motivation of the conception of the ESI deposition apparatus (chapter 2) and an introduction to the fundamentals of ESI (chapter 3), the design principles and the characterization of the ESI deposition source is presented (chapter 4). This is followed by several examples of the electrospray deposition of biological analytes onto conductive substrates (chapter 5). Finally, an UHV **s**canning **t**unneling **m**icroscopy (**STM**) study of a small biomolecule deposited by conventional means of OMBE is presented (chapter 6), giving a taste of what will be possible once the ESI-based UHV deposition source is interfaced to the UHV system.

Chapter 2

Conception of the Electrospray Deposition Apparatus

In order to reach the goal of a soft-landing of sensitive e.g. biological analytes under well defined UHV conditions a novel kind of deposition apparatus is needed that circumvents the intrinsic thermal limitation of an OMBE-based deposition technique. Due to the desired purity of the sample preparation process, the analyte deposition as well as the analysis of the adsorbate-substrate system have to be performed within a well defined environment.

As already mentioned in the chapter above, ESI is well known as soft ionization technique with a very broad range of application in the field of MS [9]. Hence, although technological challenging, it is natural to extend this technology to an UHV deposition technique that permits the destruction-free deposition of sensitive analytes on chemically clean substrates.

Figure 2.1 provides an overview on our novel ESI deposition apparatus that is composed of three main components: the ESI deposition source, the UHV deposition chamber, and the sample analysis chamber. The ESI deposition source consists of the ESI-head, the ion beam formation stage, the **o**rthogonal–**TOF** (**o–TOF**) chamber, as well as a further differential pumping stage that connects the vacuum of the TOF chamber with the UHV of the deposition chamber.

In our experimental setup, a syringe pump is used to supply the analyte solution to the ESI-needle of the ESI-head where the spray solution is electrohydrodynamically
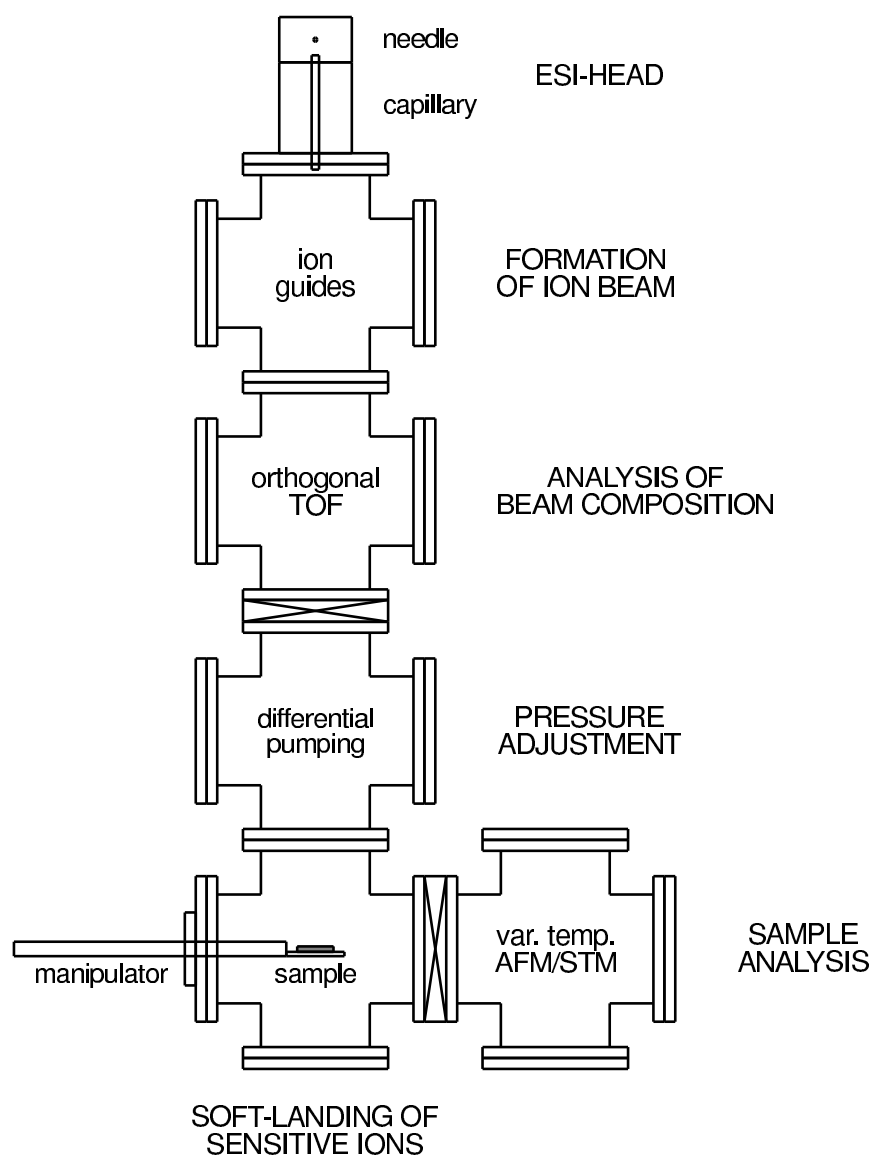
Figure 2.1: Schematic top view of the ESI deposition apparatus for the soft-landing of sensitive analyte ions under UHV conditions.

dispersed and the analyte ions are released during the ESI-process (see section 3.1). A glass capillary is utilized to connect the atmospheric side of the ESI-head to the 1st pumping stage of the following beam formation stage and to transport the analyte ions. There, after the in-vacuum expansion into the 1st pumping stage, the angular as well as energetic definition of the ion beam is accomplished by means of several electrostatic and electrodynamic components inside the beam formation stage[1]. Simultaneously to the formation of the ion beam the background pressure is gradually decreased by means of differential pumping. The following TOF chamber is already in place while the o–TOF that will be used for the analysis of the composition of the ion beam is still under assembly. The pressure adjustment chamber, next in downstream direction, is needed for vacuum reasons and will interface the ESI deposition source with the UHV deposition chamber. Detailed information on the conception and the working principles of the ESI deposition source is provided in chapter 4.

Inside the deposition chamber, a final deceleration of the analyte ions will take place in front of the substrate that permits the soft-landing of the analyte onto e.g. a single crystal surface. After the sample preparation is finished, a cryogenic manipulator is used to transfer the sample into the UHV analysis chamber. The analysis chamber comprises a commercial variable temperature AFM/STM of Omicron Nanotechnology GmbH that is used for the in-situ scanning probe investigation of the sample. The deposition and analysis chamber form an independent two-chamber system being described in more detail in the following section.

2.1 Apparative Aspects: Deposition and Analysis Chamber

The initial part of my PhD has been devoted to the design and setup of an UHV system for the preparation and characterization of single crystal surfaces. Figure 2.2 shows a picture of this two-chamber system that in the future will be directly connected to the ESI deposition source. The spherical chamber depicted on the left will

---

[1]The detailed construction design of the ESI-head and the beam formation stage is provided in chapter 4.
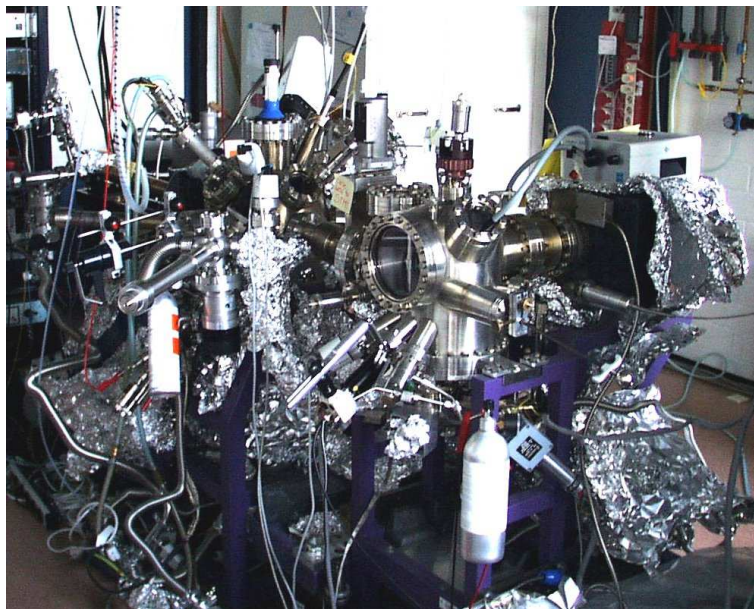
Figure 2.2: Photograph of the two-chamber system used for sample preparation (left) and sample characterization by means of AFM/STM (right).

represent the final component of the whole ESI differential pumping system and will house the single crystal samples on which the analyte ion beam will be deposited (see figure 4.1). It also acts as a preparation chamber and is equipped with a wobble stick for sample handling, a differentially pumped and cryogenic UHV manipulator for the positioning and the transfer of samples, a cold cathode pressure gauge, an ion gun with an Ar gas-inlet for substrate sputtering, a quadrupole mass spectrometer for residual gas analysis and deposition control, and several Knudsen cells and electron beam UHV evaporators. The maintenance of a base vacuum of $\sim 2 \cdot 10^{-10}$ mbar is assured by the combined action of a turbomolecular pump (TP 361, Pfeiffer, $400\ \frac{l}{s}$) and an ion pump (PID 400, Meca 2000, $400\ \frac{l}{s}$) and is supported by an integrated Ti sublimation pump.

Special features of this preparation chamber are two homemade load- and park-locks that, in combination with the self-designed manipulator head, provide excellent sample handling and vacuum-side storage possibilities for up to 4 single crystals. All components are adapted to the sample holder geometry of Omicron Nanotechnology GmbH, utilized in the variable temperature AFM/STM (see below). Cooling and resistive heating type sample holders are available, ranging in their operational

temperature between $25 - 300$ K and $45 - 750$ K, respectively.

The manipulator head was designed to be appropriate for the electrospray deposition of analyte ions being soft-landed on the single crystal substrate which is held by the sample plate (see figure 2.3). Three metal shields, whose purpose is to produce a

Figure 2.3: A heating type sample holder together with the shielded head of the manipulator are shown. The central shield can be slid laterally to insert the sample plate and to directly access the surface during sample preparation. The sliding is done by means of a wobble stick that grabs the central protruding pin.

well defined electrostatic potential environment were integrated in the manipulator head. While the outer shields are fixed directly to the head, the inner shield - provided with a square hole just above the sample location - can be moved laterally by means of the wobble stick that is used for handling the sample holders. This shield will be placed over the sample only during ESI deposition, while for sample preparation (cleaning of the sample by Ar^+ bombardment) or ordinary MBE and OMBE deposition, it remains on the side in order to allow full access to the surface. The surface of the sample crystal protrudes over the metal coated ceramic plate on top of the sample plate, allowing a better substrate preparation during Ar^+ bombardment due to the improved spatial accessability. Each single metal piece of the manipulator is independently connected, and electrically isolated from neighboring metal pieces up to voltage differences of 1.0 kV. Although the design of the manipulator is quite

compact, it is still possible to integrate further grid and lens elements, which might be needed for a final decelerating ion optics, in order to accomplish the soft-landing of the analyte ions onto the substrate.

The analysis chamber comprises a commercial variable temperature AFM/STM from Omicron Nanotechnology GmbH, with an integrated in-vacuo exchange possibility between both operation modes. This is enabled by a simple tip/cantilever exchange mechanism in combination with a retractable vacuum-side carousel, in which samples, STM tips, and AFM cantilevers are stored. The AFM/STM is equipped with a very efficient eddy-current damping system and, additionally, the whole chamber rests on a passive damping support system, improving the mechanical noise rejection and therefore the imaging stability.

When utilizing a resistive heating type sample holder and LHe as cyro-liquid, sample temperatures down to ~ 45 K can be reached inside the AFM/STM (down to ~ 130 K in the case of LN_2 as cryo-liquid). After baking of the analysis chamber, it is possible to reach a base pressure of $\sim 2 \cdot 10^{-10}$ mbar, which is maintained by means of a single ion pump (Starcell, Varian, 150 $\frac{l}{s}$).

In the future, the deposition and the analysis chamber could be mechanically decoupled after the preparation and the in-vacuo transfer of the sample, in order to protect the AFM/STM measurements from vibrations originating from the ESI deposition source. This will be done by means of an independently pumped T-shaped chamber that connects the preparation and the analysis chamber and that will be delimited by two gate valves. At present, since the UHV-ESI deposition source is still not fully operative, it is sufficient to connect the preparation and the analysis chamber by means of a simple bellows and a single gate valve (see figure 2.2). These two chambers form an independent system.

Chapter 3

Electrospray Ionization: An Introduction

3.1 Electrospray Ionization in a Nutshell

Electrospray Ionization (ESI) denotes the generation of free gas phase analyte ions from a diluted polar solution of sample molecules by electrohydrodynamic means. The corresponding mechanism is schematically shown in figure 3.1. In ESI a constant flow of diluted analyte solution is fed to e.g. a metal capillary, also called ESI-needle. A high voltage (typically $2 - 5$ kV) is applied between the capillary and a counter electrode, resulting in an inhomogeneous electrical field that separates solvated anions and cations already in solution. Moreover, the applied voltage results in a charged surface of the forming liquid meniscus at the tip of the ESI-needle. From a certain voltage on, the electrostatic forces become so strong that the meniscus starts to emit a fine liquid jet which subsequently disintegrates into a mist of charged droplets.

If we neglect the influence of gravity, the trajectories of the charged aerosol particles follow the local electric field lines pointing in the direction of the counter electrode. Due to evaporation of neutral solvent molecules a shrinkage of the droplets takes place[1] [10, 11]. Since the excess charge on the droplets is located at their surface, the reduction of the droplet diameter leads to a continuous increase of their

---

[1]Various types of electrospray sources support the solvent evaporation by means of a hot (countercurrent) flow of a dry inert gas [9], usually nitrogen.
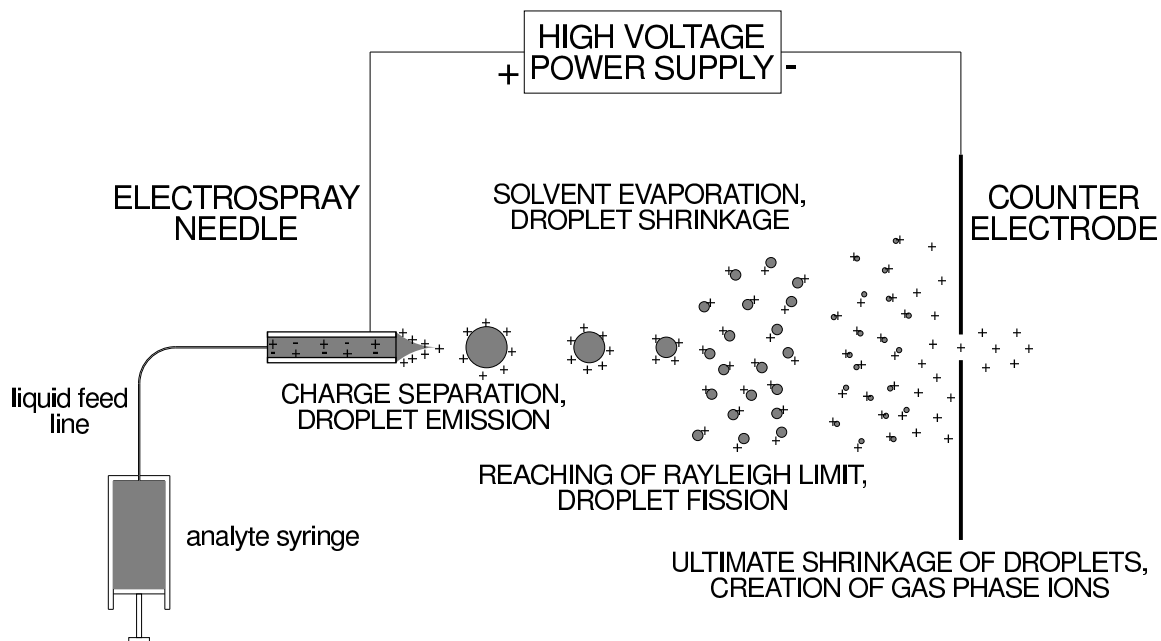
Figure 3.1: Schematic representation of the electrospray mechanism. Droplet shrinkage and repeated fission leads to free gas phase ions under atmospheric conditions.

surface charge density. At the point when the surface tension is no longer able to compensate the repulsive Coulomb interactions of the additional surface charges, the Rayleigh limit is reached [10, 11]. Thereafter, in order to minimize its energy, the primary droplet releases several smaller offspring droplets that carry just a small percentage of the primary droplet's mass but a high percentage of its charge. The repeated shrinkage and fission of all released generations of offspring droplets finally leads to the creation of free gas phase ions from the diluted analyte solution.

It should be noted that all ions present in the spray solution, including analyte ions and solvent impurities, compete with each other during the final stages of ion release. Consequently, the final population of gas phase ions will be a mixture of all these species.

3.2 Technological Basics and Fundamentals of ESI

A first classification of ESI sources utilized in practice can be done according to the way the analyte solution is supplied to the ESI-needle: either on-line[2] or off-line. Two important examples of on-line ES sources are the so-called "sheath flow capillary ion source" and "pneumatically assisted ES" [10]. In the first case, a smaller (inner) capillary carries the analyte solution, while a second (outer) coaxial capillary supplies the sheath liquid. Both liquids mix at the point of ES formation if the protrusion of the inner over the outer capillary is properly adjusted. Typical flow rates are $0.25 - 1 \frac{\mu l}{\min}$ for the analyte solution and $3 - 5 \frac{\mu l}{\min}$ for the sheath liquid [10]. In the case of pneumatically assisted ES, the outer capillary carries a flowing stream of inert gas (usually nitrogen) that supports the dispersion of the analyte solution transported by the inner capillary. Pneumatically assisted ES can be regarded as the most rugged of all ES variants, as a dispersion of sample liquid is achieved regardless of its composition and within a very broad range of flow rates. Typical analyte flow rates are $1 - 20 \frac{\mu l}{\min}$, but flow rates up to $200 \frac{\mu l}{\min}$ could also be dispersed [10].

An example of an off-line electrospray source, capable of handling extremely small amounts of analyte solution, is the so-called "nanoelectrospray ion source" [12]. No liquid feed system is used in this case. Only the intrinsic volume of the ESI-needle itself is used as an analyte supplying reservoir during electrospray operation. Hence, the essential part of this ion source is the ESI-needle, a gold-coated, pulled glass capillary, which ends in a short taper of very fine inner diameter (ID: $\sim 1 - 2~\mu$m), and is directly filled with only a few μl of analyte solution. In absence of an external feeding system, the flow rates are dictated by the ES process itself, and lie in the range of $20 - 40 \frac{nl}{\min}$ [12]. Due to the very low analyte consumption, nanoelectrospray is the preferred ES technique if only tiny amounts of precious analyte solution are available.

J. Jeng and J. Shiea recently reported about a different version of off-line electrospray source, based on "ionization from a droplet deposited on a surface-modified glass rod" [13]. Their direct-electrospray probe consists simply of two gold coated

---

[2]On-line denotes here the direct connection of the ion source with a liquid feed system, e.g. an analyte syringe with corresponding pump or a coupling to a liquid chromatography column.

optical fibers, which are fixed inside a platinum coil. In contrast to nanoelectrospray, a single macroscopic droplet of analyte solution is placed on top of two horizontally oriented optical fibers. By increasing the high voltage, the deposited droplet moves along the contact line to the tip of the fibers, where a stable electrospray is observed. A droplet disappearance rate of $\sim 45 \frac{\text{nl}}{\text{min}}$ was estimated by the authors. A major advantage of this direct-electrospray probe is the avoidance of a possible tip clogging, that otherwise can happen in the case of $\sim 1\ \mu$m inner diameter nanoelectrospray tips.

The spray solution emerging from an ESI-needle maintained at high voltage can be dispersed in different ways depending on the relative geometry of the ESI-needle and counterelectrode, supplied analyte flow rate, and applied voltage. Concerning the high voltage, an upper boundary exists in the form of a corona discharge, denoting the electrical breakdown between the ESI-needle and the counter electrode. The lower boundary is the surface tension of the analyte solution itself, which results in a simple dripping of the supplied spray solution when no voltage is applied. A. Jaworek and A. Krupa [14] distinguished ten modes of electrohydrodynamic spraying in their qualitative study of jet structure and droplet formation. Depending on the applied high voltage, different spray modes are defined on the base of observable geometrical forms of the liquid meniscus and/or emitted jet(s). The 'Taylor cone-jet regime' is a stable atomization condition most commonly referred to in literature. The lateral surface of the Taylor cone[3] forms a half-angle of 49 ° with respect to the jet axis.

The charging of the emerging liquid meniscus surface is the result of a discharge process taking place at the inner wall of the ESI-needle, which is basically an electrochemical process [10]. The origin of this discharge process could be regarded to lie in a partial penetration of the electric field through the liquid meniscus at the tip of the ESI-needle [16]. Anions discharged at the ESI-needle[4], lead to the 'generation' of a counterbalanced positive charge at the surface of the liquid meniscus, which corresponds to a displacement between the positive and negative centers of charge of cations and anions.

---

[3]The historically interested reader is directed to the original work of Sir Geoffrey Taylor [15].

[4]During positive ion mode operation, the ESI-needle acts as anode, while the counterelectrode adopts the role of the cathode (see figure 3.1).

The conical shape of the emerging liquid cusp is a consequence of the force balance between the surface tension at the liquid meniscus and the repulsive forces of accumulated surface charges [17]. For the onset of ESI a certain electric field strength is required, which depends mainly on the surface tension of the supplied liquid, but also on geometrical factors like the radius of the ESI-needle used [16].

Also, the surface of the emerging liquid jet that is drawn out from the apex of the liquid cone carries additional surface charges, leading to the generation of charged primary droplets after subsequent disintegration of the pulled liquid jet. Although the precise mechanism of this disintegration is still unclear [10], the breakup of the jet into charged droplets is clearly driven by energetic reasons. Within the transition from the jet-geometry toward the charged aerosol of primary droplets, the surface-to-volume ratio of the dispersed liquid is increased. At the same time the electrostatic forces between separated primary droplets are decreased, and therefore, the corresponding Coulomb energy is reduced [17]. All this is only due to the action of an electric field on a polar spray solution.

In pneumatically assisted ESI, the dispersion of analyte solution is additionally supported by a concentrically supplied flow of nitrogen gas. The generated primary droplets are typically $\sim 2~\mu$m in diameter [7]. They shrink continuously due to the evaporation of neutral solvent molecules [10, 11], which is often enhanced by e.g. the presence of a hot countergas [9]. Their surface charge density increases with the course of solvent evaporation, as the excess charges still remain at the surface of these primary droplets. Therefore, the energetic status of the primary droplets becomes increasingly unfavorable as the evaporation of the neutral solvent continues until the Rayleigh limit is reached, and the primary droplets continue to fission into several secondary offspring droplets.

This phenomenon, which is crucial to the functioning of ESI, has recently been investigated by D. Duft et al. [11] for the case of levitated microdroplets. The authors recorded the dynamics of the disintegration process under high-speed optical microscopy. Charged droplets were created by means of a piezo-driven nozzle and were subsequently suspended in an electrodynamic levitator. Figure 3.2 shows the typical temporal evolution of such droplets.
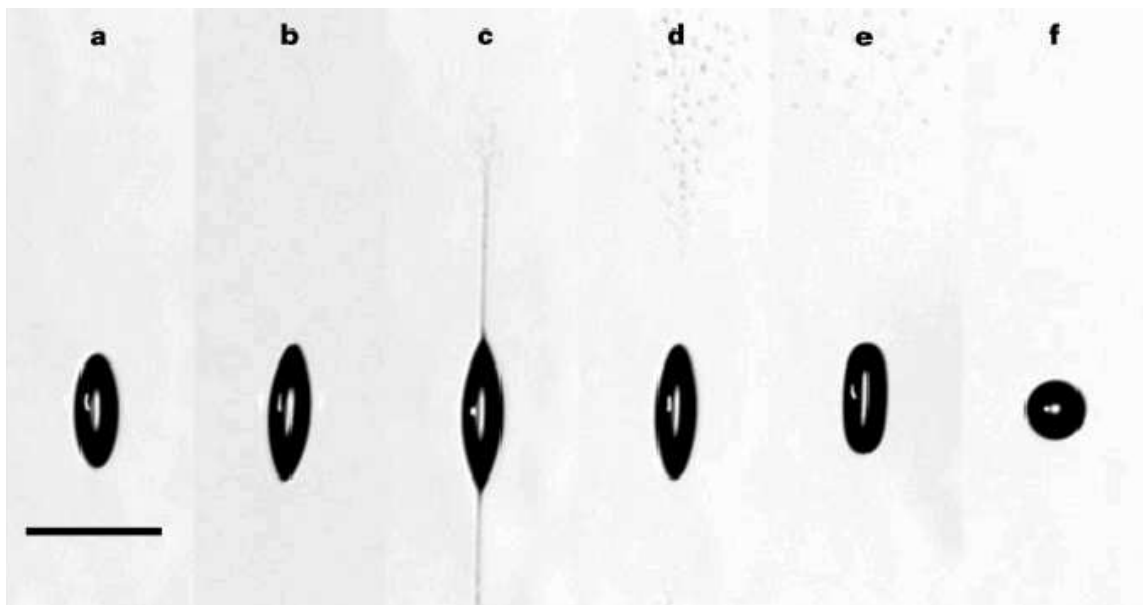
Figure 3.2: High speed imaging of the disintegration of a levitated droplet close to the Rayleigh limit. Images were taken at the following Δt values (in μs): **a** 140, **b** 150, **c** 155, **d** 160, **e** 180, **f** 210, scale bar = 100 μm. Image reproduced from [11].

Immediately after injection, the spherical primary droplet has a radius of 58 μm. Due to evaporation of neutral solvent molecules, the droplet approaches the Rayleigh limit of stability that corresponds to a radius of about 24 μm. At this point, due to a drastic increase in the quadrupole-shape oscillations, the droplet stretches from a sphere into an ellipsoid (see image **a** of figure 3.2), and starts to develop two sharp tips at the poles immediately afterwards (image **b**). Nearly instantaneously after the formation of these tips, the ejection of a fine jet can be observed at both poles (image **c**). These jets disintegrate into fine droplets, which repel each other due to Coulomb repulsion (image **d**). After the jet ejection is finished, the tips at the poles disappear (image **e**), and finally a spherical symmetry is regained (image **f**). In total, about 100 smaller offspring droplets are created during the jet disintegration examined here. In total, these offspring droplets constitute only about 0.3% of the primary droplet's mass but carry 33% of its total charge [11].

The iteration of this process, caused by a further evaporation of neutral molecules, forces the primary droplet as well as all offspring droplets to enter new jet-ejection and jet-disintegration cycles, creating new generations of even smaller droplets.

The examination of levitated charged droplets obviously represents an idealized case, compared to general ESI conditions. The generated primary droplets are typically smaller in size, and their shape (as well as that of all offspring droplets) undergoes a prolate or oblate distortion due to the movement toward the counterelectrode [17]. Anyhow, the above described uneven fission of mass and charge between primary and offspring droplets, finally leading to the vaporization of analyte ions into the free gas phase (see next section), still takes place.

3.3   Analyte Ion Formation: Ion Evaporation and Charge Residue

The concomitant loss of a large fraction of charge and only little mass during a Rayleigh fission event forbids that the main remaining part of a primary droplet repeats a large number of offspring release cycles, which finally leads to the formation of lowly charged residues. For the same reason, offspring droplets themselves are close to further Rayleigh fission events [11]. Since they contain only few analyte molecules right from the beginning, new generations of offsprings might contain even fewer analyte molecules, approaching the limit of a single molecule.

Two scenarios for the final formation of analyte ions can be found in literature, which proceeds according to the charge residue model and the ion evaporation model, respectively. Both assume that free gas phase ions are only formed from very small droplets [18]. Within the **c**harge **r**esidue **m**odel (**CRM**), these very small droplets are produced due to a repetition of Rayleigh fission and solvent evaporation cycles up to a point where the droplets contain only one ion [18]. Contrarily to the CRM, the **i**on **e**vaporation **m**odel (**IEM**) explains the formation of free gas phase ions as the consequence of a direct evaporation of charged analyte molecules from very small charged droplets. This evaporation of analyte ions is caused by the high electric field close to the droplet surface. This field has to be strong enough to overcome the interactions of analyte ions and solvent molecules [18]. Either way, even within the IEM scheme, it is not correct to consider that analyte ions are transferred into the gas phase as completely 'dry' ions. Instead it is more reasonable to consider a charged
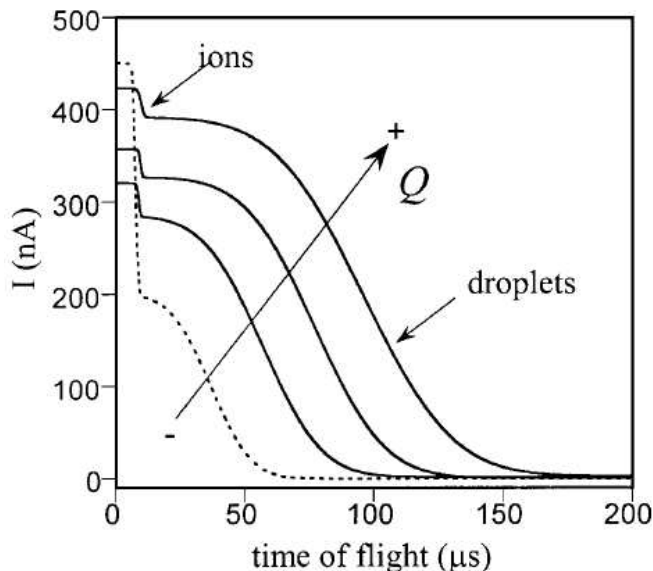
Figure 3.3: Time-of-flight spectra showing well defined ions and charged droplets after controlled interruption of the ESI-process at t = 0 μs. The arrow in Q direction denotes the rise in the corresponding flow rates. Image reproduced from [19].

analyte+solvent cluster that gradually evolves into a solitary gas phase molecule to which a number of charges are attached [10]. It should be noted that within both models the formation of charged residue clusters is allowed via the final evaporation of solvent molecules, which are still contained in the 'mother droplet' of the residue.

A clear-cut experimental distinction between IEM and CRM is extremely difficult, mainly because of the intrinsic limitation in tracking very small droplets with a diameter of several nanometers while both their charge and mass are evaporating.

An ingenious approach to the topic of ion evaporation was made by Manuel Gamero-Castaño, who was able to present a direct proof of ion field evaporation from dielectric liquids [19]. Instead of following the evaporation of ions from higher order offspring droplets, he investigated the mechanism of ion evaporation from the strong electrical field cone-to-jet transition region of a Taylor cone in the low flow regime[5]. Figure 3.3 shows time-of-flight spectra of the electrospray current I(t), recorded after the ESI-process was selectively interrupted at t = 0 μs. The time dependence of each I(t) curve shows two steps, a well defined faster step followed by

[5]Numerical computations about the "Ion evaporation from the surface of a Taylor cone" can be found in [20].
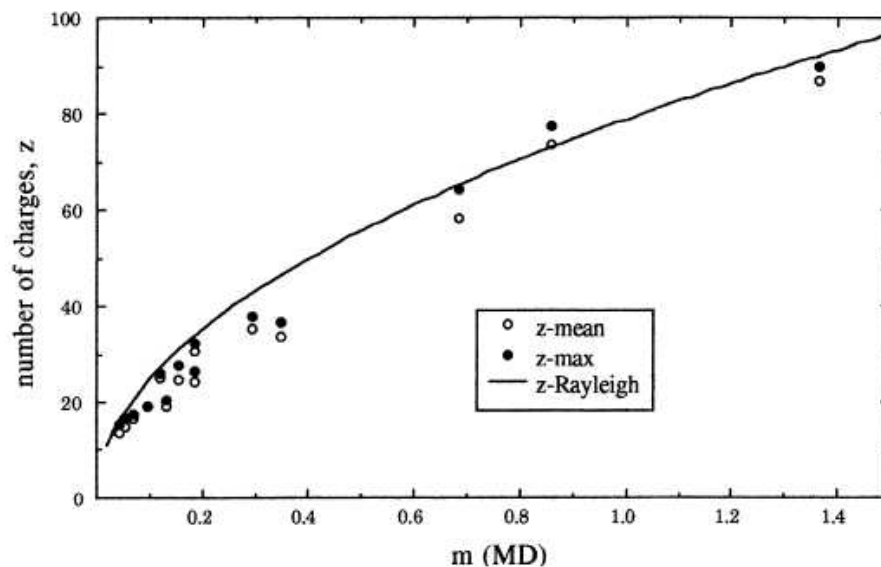
Figure 3.4: Charge state z of various proteins versus mass (in 10^6 Da) compared to the Rayleigh limit of charged water droplets of equal size. Image reproduced from [21].

a broader second step. The fastest step is associated with well defined ions, whose time-of-flight is independent of the addressed flow rate Q. The slower second step is due to charged droplets, which are known to have a decreasing mass-to-charge ration for diminishing Q.

In the case of very large molecules, a solid consensus has emerged that analyte ions are formed by ESI according to a charge residue mechanism [17]. If the CRM holds, nearly the same amount of charges can be expected on a 'droplet probe molecule' (spherical molecules such as globular proteins or dendrimers) and on a small water droplet at the Rayleigh limit [16]. Within this picture the smallest possible diameter of the charged water droplet is represented by the size of the probe molecule, while the upper limit of the charge on the probe molecule is given by the charge state of the water droplet at the Rayleigh limit.

Fernandez de la Mora [21] reported that the average number of charges on polypro-tonated native globular proteins, obtained from aqueous solutions at neutral pH, are close to the number of charges carried by aqueous droplets of equal size at the Rayleigh stability limit [16]. Figure 3.4 collects experimental data of maximum and mean charges for various proteins compared with the Rayleigh limit of a charged water droplet. The comparison between the depicted Rayleigh curve of the charge

state z of a water droplet at the Rayleigh limit and the charge states of the proteins yields good evidence that the CRM holds for globular proteins.

During this presentation of IEM and CRM we intrinsically assumed that only two classes of substances - analyte and solvent - are present in the spray solution. In reality all ions present in the spray solution, also solvent impurities and ions produced during electrolysis at the ESI-needle, compete with each other in the processes that lead to the formation of free gas phase ions [18].

In the above chapter we have briefly introduced the key elements of Electrospray Ionization, namely electrohydrodynamic dispersion, ion evaporation and charge residue. For a more elaborate discussion of the complex ESI processes, in particular with respect to the chemical interactions, we refer the reader to the literature. The dependence of the sensitivity in ESI-MS on the chemical nature of the analytes and on the analyte concentration can be found in the publication of P. Kebarle [16]. R. B. Cole [17] provides further information about gas phase processes influencing the charge state distribution and signal intensity in ESI-MS. The book edited by R. B. Cole [9] compiles various aspects of instrumentation and application, together with fundamentals of ESI-MS. Further considerations toward the field of ESI-MS are supplied in references [18, 21, 22, 23, 24, 25, 26, 27] and [16, 17, 28, 29, 30] within the frame of special issues of Analytica Chimica Acta and the Journal of Mass Spectrometry, respectively.

Concluding, I would like to quote J. B. Fenn and S. C. Rutan [22]: "... the mechanism by which the ions are formed remains an enigma that is the subject of much discussion, disagreement and debate ..."

Chapter 4

Design and Characterization of the Electrospray Deposition Source

4.1 Conceptual Overview on the ESI Source

The intention of this section is to provide a conceptual overview on our novel deposition source that utilizes the electrospray technique for the soft ionization of sensitive analytes. Figure 4.1 shows a schematic drawing of the ESI deposition source, of which the task is the formation of a beam of analyte ions, originally dissolved in solution, and its deposition on chemically clean substrates. After the ions are released into the gas phase during the course of ESI (see section 3.1), they leave the ESI-head through a glass capillary, entering the beam formation stage. There, after a supersonic expansion into vacuum, the angular and energetic definition of the ion beam is performed by the combined action of electrostatic (apertures, lenses) and electrodynamic (quadrupole ion guides) ion optical means. Next, the analyte beam is passed through the o–TOF chamber, where the composition of the ion beam is analyzed. Then the ions pass through a further chamber, which is needed in order to link the vacuum stage of the TOF chamber with the UHV stage of the deposition chamber, and finally they are gently deposited on chemically clean and atomically defined substrates.

Figure 4.2 depicts the ESI deposition source in more detail. On the left side, the
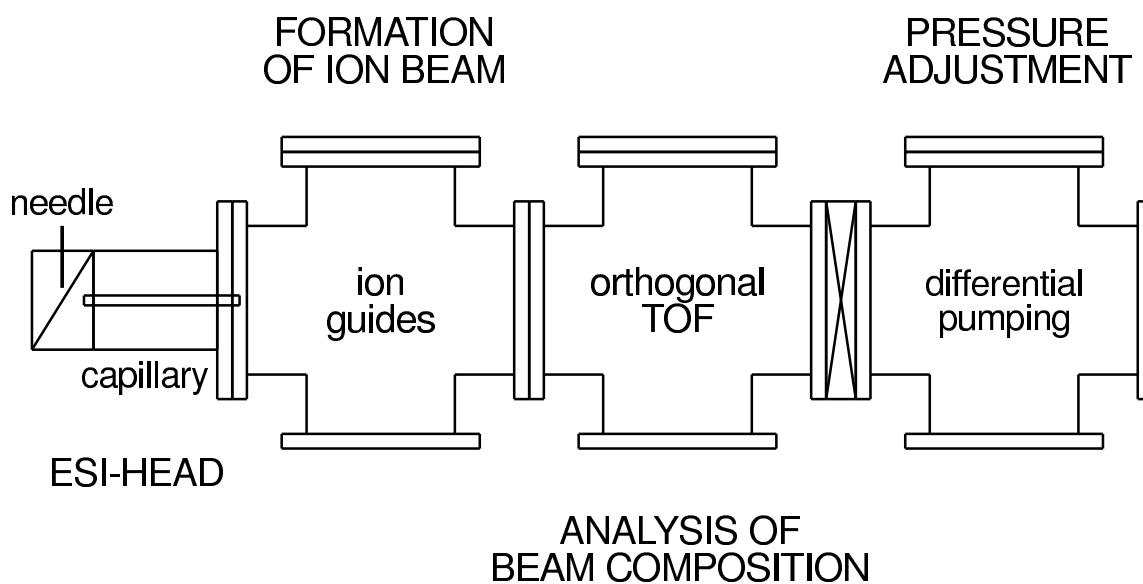
FORMATION
OF ION BEAM

PRESSURE
ADJUSTMENT

needle

ion
guides

orthogonal
TOF

differential
pumping

capillary

ESI-HEAD

ANALYSIS OF
BEAM COMPOSITION

Figure 4.1: Schematic side view of the ESI deposition source for the soft-landing of sensitive analyte ions under UHV conditions.
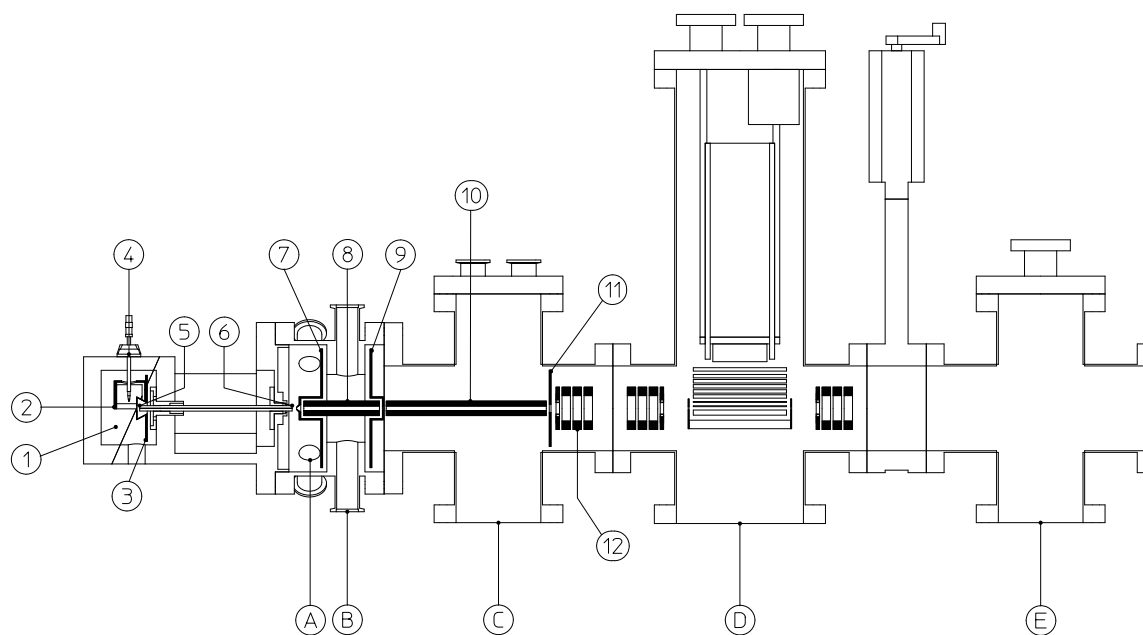
Figure 4.2: Detailed scheme of the ESI deposition source. (1) nebulizer chamber, (2) chamber electrode, (3) entrance plate, (4) nebulizer, (5) entrance side of glass capillary, (6) exit side of glass capillary, (7) skimmer, (8) 1st ion guide, (9) 1st aperture plate, (10) 2nd ion guide, (11) 2nd aperture plate, (12) 1st ion optical system, (A)–(E) denote differentially pumped vacuum stages with increasing quality of vacuum (see text).

pneumatically assisted ESI-head[1] is shown. A needle on top of the ESI-head serves as nebulizer (4) and is fed by a continuous flow of analyte solution, supplied by a syringe pump that is connected via teflon tubing. This electrospray assembly provides free gas phase ions at atmospheric pressure conditions. Several high voltage electrodes in this atmospheric region 'force' the electrohydrodynamic dispersion of the spray solution (see section 3.3). Additionally, the presence of a counterflow of dry heating gas assists the release of the analyte ions (see section 4.2.2).

The atmospheric side of the ESI-head is connected to the first vacuum stage by means of a glass capillary (5)+(6) that creates a pressure gradient and transports the mixture of gas and analyte ions. The transported flux depends on the length and the cross-section of the capillary as well as on the pressure difference at the capillary ends. With values of ~ 1.0 mbar for the pressure in the first vacuum stage, typical transported currents of ~ 1 nA can be obtained.

The remaining reduction by 10 orders of magnitude in pressure, from the first vacuum stage up to the UHV deposition chamber (pressure $\sim 10^{-10}$ mbar), is gradually reduced by means of several differential pumping stages. Each stage consists of two neighboring vacuum chambers connected by a small orifice. The gas flow between the two chambers is determined by the product of the conductance C of the orifice and the pressure difference $\Delta p = p_{\circ} - p_1$ in between them. Through the right dimensioning of the orifice diameter and the pumping speed in the two chambers, vacuum gradients $\frac{p_1}{p_{\circ}}$ down to 10^{-3} can be reached. For example, a pressure of ~ 0.1 mbar in vacuum stage (B), a connecting orifice of 2 mm inner diameter, together with a pumping speed of $350 \frac{l}{s}$ in vacuum stage (C), are sufficient for attaining a pressure of $\sim 1 \cdot 10^{-4}$ mbar in vacuum stage (C).

Passing the ion beam through apertures of $\sim 1 - 2$ mm inner diameter is of primary importance. Although it is possible to drag, steer, guide, and focus ions with the help of electrostatic and electrodynamic elements, these operations are always accompanied by intensity losses. In order to maintain the beam intensity as high as possible, and hence the sample preparation times as short as possible, an ion beam

---

[1]The design of the ESI-head is based on a Series 1100 Electrospray Assembly of Agilent Technologies.

that is well defined in real space and energy is needed. In practice, the analyte ions emerging from the capillary possess a broad distribution of kinetic energy, mainly resulting from the repulsive Coulomb interactions during expansion. Consequently, an extra beam formation stage is needed in order to produce a well defined ion beam. This is done by means of a skimmer (7), performing a first angular definition, together with two quadrupole ion guides (8)+(10) (see section 4.3). In the region of the 1st ion guide (8) a narrow thermal energy distribution as well as an axial concentration of the analyte ions are achieved due to collisions between the ions and the background gas (typical pressure: $0.1 - 0.3$ mbar). The 2nd ion guide (10) in contrast, performs a mass-to-charge selection of the transported analyte ions since the lower vacuum drastically reduces the frequency of collisions.

The beam formation stage follows downstream of the ESI-head and consists of three different pumping stages: A first vacuum stage (stage (A) of figure 4.2) where the free supersonic expansion and a crude angular definition of the ion beam take place, and two further vacuum stages (stages (B)+(C) of figure 4.2) which are located in the 1st and 2nd ion guide, respectively.

At present the ESI deposition source is running well and has been completely characterized up to this point. In addition, the emerging ion beam has already been used for first deposition experiments on conductive substrates (see chapter 5).

Vacuum stage (D) of figure 4.2 is already in place (pressure $\sim 1 \cdot 10^{-6}$ mbar), but the assembly of the linear o–TOF to be installed there (expected resolution $\frac{m}{\Delta m} \simeq 500$) is not finished yet. The o–TOF will allow us to analyze the composition of the ion beam online, and therefore we will also use it to monitor the tuning of the composition of the ion beam. After the examination of the transport behavior through the o–TOF chamber is finished, we will continue to assemble the still missing pressure adjustment chamber (stage (E) of figure 4.2). The function of this chamber is to link the o–TOF chamber with the deposition chamber while further reducing the pressure to the UHV limit. This will be achieved again by means of differential pumping. The analyte ions that eventually enter the final chamber will be directed toward the substrate and decelerated by ion optics in order to be gently deposited onto the substrate.

Figure 4.3 shows a photograph of the present ESI deposition source. The pneumatically assisted ESI-head together with an analyte syringe, the syringe pump, the beam formation stage, and the o–TOF chamber can be recognized.
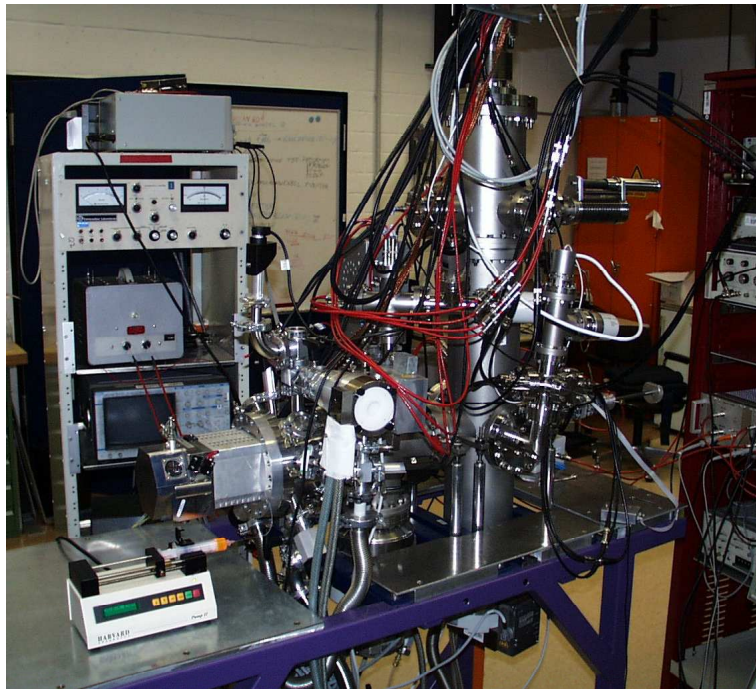

Figure 4.3: Photograph of the ESI deposition apparatus. The pneumatically assisted ESI-head with analyte syringe and syringe pump, the beam formation stage, and the o–TOF chamber can be easily recognized. Compare with schematic representation in figure 4.2.

In the remaining part of this chapter, we follow the gas phase analyte ions step by step on their flight through the ESI deposition apparatus. Each part of the apparatus will be discussed in detail during this downstream journey. In order to describe these parts and to elucidate the influence of the various parameters, such as analyte supply rate and atomization parameters, and pressures and voltages, we used the intensity of the ion beam, measured as current, at various points of the apparatus. These measurements were done by means of a self written LabVIEW[TM]-based acquisition software, reading the output signal of a Keithley 616 Digital Electrometer operated mainly in the charge detection mode. When interested in the effect of one parameter on the overall performance of the system, we collected the analyte current as far downstream as possible, which is the position of sample preparation (see figure 5.1) utilized during the deposition experiments presented in chapter 5. Although only

mass spectra measured with the o–TOF could furnish definitive information on the ion beam nature and its quality, ion currents measured at the sample position allow a very good approximation to the optimum operation conditions. In fact, only those ions that fulfill the mass-to-charge pass condition are transported by the two quadrupole ion guides and subsequently deposited onto the substrate. As a consequence, the characterization presented in this chapter can be considered to be based on true analyte ion beam intensities which are close to the optimum TOF-based intensities.

The design of the ESI-head, and the corresponding explanation of the underlying working principle are provided in section 4.2. This is followed by a discussion about two different modes of operation of the ESI-head, the role of the hot countergas introduced during the course of ESI, its temperature and the correct choice of the flow rate, as well as the function of the fragmentor voltage. Next, the working principle of the beam formation stage, including a short description of the mechanical design of the ion guide tandem and its electronics is presented in section 4.3. Afterwards, correlations between the dc voltages applied to the ion guides and the measured analyte current are discussed. Finally, the influence of the background pressure in vacuum stage (B) (see figure 4.2) on the kinetic energy distribution of the analyte ions is examined.

4.2   Characterization of the ESI-Head

Figure 4.4 shows an enlarged view of the Series 1100 ESI-head of Agilent Technologies that has been adapted to our system. The corresponding geometrical dimensions and the potentials applied to the various components denoted in the figure are summarized in table 4.1.

Inside the nebulizer chamber (1), the chamber electrode (2) and the conically shaped entrance plate (3) are in close proximity to the tip of the nebulizer (4)[2]. The whole ESI-head and the nebulizer (4) are per construction at ground potential, while equal high voltages are applied to the electrodes (2) and (3). This generates an inhomogeneous electric field between the nebulizer's tip-end (4) and the conical

---

[2]A detailed description of the working principle of the nebulizer can be found in section 4.2.1.
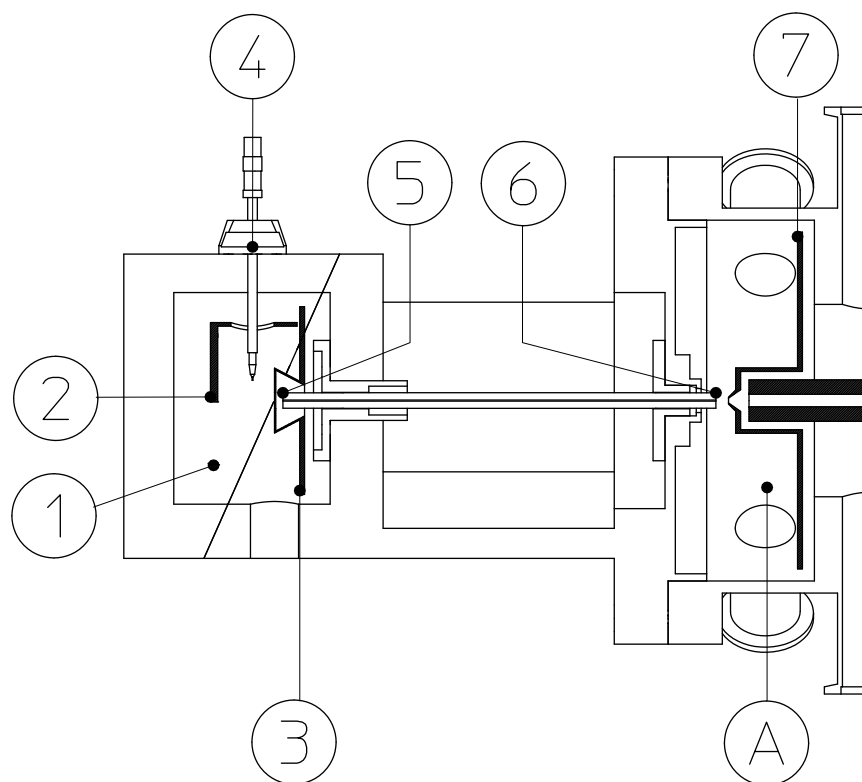
Figure 4.4: Adapted design of the commercial ESI-head: (1) nebulizer chamber, (2) chamber electrode, (3) entrance plate, (4) nebulizer, (5) entrance side of glass capillary, (6) exit side of glass capillary, (7) skimmer, (A) 1st vacuum stage.

name of component	geometrical dimension	applied potential
components inside nebulizer chamber: $p \simeq 1$ bar		
inner metal capillary of nebulizer (4)	ID: 125 μm OD: 250 μm	grounded
entrance plate (3)		-3.0 kV $\leq V_{\text{ent.}} \leq -4.0$ kV
distance between (3) and (4): 6 mm		
entrance of glass capillary, capillary (5)	ID: 0.6 mm OD: 6.5 mm	-3.5 kV $\leq V_{\text{cap.}} \leq -4.5$ kV
components inside vacuum stage (A): $p \sim 1$ mbar		
exit of glass capillary, fragmentor (6)	length: 180 mm	$+100$ V $\leq V_{\text{frag.}} \leq +150$ V
skimmer (7)	ID of orifice: 2 mm	$+0$ V $\leq V_{\text{skim.}} \leq +50$ V
distance between (6) and (7):	5 mm	

Table 4.1: Geometrical dimensions and typical voltage ranges used for several components of the ESI-head. Letters and numbers in parentheses refer to figure 4.4.

face of the entrance plate (3), that leads to the electrohydrodynamic dispersion of the analyte solution inside the nebulizer chamber (see section 3.2). The same electric field drags all charged droplets in the direction of the entrance plate (3), acting as the counter electrode (see figure 3.1). A counterflow of dry heating gas (hot countergas) is directed into the nebulizer chamber from behind the entrance plate (3). This leads to a warming up of the whole ESI-head that augments the evaporation of the solvent during droplet shrinkage, and therefore improves the ESI-process of the analyte. In order to prevent the build-up of an overpressure inside the nebulizer chamber, the excess gas is released into the ambient air by means of an exhaust aperture. On the other side, it acts as a repelling gas curtain (see section 4.2.2) that prevents dust particles, charged primary droplets, and residues from entering the ESI deposition apparatus. When the source is tuned correctly, only highly mobile analyte ions together with small neutral molecules that are affected only by the pressure drop, are able to enter the sampling orifice of the glass capillary (5), and to be transported through the capillary up to its exit (6).

The subsequent expansion of the transported particles into the vacuum stage (A) of figure 4.4 results in the generation of a supersonic jet of neutral and charged components. The charged components experience further repulsive interactions during expansion, leading to a broader kinetic energy distribution compared to a pure aerodynamic acceleration of a completely neutral beam.

A first angular definition of the ion beam is then performed by the skimmer (7), which separates the shell of the expanding supersonic jet from its central part, and passes the remaining core portion of the ion beam toward the 1st ion guide, which is already inside the 2nd vacuum stage (see figure 4.14).

4.2.1 Nebulizer versus Emitter Operation

The electrospray solution is fed at constant flow rate to the nebulizer (4) with the help of a programmable syringe pump. The nebulizer is composed of two main parts, a thin metal capillary, which is coaxially enclosed by the surrounding body of the nebulizer. Depending on the protrusion of the inner metal capillary over the brim of the body we are able to distinguish two modes of operation: The emitter-mode, where a pure electrohydrodynamic analyte atomization takes place, and the nebulizer-mode in which the dispersion is pneumatically assisted. The nebulizer-mode operation is obtained when the inner metal capillary protrudes only few tenths of a millimeter (~ 0.2 mm). For this geometry we profit as much as possible from the nitrogen gas being concentrically supplied by the outer body and assisting the formation of the primary droplets. In contrast, in emitter-mode no nitrogen gas assists the electrohydrodynamic analyte atomization, and the protrusion of the inner metal capillary is increased to $2-3$ mm. This results in a reduced electrical shielding of the inner metal capillary by the nebulizer body, and an even more pronounced electrohydrodynamic tip-effect due to a reduced distance to the high voltage counter electrode.

The difference between the two operating modes is mainly reflected in the on-off behavior of the ESI-process as function of the applied **h**igh **v**oltage (**HV**). In order to experimentally verify this, we measured the current that arrives at the skimmer as a function of the HV potential applied in parallel to the entrance plate and the
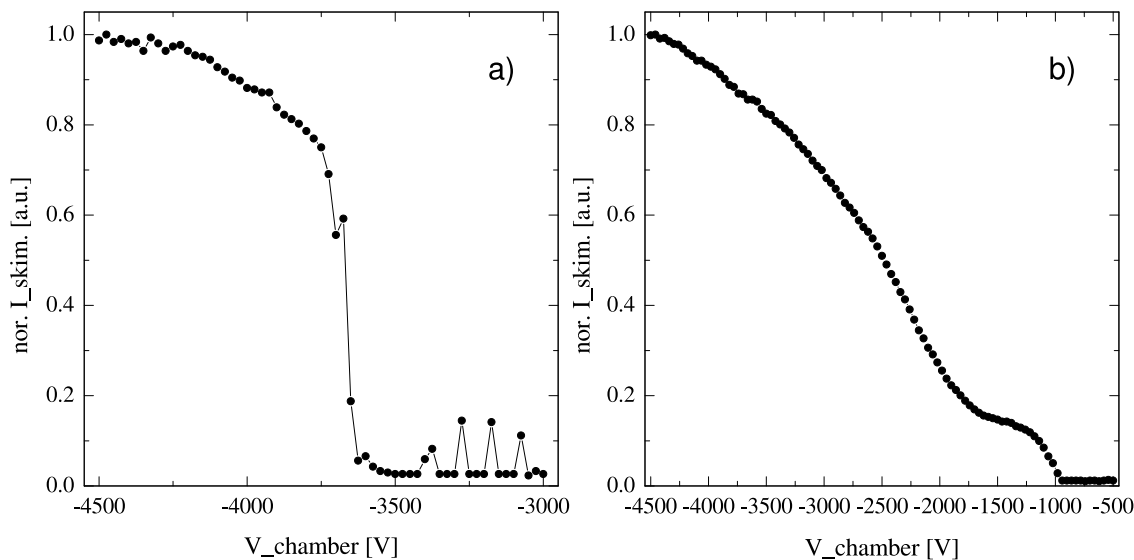
Figure 4.5: Examples of normalized I-V curves taken under emitter-mode (a) and nebulizer-mode operation (b). The corresponding analyte solutions contained ferritin (a) and albumin (b), respectively.

metal coated entrance of the glass capillary.

Figure 4.5 depicts I-V curves for different operation modes. Although different analyte solutions were used in this comparison (bovine serum albumin, compare section 5.5; and horse spleen ferritin, section 5.6), the features observed do not strongly depend on the spray solution used, and therefore can be considered as typical of the two operation modes. The I-V curve obtained for emitter operation (figure 4.5a) is very close to an ideal step-like on-off curve. In fact, only when the electric field forces are able to overcome the surface tension of the spray solution (see section 3.2), corresponding to the existence of a certain onset high voltage, is the ESI-process initiated and analyte ions released. In this example, this evidently happens for a HV value of ~ -3.6 kV.

In contrast, during nebulizer operation (figure 4.5b) it is still possible to detect an electrospray current even 'at less than' -3.0 kV. The whole I-V curve shows an almost linear behavior, without any significant step-like feature. Here, the supplied nebulizer gas, together with the electrohydrodynamic dispersion, is able to support the ESI-process up to much 'lower' voltages. This is due to the additionally imposed pneumatic stress that adds to the electrostatic dispersion forces, extending the limit
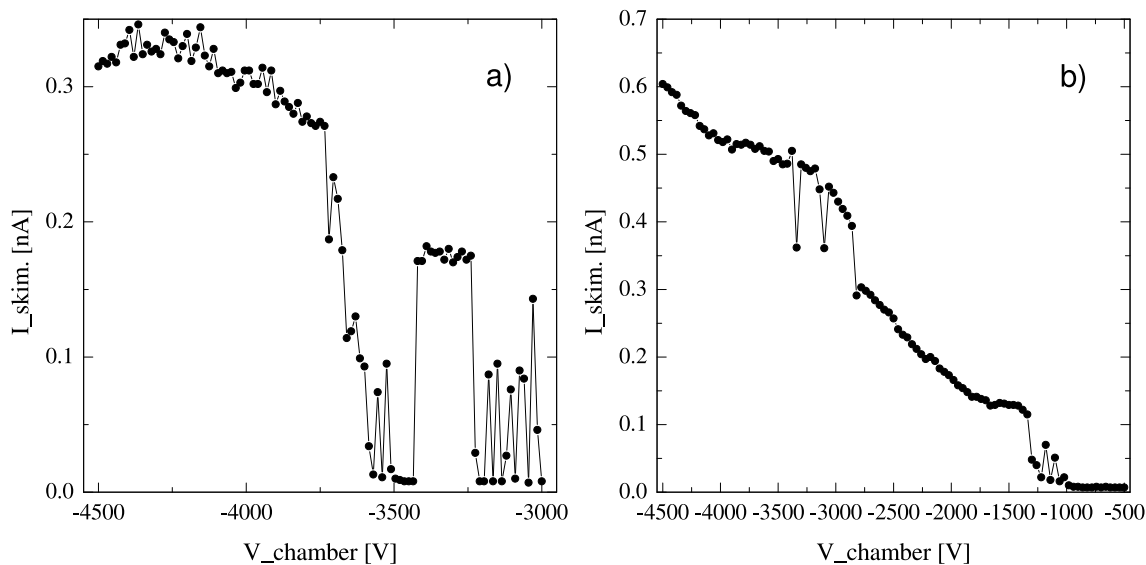
Figure 4.6: Examples of typical instabilities encountered during atomization in emitter-mode (a) and nebulizer-mode (b) operation. The corresponding analyte solutions contained either ferritin (a) or albumin (b).

of ion vaporization to -1.0 kV.

Figure 4.5 depicts I-V curves close to the optimum case for both operation modes. In reality, it is very difficult to address a very stable spraying behavior, both for the emitter as well as the nebulizer operation. The temporal stability of the spray current is in fact very sensitive with respect to the balance of the two main parameters, the supplied analyte flow and the applied HV. Figure 4.6 shows I-V curves closer to the every day experimental reality. The emitter-mode (figure 4.6a) is still characterized by a step-like transition, but in addition a self-initiation of the ESI-process 'at less than' -3.5 kV can be observed. In the case of the pneumatically assisted nebulization, the instabilities are still present, even though they are less pronounced due to the 'smoothing action' of the concentrically supplied gas stream supporting the nebulization.

Pulsation phenomena during ESI have been reported in literature [31]. There it resulted from an imbalance between the supply of spray solution to the liquid meniscus at the tip of the ESI-needle and the loss of the spray solution from the meniscus during a sequence of emission pulses. A similar explanation possibly also holds for the instabilities observed in figure 4.6.

In the course of the experiments it could not be decided whether the emitter- or the nebulizer-mode is the most suitable mode of operation for the dispersion of analyte solution. For identical spray solutions, it is possible to achieve the same deposition current at the sample position (see figure 5.1), regardless of the utilized mode. From the point of view of ionization efficiency, small highly charged droplets directly after the cone-jet disintegration are more preferable. Therefore the emitter-mode, whose technological conception is closer to the nanoelectrospray technique (see section 3.2), might be regarded as the preferable mode of operation. However, only a direct comparison of the two operation modes by mass spectrometric means will allow a final judgement.

4.2.2   The Role of the Hot Countergas Flow

Any design of an ESI-head has to take into account the formation of cluster ions, resulting from the condensation of polar neutrals on analyte ions during in-vacuum expansion [9]. Polar molecules like water or other solvents tend to cluster with analyte ions as a consequence of the strong cooling that accompanies the expansion into vacuum. The problem of clustering can be reduced by blocking the solvent molecules before entering the first vacuum stage. This is schematically shown in figure 4.7 that represents the effect of the so-called dielectric interface of our commercial ESI-head. An effective separation of polar neutrals and analyte ions is achieved by a continuous flow of hot nitrogen gas, being supplied from the rear of the conically shaped entrance plate. Dust particles, neutral contaminants, and water vapor are pushed away from the opening of the entrance plate, whereas the analyte ions are dragged toward the entrance of the capillary by means of the electrical fields between the ESI-needle, the entrance plate, and the metal coated sampling orifice of the glass capillary.

After having served as a gas curtain, most of the nitrogen flows into the nebulizer chamber, while only a small part is pumped through the orifice of the capillary. Due to its high temperature (typically 150 °C), the effect of the countergas is to heat the whole nebulizer chamber and therefore to improve the ESI-process by means of a faster evaporation of the solvent and an enhancement of the droplet shrinkage (see sections 3.2 and 4.2.3). Moreover, it also increases the temperature of the particle
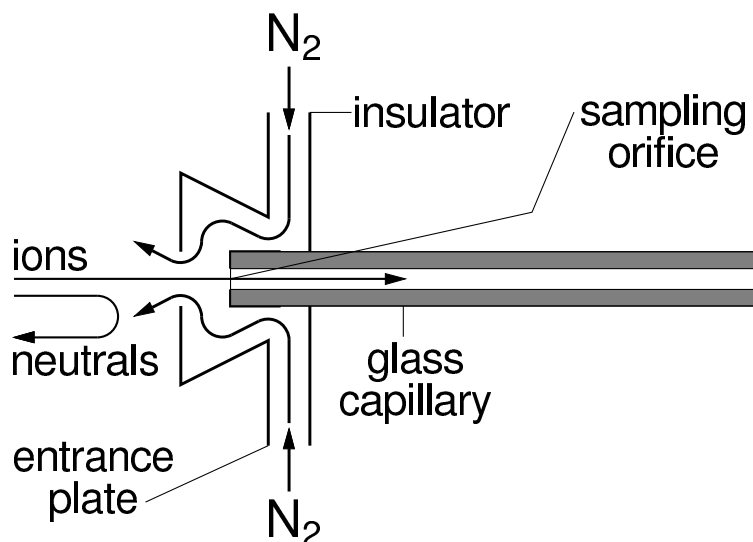
Figure 4.7: Scheme of the Series 1100 dielectric interface of Agilent Technologies located at the atmospheric entrance side of the glass capillary. A hot flow of dry nitrogen gas, in combination with an electric field, is used to create a filter that passes the ions towards the metal coated sampling orifice of the capillary, while neutrals are blocked and cannot enter the ESI deposition apparatus.

flow that enters the glass capillary and subsequently expands into vacuum. As a consequence, even if a small fraction of polar solvent molecules is not filtered by the dielectric interface, the temperature drop due to the supersonic expansion is not enough to cause a formation of cluster ions [9].

The region in front of the entrance plate also acts as a dielectric interface, but it is between the entrance plate and the capillary where the countergas flow is at its maximum and the major part of the filtering takes place. Therefore, once the countergas flow is set, the potential difference between these two electrodes ($\Delta V = V_{cap.} - V_{ent.}$) allows to preferentially select multiply charged analyte ions, instead of polar neutral and charged residues. The latter are the byproducts of the ESI-process and consist of lowly charged solvent-solvent and solvent-analyte clusters of different sizes, typically characterized by a high mass-to-charge ratio (remaining charged droplets can be considered as an extreme case of charged residues). Being charged, they also feel the attractive force of a negative ΔV, but due to their high mass-to-charge ratio (low mobility), they can be efficiently blocked by the right balance between the electric

field and the countergas flow. Although only mass spectrometry can detect the subtle changes in the ion beam composition caused by different choices of $V_{cap.} - V_{ent.}$ as well as of the flow and the temperature of the countergas, it is possible to do a first characterization of the dielectric interface by measuring the ion current at the skimmer (see figure 4.4) as a function of ΔV for fixed values of $V_{ent.}$ and the countergas. Figure 4.8 shows that for $V_{cap.}$ values much higher than $V_{ent.}$ no current can be measured. Under these conditions, the countergas and the positive potential difference
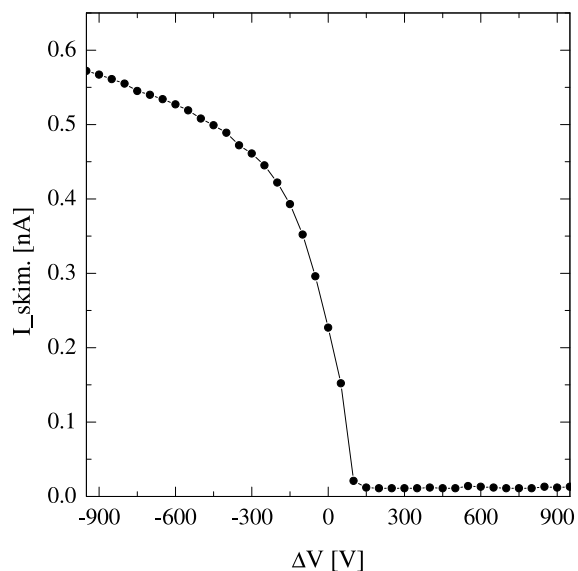

Figure 4.8: The dielectric interface in operation: The I-V curve depicts the skimmer current $I_{skim.}$ as a function of $\Delta V = V_{cap.} - V_{ent.}$. In this experiment $V_{ent.}$ was fixed at -3.6 kV and $V_{cap.}$ was varied. The spray solution contained bovine albumin as analyte, which is atomized under emitter-mode operation ($12 \frac{\mu l}{min}$ at 0 bar). The flow and the temperature of the countergas are fixed at $12 \frac{l}{min}$ and $150\,°C$, respectively.

ΔV are preventing the ions from entering the ESI deposition apparatus. In contrast, a reduction of $V_{cap.}$ to values lower than $V_{ent.}$ ($\Delta V < 0$) leads to increasing values of $I_{skim.}$, since now the ion attracting behavior of the potential difference ΔV compensates the opposing action of the countergas. The fact that a non-zero current is observed at the skimmer for small but still positive values of ΔV (0 V $\leq \Delta V \leq 150$ V) can be ascribed to the pumping action of the glass capillary itself, which is able to compensate the ion repelling action of the positive potential difference and drives the high mobility ions in the downstream direction.

Summarizing, the selection of ΔV between -500 V and -300 V represents a good compromise between an ideal separation of analyte ions from charged residues and polar neutrals, still providing a sufficient beam intensity.

4.2.3   Analyte Current versus Countergas Temperature

Another important experimental parameter is the temperature of the hot countergas. We have analyzed its overall effect by measuring its influence on the analyte ion current $I_{sam.}$, measured at the sample position (see figure 5.1). Since the system responds only very slowly to temperature variations (high heat capacitance due to large metal pieces in contact with the hot stream of countergas), the current values in figure 4.9 were averaged over 5 min, and each time a new countergas temperature was set, the current measurements were interrupted for 20 min. The dashed and solid
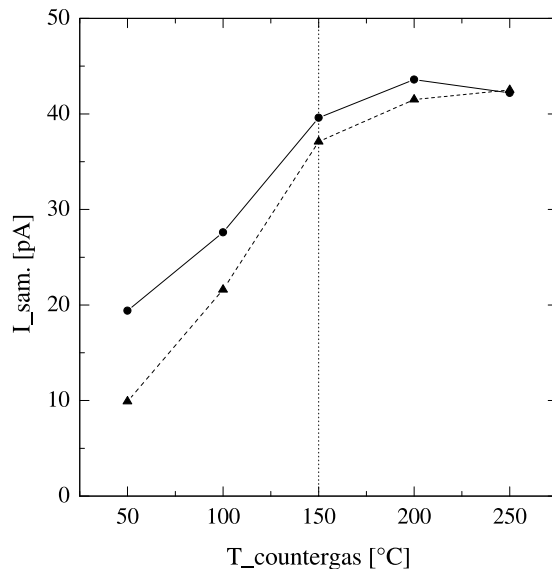

Figure 4.9: Dependence of the analyte ion current $I_{sam.}$, measured at the sample position, on the temperature of the supplied countergas. ▲- and ●-data points were collected for stepwise increasing and decreasing temperature, respectively. The spray solution contained albumin as analyte, which was dispersed under nebulizer-mode operation (10 $\frac{\mu l}{min}$ at 1.0 bar). The countergas flow rate was fixed at 7.5 $\frac{l}{min}$, while its temperature was changed in steps of 50 °C. The vertical dotted line marks the standard countergas temperature used during normal operation.

lines represent current values measured during stepwise increasing and decreasing

countergas temperature, respectively. The difference between the two curves can be attributed to the delayed warming of the whole ESI-head. Both curves show an increase in the mean sample current with increasing temperature and a saturation for temperatures between 200 °C and 250 °C.

With increasing temperature, the amount of heat offered to the shrinkage of primary and offspring droplets leads to an increased efficiency of the analyte ion release during the course of ESI (see section 3.2). On the other hand, for practical operation, lower countergas temperatures are favorable due to the risk of a thermal degradation of sensitive analytes such as proteins. Therefore, a countergas temperature of 150 °C is an optimum compromise for most applications, since the intensity of the ion beam is only 10% less than the maximum saturation value, while the temperature is still moderate.

4.2.4 Adjustment of the Countergas Flow

Besides the countergas temperature, the magnitude of the countergas flow rate is also a parameter that has to be adjusted correctly. Figure 4.10 shows the dependence of the current $I_{sam.}$ collected at the sample position (see figure 5.1) on the supplied countergas flow rate. For high counterflow values between 15 and 30 $\frac{1}{min}$, no analyte ions are able to enter the ESI deposition apparatus, and therefore cannot be measured at the sample position. For counterflow values smaller than ~ 12 $\frac{1}{min}$ a strong rise of $I_{sam.}$ can be observed, reaching its maximum at ~ 6 $\frac{1}{min}$, which is followed by a reduction of $I_{sam.}$ when further decreasing the counterflow. This behavior can be attributed to two effects of the hot countergas acting in opposite directions. On one side, the heat transferred from the gas curtain to the primary droplets enhances their shrinking and the generation of offspring droplets, and therefore the release of analyte ions, increasing the beam intensity. On the other side, an increased countergas flow inherently reduces the amount of ions that are able to pass the dielectric interface (see section 4.2.2).

Consequently, also in this case we have to choose an optimal countergas flow providing enough heat to the ESI-process, while still enabling the separation of lowly charged residues and multiply charged analyte ions, but not excessively reducing the
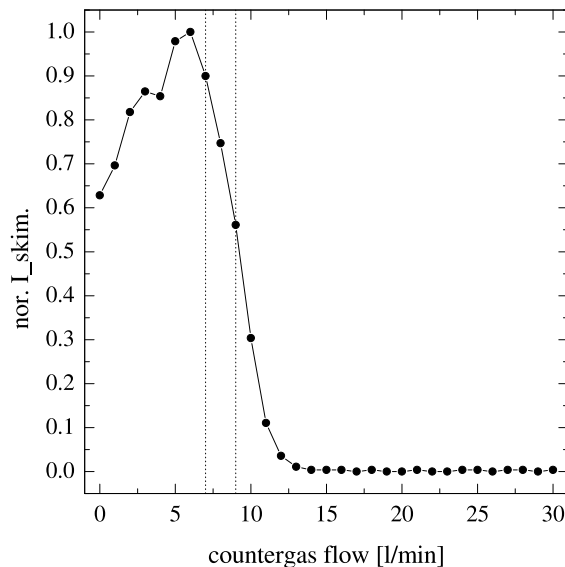
Figure 4.10: Dependence of the normalized analyte current $I_{sam.}$ measured at the sample position (see figure 5.1). The spray solution contained bovine albumin as analyte, which was dispersed under nebulizer-mode operation ($10 \frac{\mu l}{min}$ at 1.0 bar), while the temperature of the countergas was fixed at 150 °C. $V_{ent.}$ and $V_{cap.}$ were fixed at -3.0 kV and -3.4 kV, respectively. The vertical dotted lines delimit the flow values used during normal operation.

final intensity of the ion beam. Referring to figure 4.10, a countergas flow of $7-9 \frac{l}{min}$ represents an optimum compromise between these requirements.

4.2.5 The Role of the Fragmentor Voltage

Figure 4.11 depicts a magnification of the nozzle-skimmer region of the ESI-head. The pressure difference between the ends of the capillary (its entrance is at atmospheric pressure while the other end is located inside vacuum stage (A) at a pressure of ~ 1 mbar, see figure 4.11) transports the ions that have been selected by the dielectric interface, possibly together with a small residual fraction of neutral and polar molecules. While emerging into the first vacuum stage, the gas-ion mixture experiences an in-vacuum expansion by which it is accelerated in the downstream direction [32]. This expansion is accompanied by collisions between the different particles whose strength can be tuned by applying a potential difference between the metal coated end of the capillary and the skimmer (see figure 4.11). If controlled carefully, the collisions can be exploited for the dissociation of possibly remaining
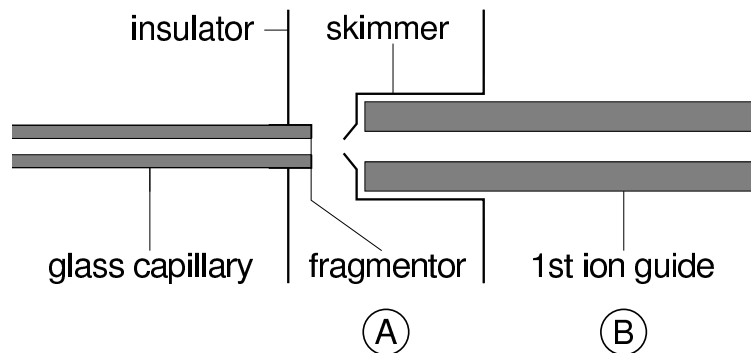
Figure 4.11: Close-up view of the nozzle-skimmer region. The charged component of the supersonic jet is steered in the axial direction due to the electric field between the fragmentor and skimmer electrode that accelerates the ions. Vacuum stages (A) and (B) are indicated, see figure 4.4.

cluster ions [9] (see section 4.2.2), or for the deliberate fragmentation of ions in an-alytical applications [9]. For this reason, the exit of the glass capillary is also called the fragmentor. On the other hand, the potential difference and hence the electric field between the capillary end and the skimmer produces a further push on the ions in the downstream direction, whose effects are shown in figure 4.12. For negative

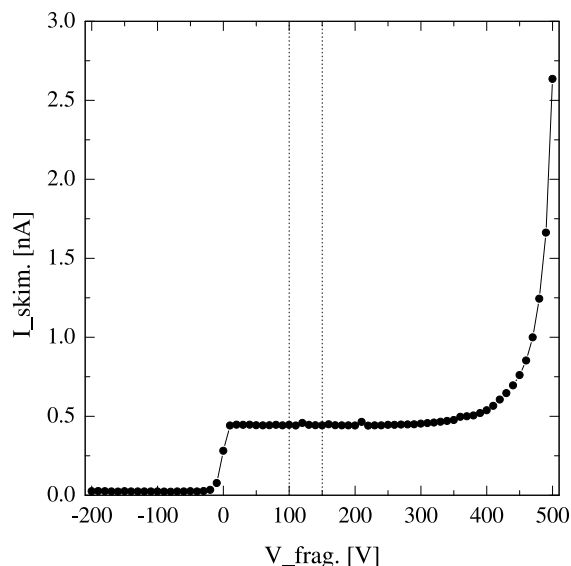**Figure 4.12:** Dependence of the skimmer current $I_{skim.}$ on the applied fragmentor voltage $V_{frag.}$. The typical working range of $+100 \text{ V} \leq V_{frag.} \leq +150 \text{ V}$ is delimited by vertical dotted lines. The spray solution contained rhodamine 6G as analyte.

values of $V_{frag.}$ all positive ions are pulled to the fragmentor electrode itself, and therefore no ion current can be measured at the skimmer electrode. Close to 0 V, but still for negative polarity of $V_{frag.}$, a rise in $I_{skim.}$ can be observed, corresponding to those ions which have gained enough kinetic energy from the supersonic expansion to overcome the counterfield generated by the negative $V_{frag.}$. By further increasing of $V_{frag.}$ up to positive values, an increase of $I_{skim.}$ up to ~ 0.5 nA can be observed. This current remains almost constant up to $V_{frag.} \sim 200$ V, from which point on an electrical discharge inside vacuum stage (A) takes place. This discharge mode can be used intentionally to generate a high yield of charged fragments of analyte ions.

A further effect of the acceleration due to the fragmentor is the improved coupling with the 1st ion guide, since a higher kinetic energy also means a better on-axis collimation, and consequently a higher transmission through the skimmer into vacuum stage (B). This can be seen in figure 4.13 where the dependence of the analyte ion current detected at the sample position (see figure 5.1) is plotted as a functions of $V_{frag.}$. A pronounced maximum in the overall transmission can be observed at
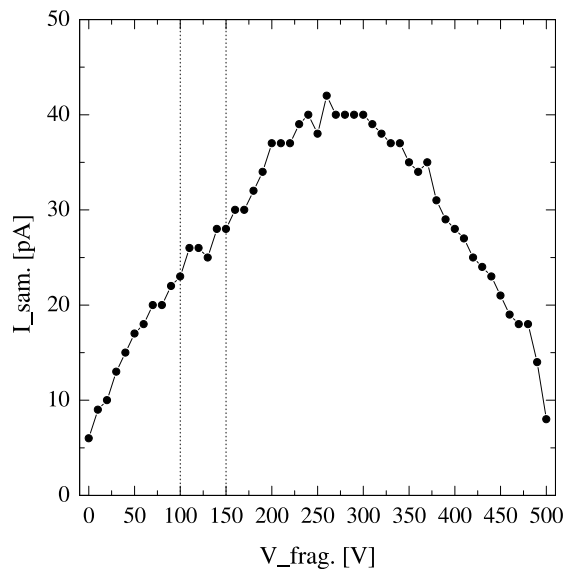
Figure 4.13: Dependence of the analyte ion current $I_{sam.}$, measured at the sample position, on the fragmentor voltage $V_{frag.}$. Two vertical lines mark the typical working range of $V_{frag.}$. The spray solution contained rhodamine 6G as analyte, as in figure 4.12.

$\approx +250$ V. Compared to figure 4.12, we are already in the range of $V_{frag.}$ values where a strong fragmentation of analyte ions and the initiation of the dc breakdown

can be expected. Therefore, we decided to work always in a range of $V_{frag.}$ values that is a compromise between a high ion transmission and a low level of analyte ion fragmentation (100 V < $V_{frag.}$ < 150 V). The decrease of $I_{sam.}$ for $V_{frag.}$ > 250 V is most probably due to the filtering properties of the two quadrupole ion guides following in beam direction. In fact, an enhanced fragmentation of the analyte ions in the nozzle-skimmer region occurs for increasing $V_{frag.}$, leading to fragments with decreasing mass-to-charge ratios which are ejected by the quadrupole ion guides. The operational principle, the design, and the characterization of these two ion guides is the subject of the following section.

4.3   Design and Characterization of the Beam Formation and Ion Guide Stage

Figure 4.14 shows the design of the beam formation stage, basically composed of two quadrupole ion guides working under different pressure conditions. In order to minimize the transport losses of analyte ions when passing them from one vacuum stage to the next, it is necessary to have a well defined ion beam, whose angular as well as energetic definition is achieved in this stage. After in-vacuum expansion into vacuum stage (A), a first angular definition of the ion beam is performed by the skimmer (7), passing only the core portion of the supersonic jet toward the entrance region of the 1st ion guide (8), which is already inside vacuum stage (B).

Note that eventually remaining neutral and polar contaminates would be almost unaffected by the electrostatic and electrodynamic forces inside the ion guide stage. Nevertheless, purely geometrical considerations (the 2nd aperture plate of ∼ 2 mm inner diameter is at a downstream distance of ∼ 40 cm) imply that the probability of having such contaminates inside the ion beam after the 2nd ion guide will be 'equal to' zero for all practical purposes.

The main task of the 1st ion guide (8) is the narrowing of the broad distribution of kinetic energy of the ion beam, which is mainly due to the repulsive Coulomb interaction among the ions during in-vacuum expansion. This is realized by so-called collisional focusing [33] (see section 4.3.1), i.e. by means of collisions between analyte

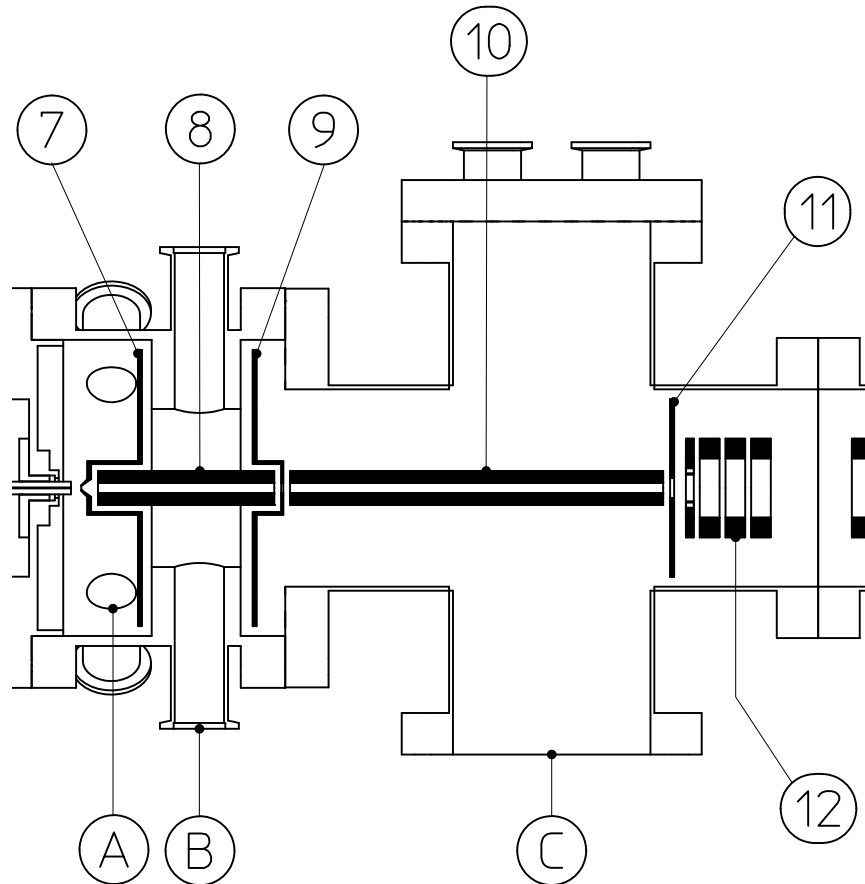**Figure 4.14:** Design of the beam formation stage: (7) skimmer, (8) 1st ion guide, (9) 1st aperture plate, (10) 2nd ion guide, (11) 2nd aperture plate, (12) 1st ion optical system, (A)–(C) denote the corresponding vacuum stages.

ions and the background gas in vacuum region (B), which is intentionally maintained at a comparatively high pressure of ~ 0.1 mbar. Although also the 1st ion guide has a mass filtering effect, this is substantially reduced and almost impossible to be theoretically predicted due to the high frequency of collisions. As a consequence, a 2nd ion guide located in the lower pressure region (C) is needed. By means of differential pumping and the 1st aperture plate (9), a vacuum of $\sim 1 \cdot 10^{-4}$ mbar can be reached in region (C) which is sufficient for avoiding collisions with the background gas and for allowing an effective mass-to-charge selection of the ion beam (see section 4.3.1), and a filtering of eventually remaining impurity and buffer ions stemming from the spray solution. After having emerged from the 2nd ion guide, the ion beam is steered and focused by the ion optical system (12). This consists of four quarter-cylindrical steering plates and three cylindrical lens elements whose main task is to optimize the transfer of the ions to the electrostatic components inside the following vacuum stage (D).

An overview of the geometrical dimensions and the operational range of the potentials applied to the different electrodes and components denoted in figure 4.14 is provided by table 4.2.

After the construction, installation, and testing of the o–TOF is finished, the pressure adjustment chamber (vacuum stage (E) of figure 4.2) together with the therein located electrostatic ion transfer system (not shown) will be installed. Finally, the ESI deposition apparatus will be connected to a UHV deposition chamber (see section 2.1), where a non-destructive deposition will be achieved by means of a final deceleration of the analyte ions in front of the substrate.

4.3.1   Quadrupole Ion Guides

The first element of the beam formation stage is constituted by the skimmer (7) which serves as a vacuum separation between the regions (A) and (B) and performs a first angular definition of the ion beam after the in-vacuum expansion. When passing the skimmer, the ion beam experiences the strongest intensity drop, from ~ 1.0 nA to ~ 75 pA, therefore any further loss in intensity should be avoided from this point on. This requirement rules out the possibility of steering, dragging and focusing the ions

name of component	geometrical dimension	applied potential
components inside vacuum stage (B): p $\sim$ 0.1 mbar		
1st ion guide (8)	rod length: 85 mm	$+0 \text{ V} \leq V_{\text{dc IG I}} \leq +20 \text{ V}$
	OD of rods: 6.0 mm	$+0 \text{ V} \leq V_{\text{ac IG I}} \leq +250 \text{ V}$
	inscribed circle: 5.2 mm	
1st aperture plate (9)	ID of orifice: 2 mm	$+0 \text{ V} \leq V_{\text{aper. 1}} \leq +15 \text{ V}$
components inside vacuum stage (C): p $\sim 1 \cdot 10^{-4}$ mbar		
2nd ion guide (10)	rod length: 185 mm	$+0 \text{ V} \leq V_{\text{dc IG II}} \leq +10 \text{ V}$
	OD of rods: 6.0 mm	$+0 \text{ V} \leq V_{\text{ac IG II}} \leq +500 \text{ V}$
	inscribed circle: 5.2 mm	
2nd aperture plate (11)	ID orifice: 2 mm	grounded
components inside vacuum stage (D): p $\sim 1 \cdot 10^{-6}$ mbar		
steering plates and	ID: 4 mm	grounded
lenses of (12)	ID: 10 mm	$-20 \text{ V} \geq V_{\text{IOS}} \geq -100 \text{ V}$

Table 4.2: Geometrical dimensions and typical voltage ranges used for several components of the ion guide tandem. Letters and numbers in parentheses refer to figure 4.14.

by simple electrostatic means. In fact, due to the broad distribution of kinetic energy after the expansion, a pure electrostatic ion guiding would result in huge transport losses when passing the ions through the apertures of ~ 2 mm inner diameter that are needed for vacuum reasons. Moreover, a broad distribution of the ion energy would be problematic for the soft-landing on solid surfaces, where a final deceleration at a fixed potential is foreseen.

As a consequence, a better definition of the ion energy becomes mandatory, which is achieved by colliding the ions with neutral gas particles at room temperature in order to 'thermalize' them. These collisions occur mainly in the interior of the quadrupole ion guide, which is driven by dc and rf voltages. The time-dependent saddle potential that is generated in such a device [34] redirects the ions toward the center line of the ion guide at each collision event, thus producing a reduction of the mean value and the spread of the kinetic energy, as well as a concentration of the ions along the axis of the ion guide [33]. The efficiency of this so-called collisional focusing [33] depends on the frequency of collisions and thus on the pressure of the background gas (typically between 0.1 and 0.3 mbar). For this reason a needle valve has been inserted in vacuum stage (B), which enables the precise adjustment of the background pressure and hence the energetic characteristics of the ion beam. A quantitative analysis will be presented in section 4.3.4.

Note, in order to improve the coupling of the ions into the 1st ion guide, a positive potential difference (typically between 5 and 10 V) is applied between the skimmer voltage and the dc voltage of the 1st ion guide. A quantitative analysis of the effects of this dragging potential difference will be presented in section 4.3.3.

A further feature that is offered by the beam formation stage is the possibility of varying the composition of the beam, i. e. of choosing the mass-to-charge ratio of the analyte ions. This is done in order to select a particular analyte out of a mixture, or to separate monomers from dimer or trimer molecular assemblies and also to definitively eliminate possible charged residues or contaminants from the ion beam. The mass selection is one function of the quadrupole ion guides but, as previously mentioned, the high pressure in the region of the 1st ion guide allows only a partial and hardly predictable mass selection. Therefore a 2nd ion guide has been placed

in the following vacuum region (C), where a pressure of $\sim 1 \cdot 10^{-4}$ mbar provides a mean free path ~ 0.6 m [35] that is larger than the length of the 2nd ion guide. This implies nearly collision free trajectories for the transported ions. Under these conditions, the behavior of the 2nd ion guide can be approximated to be that of an ideal quadrupole mass spectrometer that can be described analytically. An ideal quadrupole is composed of four parallel, infinitely long, rods of hyperbolic cross-section, which are located at the corner points of a square. Diagonally opposed rods act together and from a pair. Beside the mechanical design, also the right type of potential, being a superposition of dc and rf voltages, has to be applied to each pair of quadrupole rods. The potential landscape encountered by an ion entering the gap between the quadrupole rods can thus be written in the following form [32, 36]:

$$\Phi = \frac{(U_{dc} + V_{ac} \cos 2\pi\nu t)(x^2 - y^2)}{r_o^2} \tag{4.1}$$

where the z-axis of the coordinate system coincides with the axis of the quadrupole. U_{dc}, V_{ac}, and ν denote the dc and the rf components of the applied signal and its frequency, while r_o is the radius of the inscribed circle inside the four quadrupole rods.

The basic equations of motion of an ion of mass m and charge q inside such a potential landscape can be written in the form [32, 36]:

$$m\frac{d^2x}{dt^2} + \frac{2q(U_{dc} + V_{ac} \cos 2\pi\nu t)x}{r_o^2} = 0 \tag{4.2}$$

$$m\frac{d^2y}{dt^2} - \frac{2q(U_{dc} + V_{ac} \cos 2\pi\nu t)y}{r_o^2} = 0 \tag{4.3}$$

$$m\frac{d^2z}{dt^2} = 0 \tag{4.4}$$

It is possible to rewrite these equations in the form of Mathieu's differential equations of motion[3], whose treatment leads to an expression for the mass-to-charge ratio of the ions that are able to pass through the quadrupole. In the theoretical limit of infinite mass resolution of an ideal quadrupole, the mass-to-charge ratio of the ions that are allowed to pass the quadrupole can be calculated according to the following equation [32, 36]:

$$\frac{m}{q} = 1.385 \times 10^7 \frac{V_{ac}}{\nu^2 r_o^2}, \tag{4.5}$$

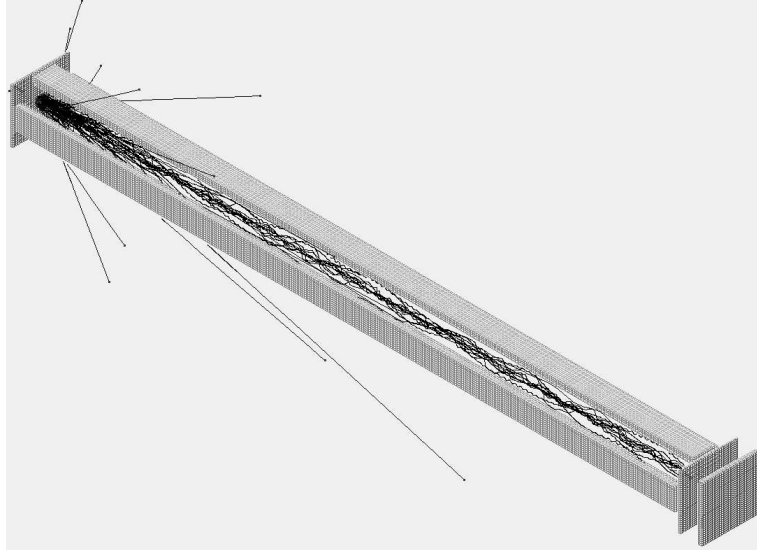[3]A profound discussion of the Mathieu differential equation can be found in [34, 37].

Figure 4.15: Simulated transport behavior of the 2nd ion guide. Only ions within the mass-to-charge transport band are able to pass the 2nd ion guide, acting as mass-to-charge filter. In the simulation 15 V and 0 V were applied to the entrance and the exit aperture of the ion guide, while the corresponding dc and rf components of the applied ion guide signal measured 15 V and 450 V. Data courtesy of S. Rauschenbach [39].

where the mass m is measured in atomic mass units, the charge q in units of the elementary charge, the amplitude V_{ac} in V, and the frequency ν in Hz.

Equation 4.5 indicates how a particular mass-to-charge pass condition can be selected by acting on the quadrupole's frequency and amplitude parameters. Although giving a first qualitative description, the ideal quadrupole approximation is not sufficient for a quantitative analysis of a real ion guide, being composed of finite rods of circular cross-section. Instead, a numeric simulation is needed in order to model the transport and mass selecting behavior in a realistic manner. Figures 4.15 and 4.16 show the results of such simulations, generated with the SIMION 7.0 ion optics modelling software package [38], demonstrating the ion guide's transport and mass selection properties, respectively. By following the different trajectories in figure 4.15, it can be seen that, depending on their initial parameters, the simulated ions are either ejected or transported by the 2nd ion guide. Figure 4.16 shows further, that under realistic conditions a mass-to-charge transport band exists for ions, whose logarithmic width shows only a weak dependence on the applied frequency ν, whereas its
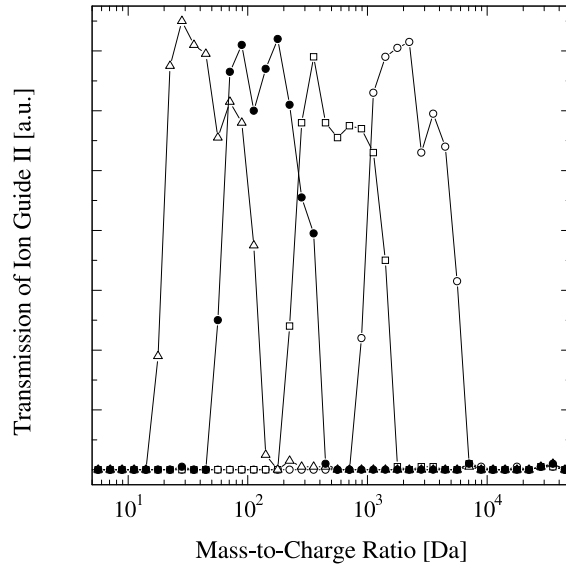
Figure 4.16: Mass-to-charge transport band of the 2nd ion guide in dependence of the applied rf frequency ν ($\circ$: 0.5 MHz, $\square$: 1.0 MHz, $\bullet$: 2.0 MHz, $\triangle$: 3.5 MHz). The start parameters were uniformly chosen in a range from $10^1 - 10^7$ amu in mass, from $1 - 100$ elementary charges, and from $10^0 - 10^5$ eV in kinetic energy. Only the frequency ν was varied in the frame of the SIMION 7.0 simulation, while all further dc and rf voltage values where kept constant. Data courtesy of S. Rauschenbach [39].

midpoint can be amply varied over several orders of magnitude. On the other hand, changes of the amplitude of the driving rf voltage produce only smaller variations in the pass conditions and simultaneously increase the width of the transport band, therefore reducing the selectivity of the mass-to-charge filter [39]. This difference can be regarded as a signature of the different dependence (linear and quadratic, respectively) of the peak mass-to-charge ratio on the amplitude and the frequency of the rf signal in the case of an ideal quadrupole (see equation 4.5). Moreover, this simulation tells us that the rf frequency is the best parameter to be varied in order to adjust the mass-to-charge composition of the ion beam and to simultaneously filter eventually still remaining impurity and buffer ions out of the ion beam. At the present stage, the simple design of the control electronics (see section 4.3.2) does not allow any frequency variation. Therefore, referring to equation 4.5, the mass-to-charge pass condition can currently only be altered by changing V_{ac}. According to the simulated values in figure 4.16, the driving parameters of the 2nd ion guide should correspond to pass conditions between 50 and 400 Da. Although not allowing any mass selection, this configurations is compatible with the transport of a broad range of analyte ions generated by ESI, as demonstrated by the electrospray deposition experiments in chapter 5.

Note that in analogy with the dragging and dc coupling of the ions from the skimmer into the 1st ion guide, a positive potential difference is also applied between the dc voltage of the 1st ion guide and the 1st aperture plate, and between the 1st aperture plate and the dc voltage of the 2nd ion guide (see figure 4.14). The same procedure is applied for dragging the ions from the second ion guide, through the 2nd aperture plate to the 1st ion optical system. In other words, the transport of the ions through the whole beam formation stage is supported by a continuous reduction of dc voltages applied to the skimmer (7), the 1st ion guide (8), the 1st aperture plate (9), the 2nd ion guide (10), the 2nd aperture plate (11), and the 1st ion optical system (12).

4.3.2   RF Electronics

For the practical operation of the beam formation stage, it is important to keep the same frequency and a stable phase shift between the signals applied to the 1st and

component	rel. V_{dc}	rel. V_{ac}
1st ion guide:	100%	50%
1st aperture plate:	75%	–
2nd ion guide:	50%	100%
2nd aperture plate:	0%	–

Table 4.3: Relative dc and ac output-ratios of the ion guide electronics. V_{dc} and V_{ac} can be varied independently.

2nd ion guide. This is achieved by the use of a single resonant circuit, used in parallel for both ion guides. Due to the higher pressure in the region of the 1st ion guide, the applied ac voltage has to be reduced in order to prevent electrical discharges. This can be achieved by means of a capacitive divider, reducing the ac voltage applied to the 2nd ion guide by a factor of 2. On the other hand, the dc voltage applied to the 1st ion guide has to be higher in order to maintain the axial dc field at the exit side of this ion guide, facilitating the transfer of the ions into the 2nd ion guide. This is done by simple resistive partitioning elements in the electronics, furnishing fixed dc voltage ratios between the various output potentials: 100% on the 1st ion guide, 75% on the 1st aperture plate in between the two ion guides, and 50% on the 2nd ion guide. The highest dc potential ($\sim$ 200%) is applied to the skimmer, in order to pass the highest possible ion intensity into the 1st ion guide (see table 4.3). The rf electronics themselves are able to provide maximal dc and rf ion guide signals of $V_{dc\ IG\ I}^{max} = +20$ V and $V_{ac\ IG\ II}^{max} = 0.5$ kV, while $V_{skim.}$ can be adjusted independently. At present, the operational frequency ν of the resonant rf circuit is tuned to 2.0 MHz.

In order to transport the analyte ions as effectively as possible through the ion guide tandem, it is necessary to address the most stable oscillation mode of the rf circuit. Its frequency ν is very sensitive to the inductance L and the capacity C of the total load, which in practice depends on several parameters such as the length and separation of the ion guide rods as well as the type and the length of the input leads used. Consequently, it is important that these values are checked after each maintenance of the ion guide in order to ensure the reproducibility of all characteristics of the beam formation stage. Table 4.4 summarizes various capacity

vacuum stage	stage pressure	$C_{pair-to-pair}$	$C_{pair-to-ground}$
(B) - 1st ion guide:	0.1 mbar	(20 ± 4) pF	(40 ± 8) pF
(C) - 2nd ion guide:	$1 \cdot 10^{-4}$ mbar	(30 ± 6) pF	(40 ± 8) pF

Table 4.4: Various capacities describing the ion guide tandem. The values of the capacities include that of the utilized input leads. The errors have been estimated based on the variation range of the individual measurement readings.

values for both ion guides, measured between the two neighboring pairs of ion guide rods, and on a single rod-pair with respect to the surrounding part of the grounded chamber.

In order to minimize the disturbance of a measuring apparatus on the rf circuit while monitoring its oscillatory behavior, a control point located in parallel to the main inductance of the rf electronics is used to connect an oscilloscope with a low capacity HV probe head. Such a setup has to be used during the tuning of the ion guide electronics which should be done according to the following guideline: I) By means of the 1st potentiometer, being part of a simple voltage divider, set all dc voltages of the ion guide tandem to zero. II) Allow the resonant circuit to oscillate with the maximal V_{ac} value by means of the 2nd potentiometer, controlling the amplification factor of the rf electronics. III) With the help of the 3rd potentiometer, that controls the resonance condition of the of the rf circuit, it is possible to adjust the most stable oscillation with maximal peak-to-peak voltage. IV) Last, the dc potentials (1st potentiometer) and hence the axial dc fields have to be adjusted in order to optimize the transport behavior of the whole beam formation stage and to maximize the deposition current.

It should be noted that, although the most stable oscillation mode is tuned correctly, not all ac voltages are stable in time. Figure 4.17 shows an example of this complex behavior, resulting in the appearance of gaps in the depicted V_{ac} dependent transport curve. After a few seconds of proper oscillation at the original V_{ac} setting, a shift toward lower and more stable V_{ac} voltages can be observed, leading to the gaps in the transport curve. We note that the simultaneous rise in the analyte current $I_{steering\ plates}$ for increasing V_{ac} values might be ascribed to two different effects: An

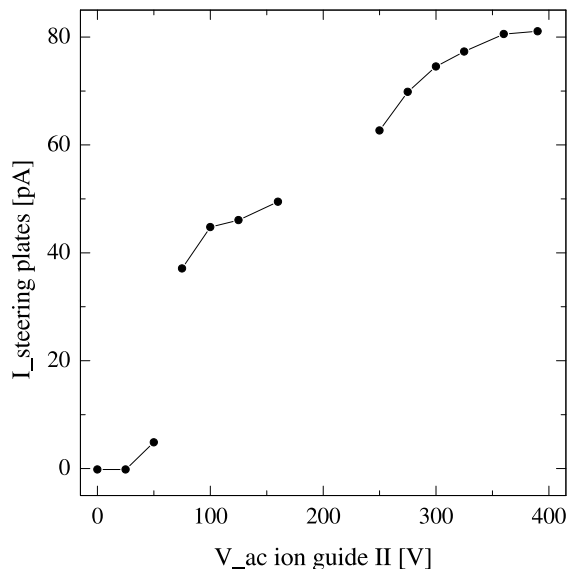**Figure 4.17:** Dependence of the analyte current $I_{\text{steering plates}}$ as a function of the V_{ac} value applied to the 2nd ion guide. The current was measured at the steering plates behind the 2nd ion guide, while keeping the 1st lens element of the ion optical system at a retarding potential of $+30$ V (see figure 4.14). The spray solution contained rhodamine 6G as analyte.

increasing transport efficiency of the rhodamine 6G analyte ions in the 1st ion guide, and a shift of the mass-to-charge transport band of the 2nd ion guide.

4.3.3   Influence of the DC Drag Potential Differences on the Analyte Current

In this section the effect of the dc potential on the ion transmission of the beam formation stage will be quantitatively analyzed. First, the influence of the ion accelerating dc field between the skimmer and the 1st ion guide will be presented. Afterwards, we will examine the effect of the dc potentials applied to the ion guide tandem.

Figure 4.18 shows normalized rhodamine 6G and bovine albumin currents measured at the sample position (see figure 5.1) as a function of the applied skimmer voltage $V_{\text{skim.}}$. The vertical dotted line marks the value of the dc component of the 1st ion guide, set to $+10$ V during the experiment. Note that $V_{\text{frag.}}$ was fixed to $+150$ V, lying within the range of potential differences between fragmentor and skimmer, for which only minor changes in the skimmer current could be observed
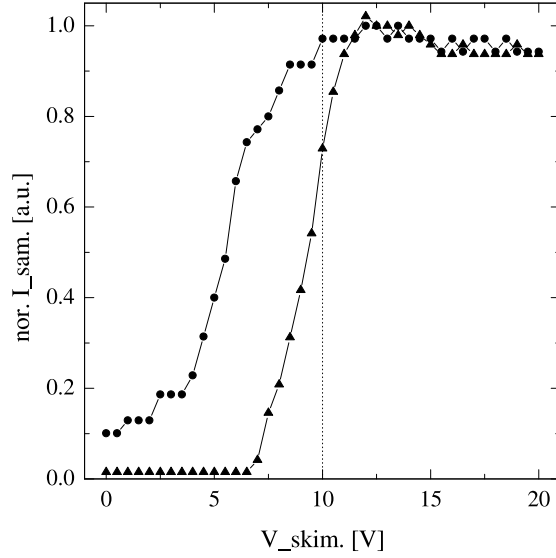
Figure 4.18: Dependence of the current $I_{sam.}$ on the applied skimmer voltage $V_{skim.}$. $V_{dc\ IG\ I}$ was fixed to +10 V during the experiment, which is marked by the vertical dotted line. The spray solutions used contained either rhodamine 6G (▲) or bovine albumin (●). Typical examples of solution composition and utilized spray and voltage parameters are summarized in tables 4.5 and 4.6.

(compare figure 4.12 on page 38). Therefore, the changes measured in $I_{sam.}$ can be interpreted as being caused only by variations in the coupling of the ions into the 1st ion guide.

After a steep rise in the analyte current for smaller values of $V_{skim.} \leq +10$ V, both I-V curves show a saturation in the collected analyte current for higher values of $V_{skim.}$ ($V_{skim.} \geq +10$ V). This saturation can be ascribed to the ion accelerating dc field between the skimmer and the 1st ion guide, effectively coupling the ions into the 1st ion guide. The two different onset values of the rising behavior of $I_{sam.}$ might be due to the different kinetic energies of the two analytes, gained during the aerodynamic acceleration .

The normalized I-V curves depicted in figure 4.19 correspond to experiments where $V_{skim.}$ was held at a fixed value, while changing the dc component $V_{dc\ IG\ I}$ of the applied rf signal. In order to perform the experiment within the region of current saturation of figure 4.18, $V_{skim.}$ was fixed to +25 V during the experiment. This implies that all variations of the analyte current $I_{sam.}$, being measured at the sample

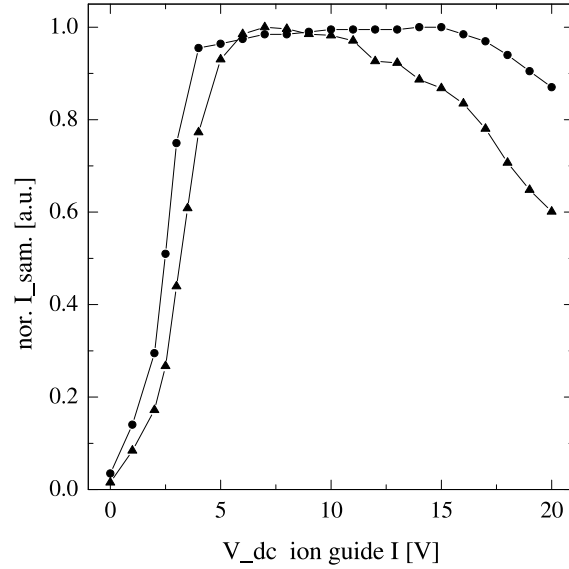**Figure 4.19:** Normalized analyte current $I_{sam.}$ versus the dc component $V_{dc\ IG\ I}$ of the applied rf signal. The rhodamine 6G I-V curve is marked by ▲, whereas the bovine albumin I-V curve is denoted by ●. The value of $V_{skim.}$ was set to $+25$ V during the experiment.

position (see figure 5.1), can this time be attributed to phenomena occurring inside the 1st and the 2nd ion guide. Remember that according to table 4.3, the dc component $V_{dc\ IG\ I}$ applied to the 1st ion guide also determines the potential and the dc component of the rf signal supplied to the 1st aperture plate and the 2nd ion guide, respectively.

Both I-V curves in figure 4.19 show a steep increase of the measured analyte current $I_{sam.}$ in the range of $V_{dc\ IG\ I} < 5$ V. Thereafter, the albumin I-V curve shows a plateau followed by a small reduction, while the rhodamine 6G I-V curve shows a weak maximum followed by a more pronounced reduction in the transmission efficiency. Referring to table 4.3, no dragging effect is present in the case of $V_{dc\ IG\ I} = 0$ V. Although the ion accelerating dc potential difference between the skimmer and the 1st ion guide transfers the analyte ions to the ion guide, no deposition current $I_{sam.}$ can be measured. This shows clearly that in the absence of any dc potential difference in between the ion guides, no ions can be transported to the exit of the beam formation stage. In contrast, with increasing dc component $V_{dc\ IG\ I}$ of the rf signal, the dragging dc field between the two ion guides leads to an improved transport of the ions and hence to increasing $I_{sam.}$. The particular shape of the I-V curves for $V_{dc\ IG\ I} > +5$ V

	dye solution	protein solution
analyte: product number:	rhodamine 6G 25,243-3 (Aldrich)	bovine albumin A-1900 (Sigma)
composition of the used spray solution:	10 ml H_2O 10 ml CH_3CH_2OH 100 μl CH_3COOH 1.5 mg rhodamine 6G	10 ml H_2O 10 ml CH_3CH_2OH 100 μl CH_3COOH 1.5 mg bovine albumin
spray solution flow: countergas flow:	12 $\frac{\mu l}{min}$ at 0 bar 10 $\frac{l}{min}$ at 150 °C	12 $\frac{\mu l}{min}$ at 0 bar 10 $\frac{l}{min}$ at 150 °C

Table 4.5: Spray solution composition and corresponding supply parameters of the electrosprayed rhodamine 6G and bovine albumin solutions.

might be related to the complex interplay of the collisional focusing and the mass-to-charge ratio dependent ion transport (see section 4.3.1), and the unequal mobility of the different analyte ions.

In conclusion, the approximate relation $V_{skim.} \simeq 2 \cdot V_{dc\ IG\ I}$ can be noted as an experimental rule of thumb. Furthermore, the choice of $V_{dc\ IG\ I} \geq 7.5$ V enables an effective transport of the analyte ions, which is necessary for an optimum ion transmission through the whole ESI deposition apparatus.

4.3.4 Measurement of the Kinetic Energy of the Analyte Ions

Determining the energy of the analyte ions that emerge from the ion guide tandem is of crucial importance for various following steps in the realization of the whole ESI deposition apparatus, such as the final soft-landing of analyte ions onto the substrate within the UHV environment.

The measurements were done by mounting a simple 'kinetic energy high pass filter' ~ 23 cm behind the exit of the 2nd ion guide. It basically consists of a retarding grid of 50 meshes per inch (wire diameter: $\sim 51\ \mu$m, open grid area: 81%), which is spot-welded to a ring-like stainless steel plate of 20 mm inner diameter, and another

	dye solution	protein solution
analyte:	rhodamine 6G	bovine albumin
voltages applied to the ESI-head		
$V_{ent.}$:	-3.7 kV	-3.7 kV
$V_{cap.}$:	-4.1 kV	-4.1 kV
$V_{frag.}$:	$+150$ V	$+150$ V
voltages applied to the ion guide tandem		
$V_{skim.}$:	$+24.6$ V	$+24.6$ V
$V_{dc\ IG\ I}$:	$+20$ V	$+20$ V
$V_{ac\ IG\ I}$:	170 V	170 V
$V_{aper.\ I}$:	$+15$ V	$+15$ V
$V_{dc\ IG\ II}$:	$+10$ V	$+10$ V
$V_{pp\ IG\ II}$:	680 V	680 V
$V_{aper.\ II}$:	grounded	grounded
voltages applied to the ion optical system (IOS)		
$V_{steering\ plates}$:	grounded	grounded
$V_{lens\ 1\ of\ IOS}$:	-26.5 V	-26.5 V
$V_{lens\ 2\ of\ IOS}$:	-16.5 V	-16.5 V
$V_{lens\ 3\ of\ IOS}$:	-16.5 V	-16.5 V
voltages applied to the funnel lens system		
$V_{funnel\ lens\ 1}$:	-100 V	-100 V
$V_{funnel\ lens\ 2}$:	-150 V	-150 V
$V_{funnel\ lens\ 3}$:	-200 V	-200 V

Table 4.6: Summary of voltages used during rhodamine 6G and bovine albumin deposition.

circular plate placed ~ 5 mm behind the grid, collecting the analyte current. All ions with an (axial) kinetic energy (per charge) lower than $\sim V_{grid}$ are deflected toward the grounded walls of the vacuum chamber, while those with a higher kinetic energy (per charge) are able to pass through the grid, being recorded at the collection plate. Quantitatively,

$$I(V_{grid}) = I_\circ \left(1 - \int_0^{V_{grid}} f(\widetilde{E})\, d\widetilde{E}\right), \tag{4.6}$$

where $I_\circ$ is the total intensity of the beam, and $f(E)$ is the kinetic energy distribution of the analyte ions, that can be derived from the measured current as

$$f(E) \propto -\frac{dI(V)}{dV}. \tag{4.7}$$

Figure 4.20 depicts typical I-V curves of bovine albumin (left panel) and rhodamine 6G (right panel), showing the expected nearly step-like behavior when increasing the retarding V_{grid} potential. The respective energy distributions are also
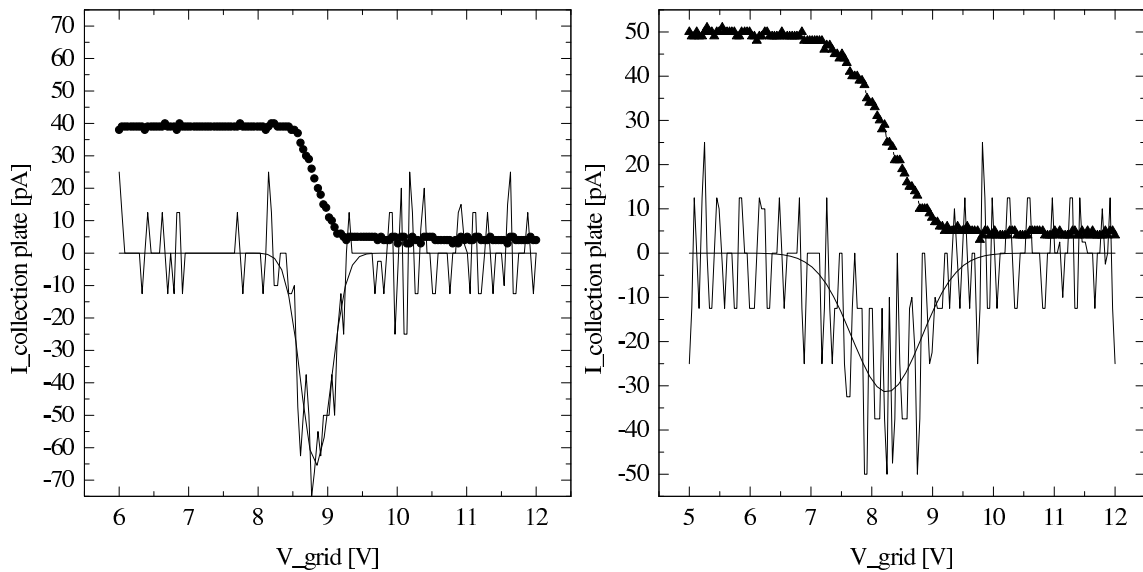

Figure 4.20: Thick data points: Ion energy high pass I-V curves of bovine albumin (left panel) and rhodamine 6G (right panel). Thin lines: Numerical derivative and fitted Gauss profile of the respective I-V curves. Corresponding $V_{center} \pm$ FWHM values of 8.8 ± 0.5 eV (bovine albumin) and 8.3 ± 1.3 eV (rhodamine 6G) are obtained. The background pressure in the region of the 1st ion guide measured 0.1 mbar during both experiments.

showed as obtained by numerical differentiation of the high pass curves and fitting

by means of a Gaussian distribution (thin lines in figure 4.20). The center position V_{center} of the Gaussian can be interpreted as the mean (axial) kinetic energy of the ion beam, while its **f**ull **w**idth at **h**alf **m**aximum (**FWHM**) might be interpreted as a measure of the energy spread.

In our experimental setup, the energetic definition of the ion beam depends strongly on the degree of collisional focusing (see section 4.3.1), and hence on the operational parameters of the beam formation stage. Moreover, the dc component $V_{dc\ IG\ I}$ of the applied rf signal and the background pressure in the region of the 1st ion guide show a pronounced influence on the shape of the retarding grid I-V curves. In fact, the kinetic energy of the analyte ions is determined by the dc potential of the point at which they stop colliding with the background gas. Collisions between neutral and charged beam components surely take place during the in-vacuum expansion, but may also occur inside the ion guides, depending on the pressure conditions in their corresponding vacuum stages. Therefore, in general, the energy distribution of the analyte ions will be a complex function of the dc components applied to the ion guide tandem, and of the operational pressures adjusted in the vacuum stages (B) and (C) of the beam formation stage (see figure 4.14).

In order to quantitatively determine this dependence, we performed measurements similar to those of figure 4.20 as a function of the pressure in the region of the 1st ion guide. The pressure was adjusted by means of simple valves in front of the turbomolecular drag pumps of vacuum stage (B), enabling the control of their effective pumping speed. Figure 4.21 shows examples of ion energy high pass I-V curves for bovine albumin (left panel) and rhodamine 6G (right panel), while the operating pressure of the 1st ion guide was changed from 0.1 mbar (far right curve) to 0.7 mbar (far left curve) in steps of 0.1 mbar.

All parameters describing the I-V curve, being the magnitude of the beam current, the center position, and the width of the descending region of the curve, show a pronounced pressure dependence. With increasing background pressure in vacuum stage (B), the magnitude of the bovine albumin current stays nearly constant, whereas the corresponding value of the rhodamine 6G ions increases by $\sim 40\%$. This is probably due to the large collisional cross-section of bovine albumin, leading to an
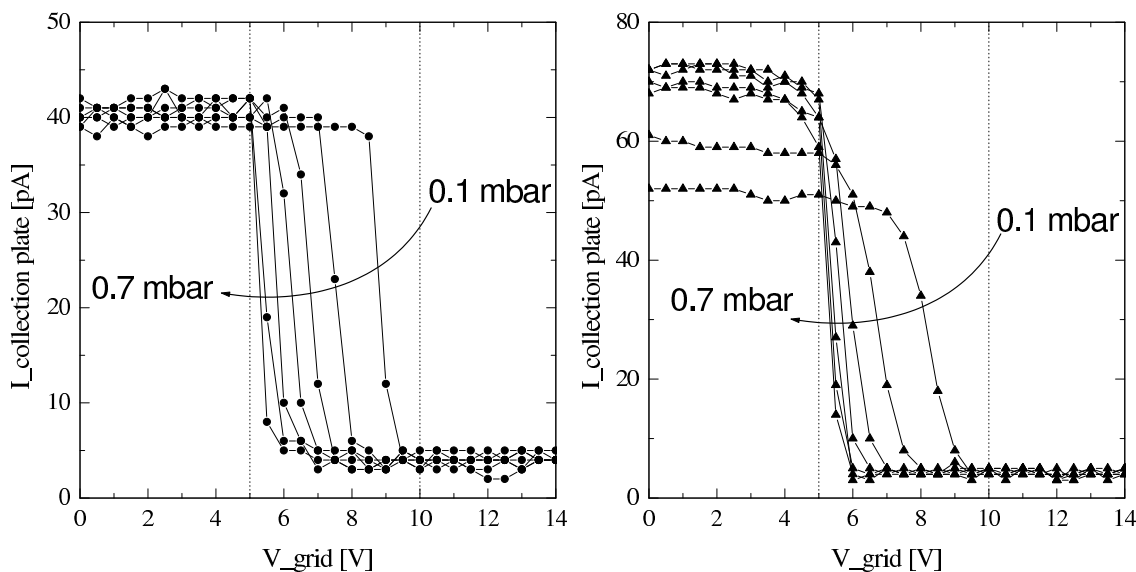
Figure 4.21: Ion energy high pass curves for bovine albumin (●) and rhodamine 6G (▲) as analyte substance. The operating pressure of the 1st ion guide was increased from 0.1 mbar to 0.7 mbar in steps of 0.1 mbar. With increasing background pressure the descending step region of the I-V curves started to shift as indicated by the arrow. Additionally, an increase of the beam intensity can be observed in the case of rhodamine 6G (▲), whereas for bovine albumin (●) no significant changes are observable. The vertical dotted lines mark the dc components of the rf signals applied to the 1st and the 2nd ion guide ($V_{dc\ IG\ I}$= +10 V, $V_{dc\ IG\ II}$= +5 V). Further information on the composition of the spray solutions, the utilized atomization parameters, and the applied set of (high) voltages can be found in tables 4.5 and 4.6.

axial concentration behavior inside the 1st ion guide that is nearly independent of the background pressure. In the case of rhodamine 6G, the corresponding small collisional cross-section results possibly in the continuation of the axial concentration of the analyte ions, while increasing the pressure. Hence, when raising the operational pressure, higher rhodamine 6G beam intensities, measured as increasing analyte currents, are passed to the 2nd ion guide.

Highly resolved I-V curves were recorded, differentiated, and fitted with a Gaussian distribution as described above. The resulting V_{center} and FWHM values of the energy distributions are depicted in figure 4.22 as a function of the background pressure in the region of the 1st ion guide. The left panel shows a reduction of the
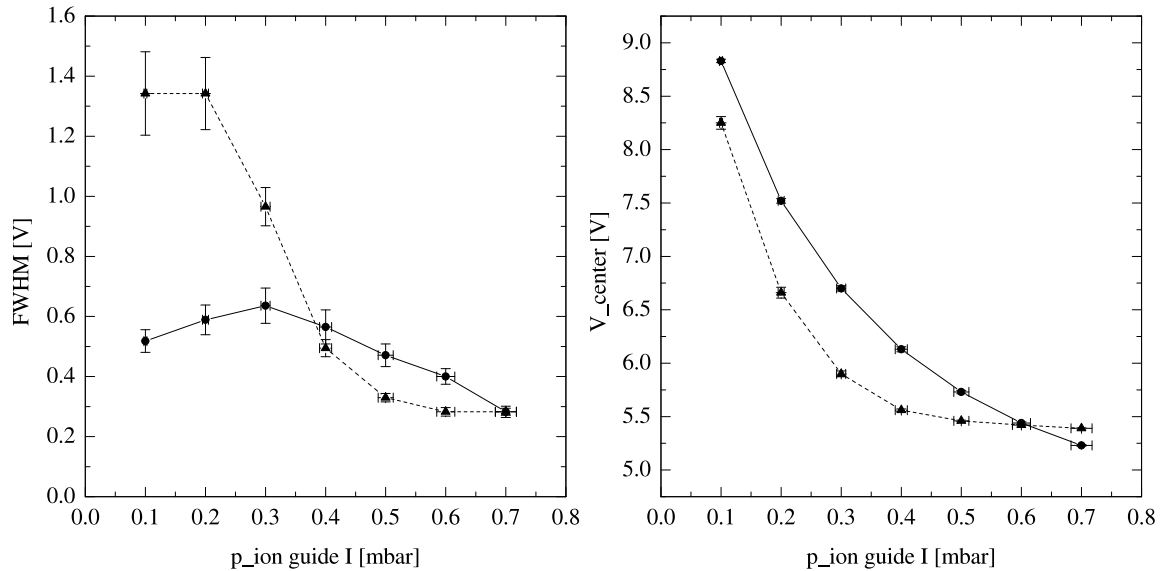

Figure 4.22: Pressure dependence of the center position V_{center} (right panel) and the corresponding FWHM (left panel) of the fitted Gaussian distribution for bovine albumin (•) and rhodamine 6G (▲).

FWHM of the distribution of kinetic energy with increasing background pressure, demonstrating the effect of 'phase space' compression inside the 1st ion guide. The fine details, such as the small increase before the decrease in the fitted albumin FWHM values, might be attributed to the complex interplay of collisional focusing, the pressure dependent transport properties of the ion guide tandem, and intrinsic differences in the ion mobility of the two analytes. Of course, besides reducing the FWHM, the collisions also reduce the mean kinetic energy of the analyte ions. The

right panel of figure 4.22 shows that with decreasing pressure the kinetic energy (per charge) nears the dc component of the rf signal applied to the 1st ion guide (here: $V_{dc\ IG\ I} = +10$ V). This is because, as already said, the kinetic energy of the ions is determined at the point where no collisions, and hence no further reductions in kinetic energy take place, being typically at a position in between the exit of the 1st and the entrance of the 2nd ion guide. With increasing pressure, the dc component $V_{dc\ IG\ II}$ of the 2nd ion guide can be assigned as the lower limit of the kinetic energy of the ions (here: $V_{dc\ IG\ II} = +5$ V). In fact, with increasing background pressure in the region of the 1st ion guide, the pressure in the 2nd ion guide also starts to increase, leading to a continuation of the kinetic energy regulation by means of collisional focusing inside the 2nd ion guide, and therefore to an additional reduction of V_{center} (see figure 4.22).

On one hand, a high pressure inside the region of the 1st ion guide is thus favorable with regard to the achievable degree of collisional focusing. On the other hand, the resulting rise of pressure in the region of the 2nd ion guide influences its mass-to-charge selecting action. Therefore, a pressure between $0.1 - 0.3$ mbar inside vacuum stage (B), containing the 1st ion guide, represents an optimum compromise with respect to all operational demands of the ESI deposition source.

In conclusion, it should be noted that all numbers and values presented in this chapter are analyte specific, and in principle they should be measured and adjusted according to simultaneously recorded mass spectra. Nevertheless, the two preceding sections demonstrate that although rhodamine 6G and bovine albumin are rather different analytes, the same set of operational parameters (see tables 4.5 and 4.6) can be used to successfully process these substances all the way up to their deposition onto the substrate.

Chapter 5

Experimental Results

As demonstrated in the previous chapter, the analyte ion beam is spatially and energetically well defined, and can be used for first in-vacuo electrospray deposition experiments with sensitive analytes, such as large thermolabile biomolecules. At the present stage of construction of the ESI source, these experiments differ only in the vacuum conditions (background pressure during deposition $\sim 1 \cdot 10^{-6}$ mbar) from our ultimate goal, the soft-landing and characterization of thermolabile analytes under well defined UHV conditions (pressure $\sim 1 \cdot 10^{-10}$ mbar). Of course, at present we are restricted to less reactive substrates such as e.g. gold films on mica, O passivated Si wafers, and **h**ighly **o**riented **p**yrolytic **g**raphite (**HOPG**).

The experimental results presented in the following paragraphs demonstrate the feasibility of the ESI deposition technique for various types of analyte systems of different molecular mass. These preliminary results can be regarded as a proof of the deposition principle, being demonstrated for small organic molecules, large biomolecules, and metal nanoparticles. The remaining open questions in the interpretation of the experimental data are mainly due to the lack of mass spectrometric information on the deposited analyte ions that would allow a better understanding of the presented morphological data.

5.1 Sample Preparation Geometry

Figure 5.1 shows the deposition geometry used during sample preparation. Compared to figure 4.2 on page 22, the therein depicted chamber (D), housing the TOF analyzer, is replaced by a smaller deposition chamber (d), that contains an electrostatic funnel lens system (13) together with the mounted substrate (14). The surface of
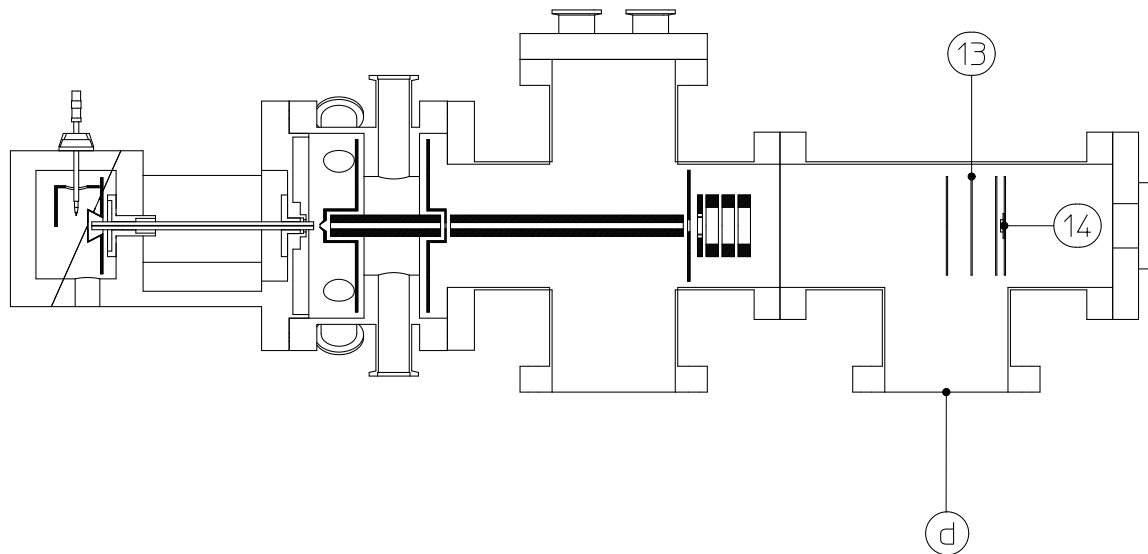

Figure 5.1: Deposition geometry during sample preparation: A special deposition chamber (d) with a funnel lens system (13) in front of the substrate (14) are used to guide and to deposit the analyte ions onto the substrate.

the substrate is close behind an assembly consisting of three concentrically mounted stainless steel plates (thickness: 1 mm, OD: 80 mm, relative distances: 20 mm) with reducing inner diameters (1st plate: 20 mm, 2nd plate: 5 mm, 3rd plate: 2 mm). The purpose of this funnel lens system is to collect as many ions as possible for the subsequent deposition on the substrate, and to restrict and locate the deposition spot on the ideal axis. Figure 5.2 shows a schematic of the deposition setup together with the corresponding computer controlled reading of the analyte current at the sample position. In order to insert the sample directly into the AFM setup after preparation, the substrate is glued onto a metallic disc with the help of a conductive silver paste. During analyte deposition, which occurs at room temperature at a pressure of $\sim 1 \cdot 10^{-6}$ mbar, the substrate-disc unit is screwed to a small metal sheet mounted
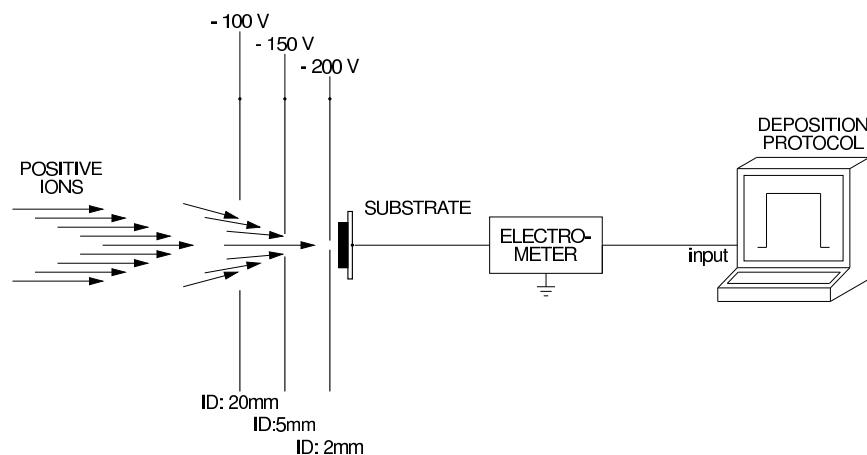
Figure 5.2: Close-up view of the deposition geometry: Decreasing voltages are applied to the plates of the funnel lens system in front of the substrate. The deposited analyte current is recorded during sample preparation.

close (distance: ~ 3 mm) to the rear of the last plate of the funnel lens system.

In order to prevent the entrance and an eventual deposition of e.g. dust particles and droplets onto the substrate during venting of the ESI source, the following protocol is used to finish the deposition: First, the polarity of the voltage applied to the 1st lens of the ion optical system is inverted, which terminates the analyte deposition at a certain time. Thereafter, the supplied analyte flow is stopped, and all applied high voltages are turned off. Next, the deposition source is vented, while the countergas flow is still kept on. Finally, the sample holder together with the prepared sample is dismounted.

Afterwards, the morphology of the deposited analyte structures is examined under ambient conditions by means of tapping mode AFM on a Digital Instruments Nanoscope IIIa system. Tapping mode cantilevers (type: NCH-W, purchased from Nanosensors) with a spring constant of $C = 38 - 68 \frac{N}{m}$ were used for AFM imaging.

5.2 Spatial Definition and Temporal Stability of the Deposition Process

Figure 5.3 shows a series of 9 AFM images that was taken across the edge of the deposition spot in the case of albumin deposition (see section 5.5). The lateral distance

between consecutive images is always 0.3 mm. The overall almost constant surface
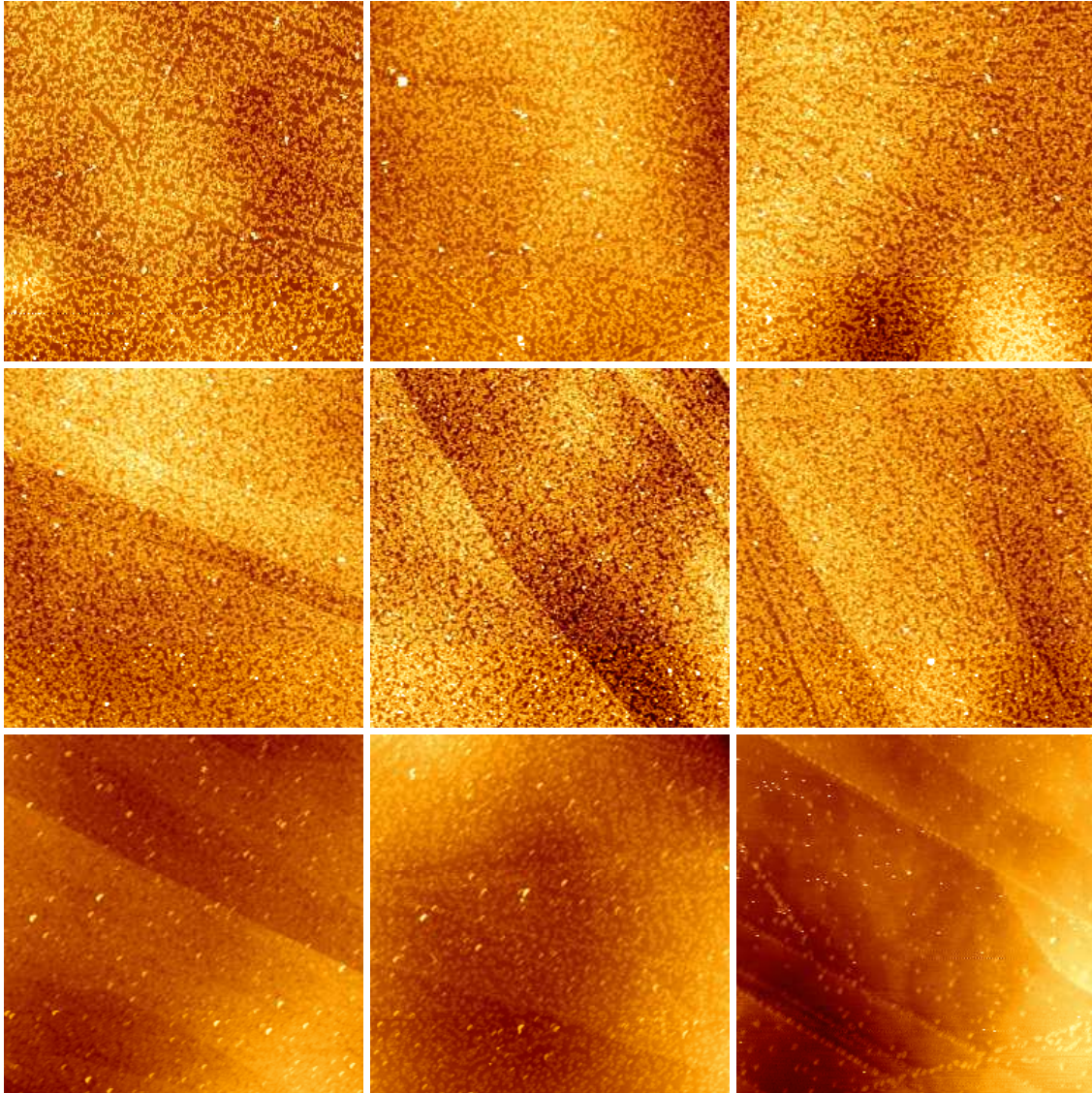

Figure 5.3: Series of 9 AFM images taken across the edge of a deposition spot on HOPG, covered by bovine albumin. The lateral distance between consecutive images is ~ 0.3 mm (image size: $5~\mu$m $\times$ $5~\mu$m). Small variations in the surface coverage are followed by a fast decrease in the last 3 imaging steps. A mean current of ~ 35 pA was deposited for 1 h 15 min during sample preparation, while the HOPG substrate was at room temperature.

coverage is followed by a sudden decrease for the last 3 images. This shows clearly that the deposition spot is well defined and its lateral size (~ 3 mm) is roughly restricted by the dimension of the pinhole in the last plate of the funnel lens system (~ 2 mm).

During each sample preparation, the deposited analyte ion current was recorded in the form of a deposition protocol in order to document the course of the deposition process. Figure 5.4 shows two examples of such a protocol for the deposition of rhodamine 6G (see section 5.4) on two successive days. Both current protocols were
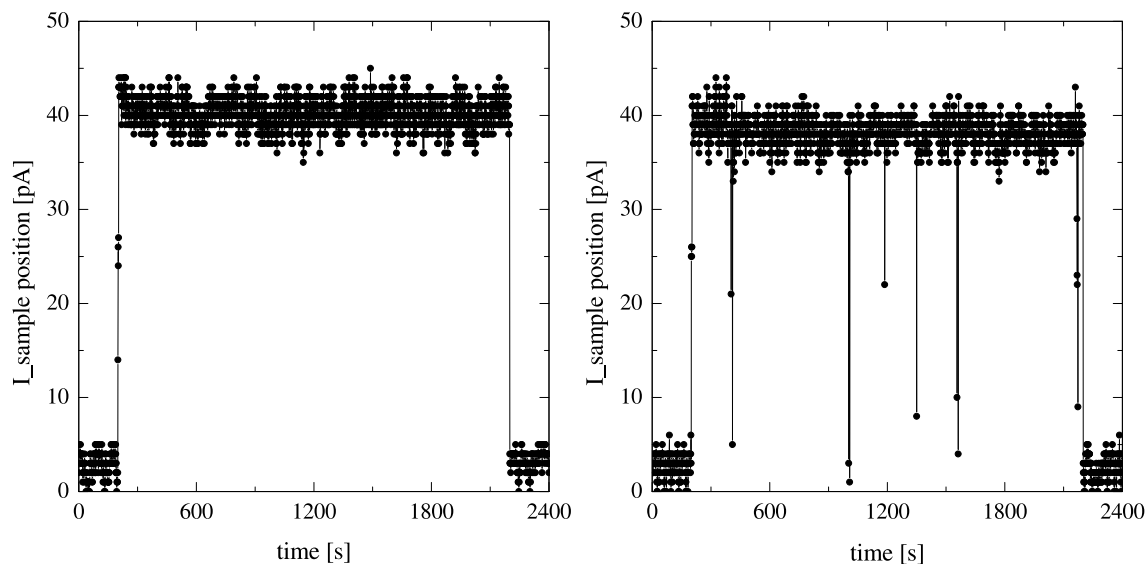

Figure 5.4: Examples of rhodamine 6G deposition protocols recorded under identical conditions on two following days.

recorded for the same set of operational parameters and the same spray solution, generally showing typical instabilities. As already mentioned before (see section 4.2.1), these instabilities probably result from an imbalance between the supply of analyte solution to the ESI-needle and its consumption during the ESI process. Nevertheless, they typically concern only a minor time fraction of the whole deposition ($< 2\%$) and can therefore be ignored for all practical purposes.

After all deposition parameters have been set, it is possible to switch the deposition current on and off by simply changing the polarity of the voltage applied to e.g. the 1st lens of the 1st ion optical system (see figure 4.14).

analyte:	5 nm Au colloidal suspension	
product number:	G-1402 (Sigma)	
spray solution:	4 ml	H_2O
	5 ml	CH_3CH_2OH
	100 μl	CH_3COOH
	1 ml	Au colloidal suspension
spray solution flow:	12 $\frac{\mu l}{min}$	at 0 bar
countergas flow:	5 $\frac{l}{min}$	at 150 °C

Table 5.1: Composition, supply, and atomization parameters of the Au colloidal solution used for ESI.

5.3 Electrospray Deposition of Colloidal Au on HOPG

Within this section the feasibility of the electrospray deposition of colloidally suspended Au nanoparticles on HOPG will be demonstrated. HOPG was purchased from ATOS (quality: ZYB, substrate size: 10 mm × 10 mm) and used as substrate after cleavage by means of an adhesive tape. The colloidal base suspension was purchased from Sigma (product number: G-1402) and besides the Au nanoparticles (with a nominal size ranging from 3.5 to 6.5 nm) also contains approximately 0.01% $HAuCl_4$ in 0.01% tannic acid with 0.04% trisodium citrate, 0.26 mM potassium carbonate, and 0.02% sodium azide. The average diameter of 5 nm of the Au nanoparticles corresponds to a mass of $\sim$ 760 kamu. A slight change in color of the reddish base suspension was observable during storage in the refrigerator, indicating a possible increase in the actual particle size due to clustering and/or coalescence.

The composition and the supply and atomization parameters of the Au colloidal spray solution are displayed in table 5.1, while all further operational parameters of the ESI source used during deposition are listed in table 5.2. A mean analyte current of $\sim$ 5 pA was electrospray deposited for 2 h 45 min, while the substrate was at room temperature.

Figure 5.5 shows tapping mode AFM images recorded under ambient conditions.

Electrospray Deposition of Colloidal Au			
voltages at ESI-head		voltages at ion optical system	
$V_{ent.}$:	-3.3 kV	$V_{lens\ 1\ of\ IOS}$:	-25 V
$V_{cap.}$:	-3.9 kV	$V_{lens\ 2\ of\ IOS}$:	-25 V
$V_{frag.}$:	$+150$ V	$V_{lens\ 3\ of\ IOS}$:	-25 V
voltages at ion guides		voltages at funnel lens system	
$V_{skim.}$:	$+25$ V	$V_{funnel\ lens\ 1}$:	-100 V
$V_{dc\ IG\ I}$:	$+15$ V	$V_{funnel\ lens\ 2}$:	-150 V
$V_{ac\ IG\ I}$:	190 V	$V_{funnel\ lens\ 3}$:	-200 V
$V_{aper.\ I}$:	$+11.2$ V		
$V_{dc\ IG\ II}$:	$+7.5$ V		
$V_{ac\ IG\ II}$:	380 V		
$V_{aper.\ II}$:	grounded		

Table 5.2: Operational parameters of the ESI deposition source used during spraying of the Au colloidal solution. A key to the abbreviations of the functional electrodes used above, and the names of the electrodes and their locations is provided by figures 4.4, 4.14, and 5.1.
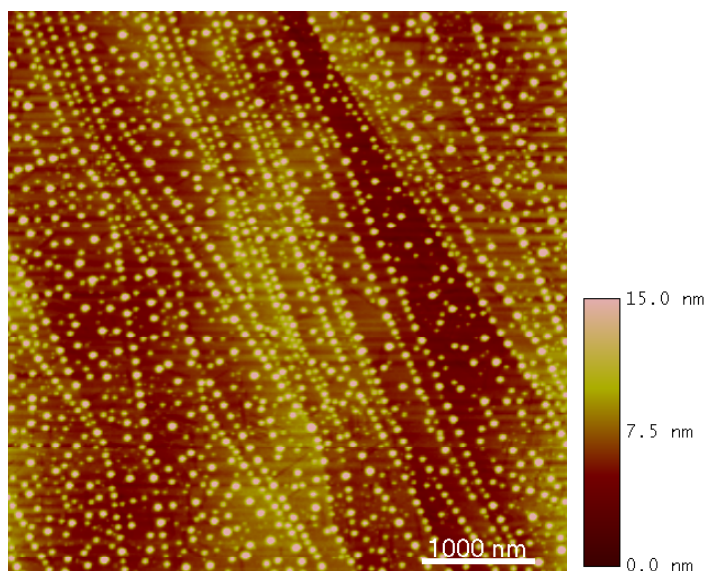

Figure 5.5: Electrospray deposited colloidal Au on HOPG. The nanoparticles show a preferential adsorption at step edges of the HOPG surface. Image size: 5 μm × 5 μm.

Only well separated single nanoparticles can be observed, without any signatures of an eventual co-deposited solvent. The preferential adsorption along the mainly monatomic step edges of the HOPG substrate results in the formation of quite regularly spaced chain-like arrangements composed of single nanoparticles (see figure 5.6). Additionally, Au nanoparticles are also adsorbed on top of HOPG terraces.
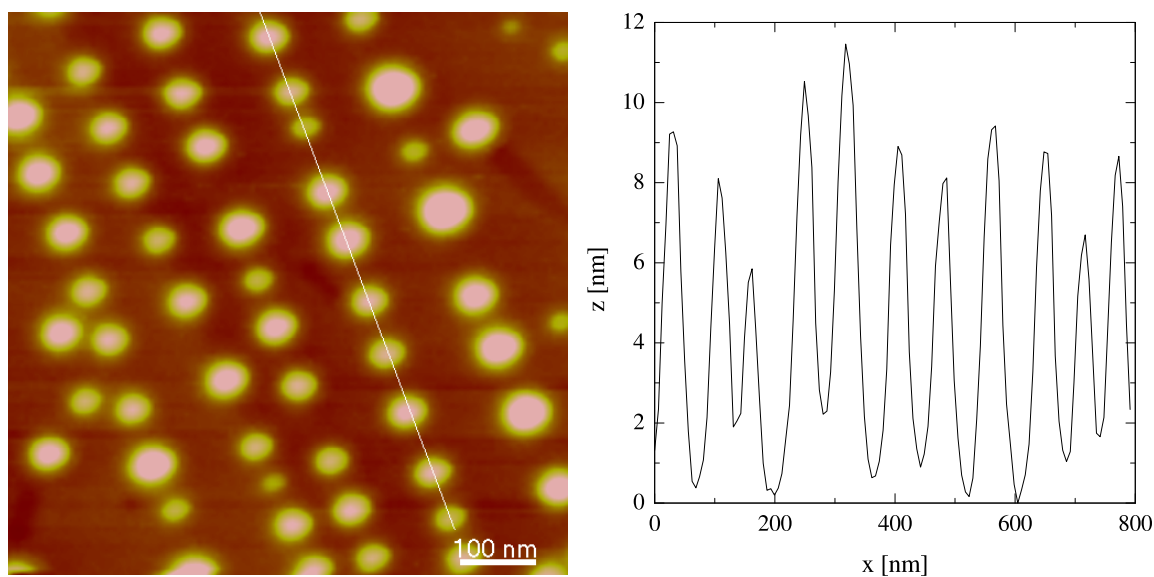

Figure 5.6: Au nanoparticles adsorbed at HOPG step edges. The lateral separation of the deposited colloidal Au is demonstrated by the cross-section along such a step edge, which is marked by the thin white line. Image size: 750 nm × 750 nm.

Compared to the specification of the colloidal base suspension (average diameter: 5 nm, nominal size range: $3.5 - 6.5$ nm), a significant difference in the measured average particle size and in its corresponding height distribution (average height: ~ 9 nm, height range: $4 - 16$ nm) can be observed. This might be partially explained by an overestimation of the particle size due to the convolution with the finite size of the AFM tip, and partially by an actual increase of the Au particle size, due to the before mentioned aging of the base suspension during storage.

On the other hand, we exclude that the measured broader size distribution is the result of a clustering or ripening process taking place directly at the surface. In fact, the complex composition of the colloidal spray solution supports the assumption of Au nanoparticles passivated by a crust of buffer substances that causes a short range repulsion between the particles. As a consequence we interpret the AFM data

in figures 5.5 and 5.6 as representing single passivated Au nanoparticles directly transferred from the colloidal suspension to the surface. Finally, we note that the passivation of the Au nanoparticles most probably causes a weak interaction with the HOPG substrate, allowing a high mobility of the particles and therefore the observed homogenous coverage of the surface. Nevertheless, the particle-substrate interaction cannot be without any effect on the arrangement of the Au nanoparticles, since otherwise one could not explain the preferential adsorption at the step edges.

5.4   Electrospray Deposition of Rhodamine 6G on Si(111)

Figure 5.7 shows a structural model of rhodamine 6G, a dye molecule with a molecular mass of 442 amu, that was used as a light test molecule. Rhodamine 6G was
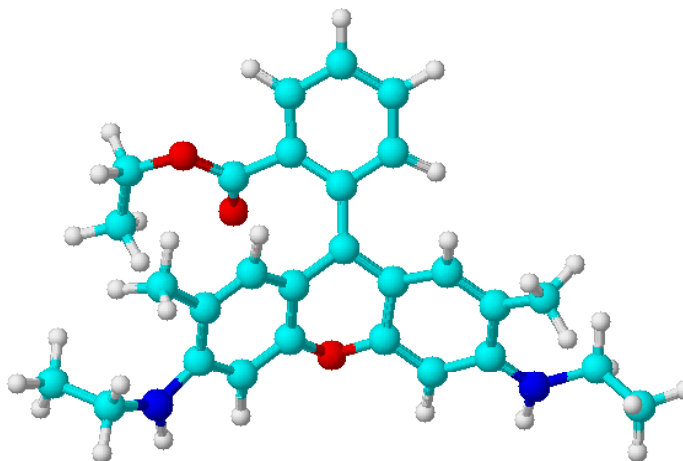

Figure 5.7: Structural model of the dye molecule rhodamine 6G ($C_{28}H_{30}N_2O_3 \cdot HCl$, molecular mass: $442 + 37$ amu). Color code: H = white, C = cyan, O = red, N = blue.

purchased from Aldrich (product number: 25,234-3, dye content: 99%), while the p-type Si(111) wafer was bought from Mateck (B doped, specific resistivity: 15 Ωcm). The native Si(111) substrate, covered by its natural oxide layer, was cleaned in several sonification steps in aceton and isopropanol before deposition. Table 5.3 displays the composition and the supply and atomization parameters of the utilized spray solution. A mean current of $\sim$ 30 pA was deposited for 3 h, while the Si(111) substrate

analyte:	Rhodamine 6G	
product number:	25,243-3 (Aldrich)	
spray solution:	5 ml	H_2O
	10 ml	CH_3OH
	100 μl	CH_3COOH
	1.5 mg	Rhodamine 6G
spray solution flow:	15 $\frac{\mu l}{min}$	at 0 bar
countergas flow:	8 $\frac{l}{min}$	at 150 °C

Table 5.3: Composition, supply, and atomization parameters of the rhodamine 6G solution used for ESI.

was at room temperature. All further operational parameters of the ESI source used during deposition were close to those displayed in table 5.2 on page 67.

Figure 5.8 shows tapping mode AFM images of the rhodamine 6G sample which were recorded under ambient conditions after the deposition. The left image was
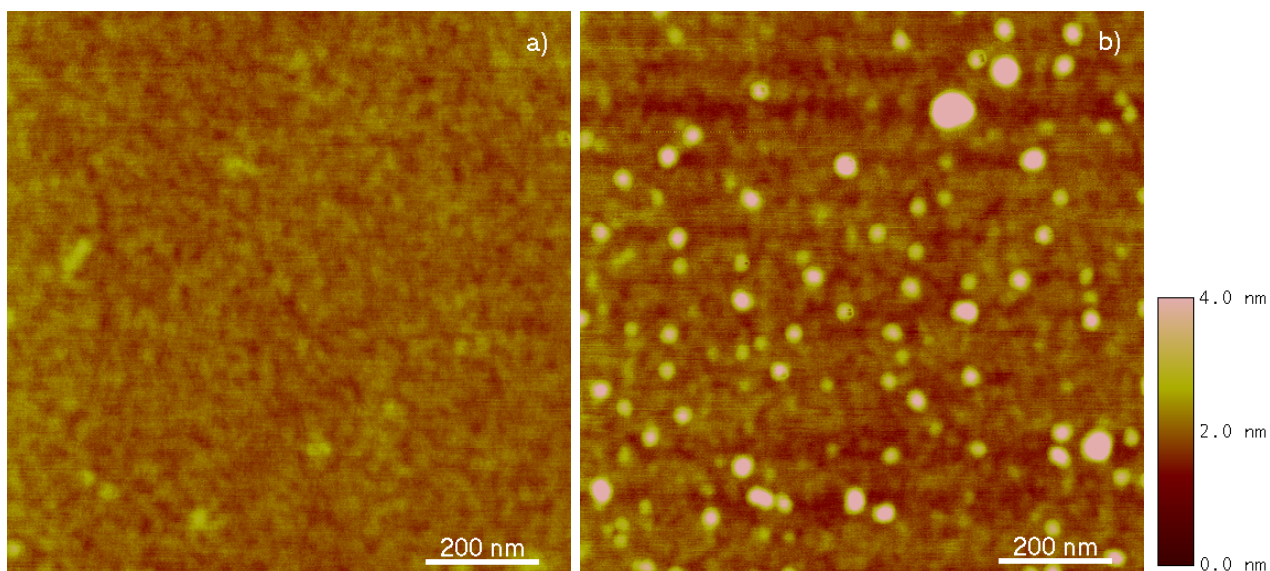

Figure 5.8: AFM images beside (a) and inside (b) the deposition area on the native Si(111) substrate. Dot-like structures can be observed only close to the center of the deposition spot. Image size: 1 μm × 1 μm, each.

recorded close to the border of the Si(111) substrate (size: 10 mm × 10 mm) far

away from the actual deposition spot (see section 5.2), showing only a few structures inherent to the substrate, and possibly remaining from the simple substrate cleaning procedure. The right image, in contrast, depicts a region close to the center of the deposition spot: Well dispersed dots can be observed, ranging from ~ 1 nm up to ~ 6 nm in height. Although these large dots clearly do not represent single rhodamine 6G molecules, the comparison with the blank measurement in image a) indicates that they are the result of the ESI deposition.

Without additional mass spectrometric information it is difficult to judge the origin of these structures. They could possibly originate from a clustering in solution or they could be due to a post-deposition coalescence on the Si(111) substrate. Moreover, it cannot be excluded that they are composed of a mixture of analyte and solvent molecules. Nevertheless, the observation of a deposition current during sample preparation and the presence of deposited structures prove the successful electrospray deposition of rhodamine 6G.

5.5 Deposition of Bovine Serum Albumin on HOPG

Bovine **S**erum **A**lbumin (**BSA**) is a single polypeptide chain protein, composed of 583 amino acid residues [40], and has a molecular weight of ~ 66.4 kamu. The transport of lipids, fatty acids, and non-water-soluble substances within the blood circulation is one of its manifold physiological tasks [40, 41].

Albumin molecules can be regarded as consisting of 3 spherical domains stabilized by disulfide cross-linkages [40, 41]. Unfortunately, no crystallographic structure of BSA is available. Figure 5.9 shows the tertiary structure of the closely related human serum albumin in the form of a ribbon diagram. When dissolved in water, BSA adapts an elongated ellipsoidal shape with a 116 Å long axis and a 27 Å short axis [43].

Two approaches were used to deposit the protein molecules on the substrate. Either directly, by dripping the solution onto the substrate, or via the route of electrospray deposition under vacuum conditions. A comparison between the two methods allows us to directly demonstrate the differences and the advantages of our novel
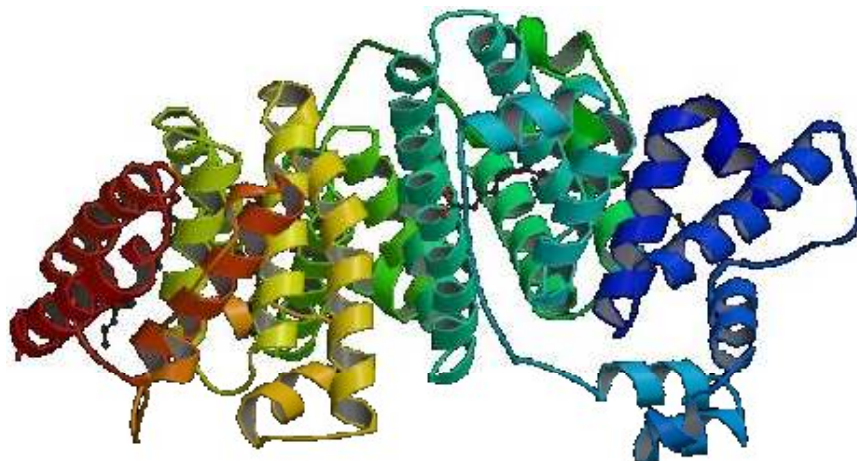
Figure 5.9: Ribbon diagram of human serum albumin, whose constituting amino acid sequence is about 80% homologous to that of BSA [42].

deposition technique.

5.5.1   Direct Deposition of Bovine Albumin on HOPG

Bovine albumin was purchased from Sigma (product number: A-1900) in the form of a lyophilized powder with a glassy white appearance. The solution consisted of 2 mg bovine albumin, 10 ml H_2O, 10 ml CH_3CH_2OH, and 100 μl glacial acetic acid, corresponding to an albumin concentration of 1.5×10^{-6} $\frac{mol}{l}$. The solution was dripped onto the HOPG substrate (size: 10 mm$\times$10 mm) immediately after cleavage. In order to avoid the fast retraction of drying fronts, it is better to evaporate the solvent slowly, which is achieved simply by covering the sample with a glass beaker. Afterwards, the samples were investigated by means of tapping mode AFM.

In the case of the direct deposition of the 'mother solution', various problems appeared in the tip-sample approach as well as during tip-scanning. These are probably due to the formation of large protein aggregates, densely covering the substrate surface. Only further diluting the 'mother solution' led to the formation of thin albumin films that could be successfully imaged.

Figures 5.10 a) and b) show AFM images obtained after dilution in 1 : 1 water/ethanol by factors of 10 and 100, respectively. Image a) shows branched albumin aggregates (height range: $3.5 - 4.5$ nm), visible after the first step in dilution. The
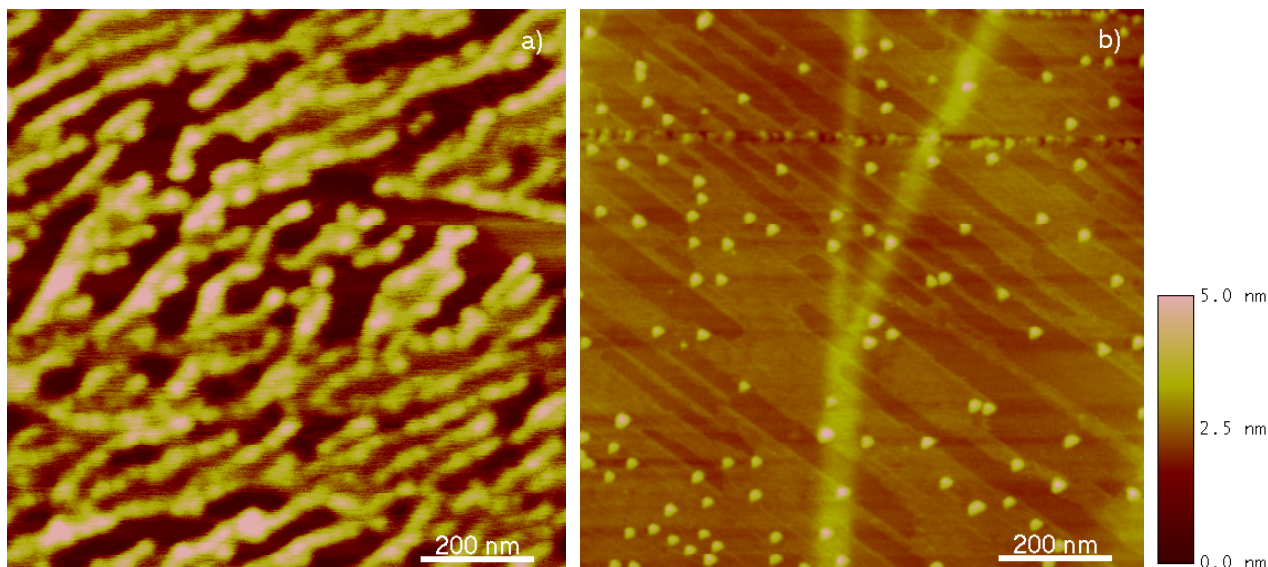
Figure 5.10: a) Branched protein aggregates and b) single albumin molecules on HOPG observed after dilution of the 'mother solution' in a 1 : 1 water/ethanol solution by a factor of 10 and 100, respectively. Image size: 1 μm $\times$ 1 μm, each.

preferred branching direction might be related to the movement of the local retraction front during solvent evaporation. In contrast, albumin deposition from the highly diluted solution resulted in the morphology depicted in figure 5.10b, in which separated, single bright dots, that can be attributed to single BSA molecules, are immersed in a wetting film. This film is characterized by a uniform height of $\sim$ 0.4 nm (compare with the monatomic step height of HOPG, $\sim$ 0.7 nm) and is most probably due to solvent remaining after evaporation. The dots have a uniform height of $\sim$ 1.9 nm and a triangular shape that compares well with the one reported for human albumin molecules[1] adsorbed on mica [44]. Their height on the contrary, is much larger to what has been measured in the case of human albumin ($\sim$ 0.5 nm, [44]), and lies nearly in the middle of the height range of $1 - 3$ nm of typical biomolecules. Since the heights measured by AFM depend on the tip-sample interaction, this difference could be caused by various forces used while imaging the intrinsically 'soft' molecules. This comparison shows that, besides experimental details of sample preparation, the

---

[1] The constituting amino acid sequences of bovine and human serum albumin are about 80% homologous, their molecular weights differ by less than 1%, and many other properties, such as their isoelectric points, are identical within experimental uncertainty [42].

proper adjustment of the tapping mode AFM is crucial for the imaging quality of sensitive biological molecules [45].

5.5.2 Electrospray Deposition of Bovine Albumin on HOPG

Composition of the Spray Solution

Figure 5.11 compares two deposition protocols (see section 5.2) of bovine albumin spray solutions, with (●) and without (▲) glacial acetic acid. In both cases, the
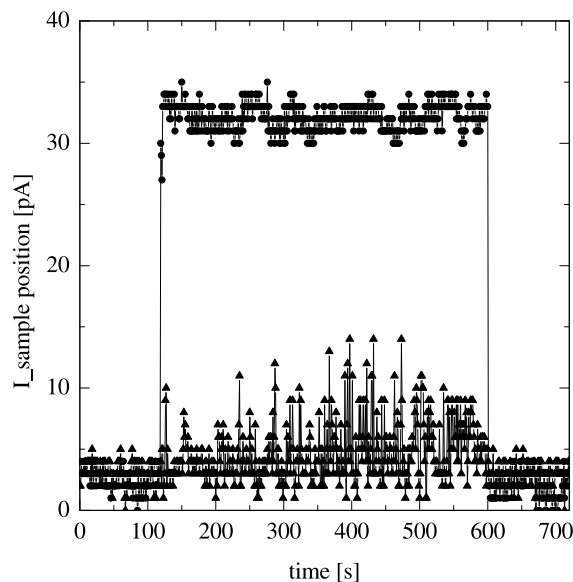

Figure 5.11: Examples of bovine albumin deposition protocols: Spray solutions with (●) and without (▲) acetic acid are shown.

deposition was turned on at t $\simeq$ 2 min and again off at t $\simeq$ 10 min, but only solution containing glacial acetic acid showed a significant deposition current of $\sim$ 30 pA. Without glacial acetic acid, only statistical fluctuations, mainly due to the nebulizer mode operation of the electrospray source, are observable. This behavior is a consequence of protein charging that takes place in solution, and can also be found for other analytes.

Electrospray Deposition of Bovine Albumin on HOPG

During sample preparation, an albumin current of $\sim$ 25 pA was deposited for 1 h 15 min onto a freshly stripped HOPG substrate at room temperature. Table 5.4

analyte:	Bovine Serum Albumin
product number:	A-1900 (Sigma)
spray solution:	8 ml H_2O
	12 ml CH_3OH
	200 μl CH_3COOH
	2 mg Bovine Albumin
spray solution flow:	6 $\frac{\mu l}{min}$ at 1 bar
countergas flow:	8 $\frac{l}{min}$ at 150 °C

Table 5.4: Composition, supply, and atomization parameters of the bovine albumin solution used for ESI.

lists the corresponding composition, supply, and atomization parameters of the spray solution. All further operational parameters of the ESI source used during deposition were identical to those displayed in table 5.2 on page 67.

Tapping mode AFM images of bovine albumin on HOPG are shown in figure 5.12. The albumin molecules adsorb preferentially at step edges, but in addition, the for-
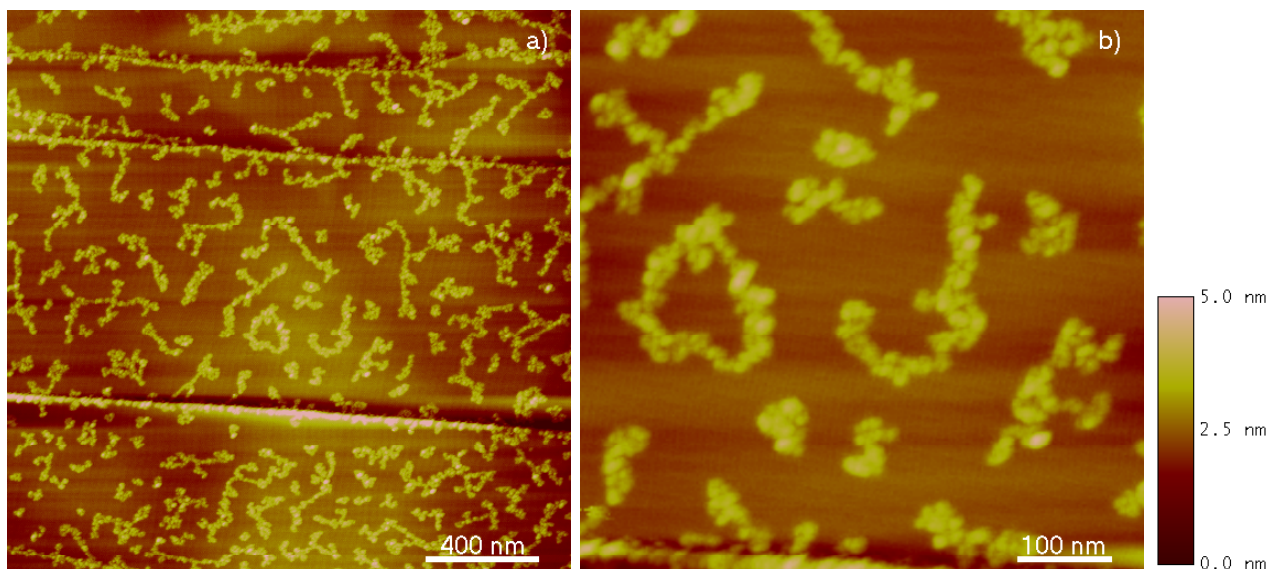

Figure 5.12: Ramified growth of bovine albumin on HOPG. An intrinsic substructure of the deposited albumin 'units' can be observed. Image sizes: a) 2 μm × 2 μm, b) 600 nm × 600 nm.

mation of ramified structures can be observed on flat terraces. High resolution images such as figure 5.12b reveal that the structure of these dendritic islands appears to be highly non-uniform. This is quite different from the well understood dentritic growth of e.g. epitaxially deposited Ag on Pt(111) [46, 47], where all elementary units (Ag atoms) constituting the aggregates are identical. Nevertheless, we believe that also in this case the ramified islands are composed of single BSA molecules, and that the inner morphology of the island is the result of the non-spherical structure of the molecules. Apparently, a fragmentation and/or denaturation of the protein molecules occurred either during deposition onto the substrate or during the course of ESI.

Even without direct mass spectrometric information, the comparison with values reported in literature[2] tells us that the fragmentor-skimmer voltage difference ($<$ 150 V) used should be small enough to avoid the collision induced fragmentation of albumin ions during supersonic expansion. Moreover, the maximal kinetic energy per bovine albumin ion can be estimated[3] to be at most 1.5 keV.

As a consequence, the mean kinetic energy per atom is lower than 1 eV, which is known to be the rule of thumb upper limit for the nondestructive deposition of composite clusters [49]. Although these arguments reasonably rule out the possibility of molecule fragmentation during deposition, a conclusive answer to this question can only be given by comparing the ESI-TOF mass spectra recorded during sample preparation with mass spectra gained from the previously deposited and reelectrosprayed analyte material.

Albumin is known to undergo a change in its tertiary structure, depending on the pH value of its liquid environment. Figure 5.13 shows proposed isomeric configurations of the pH dependent transitions of human albumin [40, 50], starting with the normal form (N form), via the fast form (F form), toward the extended form (E form) . The values of the transition pH between forms N and F and forms F and E

---

[2]Smith et al. [7] obtained fragmented bovine albumin ESI-TOF mass spectra with a nozzle-skimmer voltage difference of 335 V, while our accelerating fragmentor-skimmer voltage is at most 150 V.

[3]Retarding grid measurements yield a kinetic energy per charge of 15 V as upper limit (compare section 4.3.4), while bovine albumin charge states up to 80 elementary charges (assumed upper bound: 100 charges) are known in literature [48].
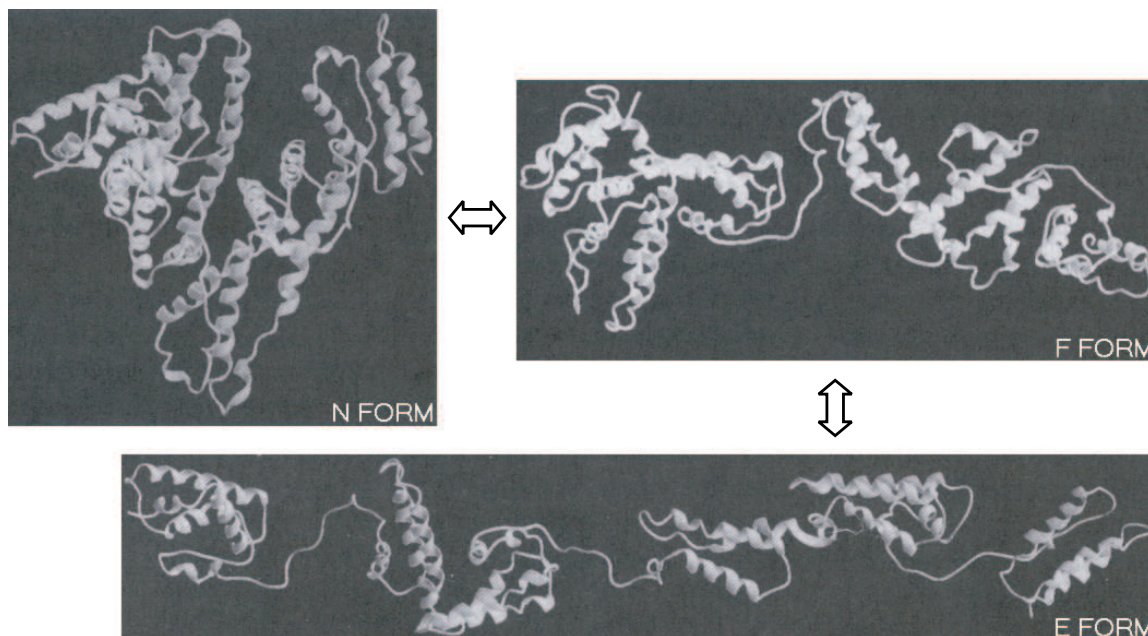
Figure 5.13: Transitions between isomeric configurations (N, F and E forms) of human albumin, depending on the pH of the solution. The pH values for the transition from N to F and from F to E are 4.3 and 2.7, respectively. Images reproduced from [40].

is 4.3 and 2.7, respectively [40, 51]. Assuming that similar transformations also take place with bovine albumin, the measured pH value of $3.5 - 4.0$ of our spray solution would imply that the F form should be predominant. This could therefore be the true origin of the observed intramolecular substructures in figure 5.12b.

Conversely, the pH value of the albumin solution ($5.5 \leq \text{pH} \leq 6.0$) used for the direct deposition on HOPG (see figure 5.10b) corresponds to the compact N form [40, 51]. This means that the triangular shape of human albumin on mica (deposited from solution at pH 7.5) observed by Quist et al. [44], and the triangular shaped bovine albumin molecules in figure 5.10b are in accordance with the reported heart-shaped structure of the N form in figure 5.13.

Incidentally, we note that one consequence of this pH dependence is the corresponding change in the distribution of the protein's mass-to-charge state in ESI-TOF mass spectra [48]. This is most probably due to the accompanying change of the protein molecule's surface-to-volume ratio, and will have an effect on the transmission through the whole ESI deposition source which depends on the mass-to-charge ratio

of the analyte ions.

A last important point concerns the interaction of bovine albumin with the substrate, which might induce a denaturation after deposition. Recently T. C. Ta and J. T. McDermott [52] reported about a contact mode AFM investigation of BSA adsorbed to HOPG. In order to explain their observations on bovine albumin aggregates, they proposed a dissociation of intramolecular disulfide bonds and a subsequent exposure of hydrophobic albumin regions to the outer shell of the aggregate, formed by intermolecular cross-linking. Although those measurements cannot be directly compared with ours since they were performed in the liquid environment, we cannot exclude that similar substrate induced bond dissociations and intermolecular linking also take place after the ESI deposition of BSA, and contribute to the morphology of the molecular structures in figure 5.12.

In conclusion, we can summarize the interpretation of the ESI deposition experiments of BSA on HOPG as follows: No fragmentation of bovine albumin occurs during ESI, supersonic expansion, and ion beam formation. The deposition itself is a very soft landing of dry, ionized protein molecules, without any decomposition. The molecules are already partly denatured in solution due to its low pH value. After deposition, the albumin molecules diffuse across the HOPG surface and stick together when they meet each other. The formation of intermolecular links, possibly accompanied by the dissociation of intramolecular disulfide bonds, is quite strong, and inhibits any restructuring of the formed molecular islands, thus producing a dentritic shape.

5.6   Deposition of Horse Spleen Ferritin

Ferritin is an iron storage protein which plays a key role in the iron metabolism, responsible for iron detoxification and iron reserve [53]. The spherical protein shell of a ferritin molecule without an 'iron' core, which is equal to an apoferritin molecule, is composed of 24 subunits (24 single polypeptide chains), forming an internal cavity of ~ 6 nm in diameter [54]. The molecular mass of the whole protein shell of horse spleen ferritin is ~ 450 kamu [54]. Figure 5.14 shows the corresponding ribbon diagram of the ferritin molecule, together with a schematic drawing of its structural composition.

Based on the possibility of loading this protein shell with different metals, new 'Bio
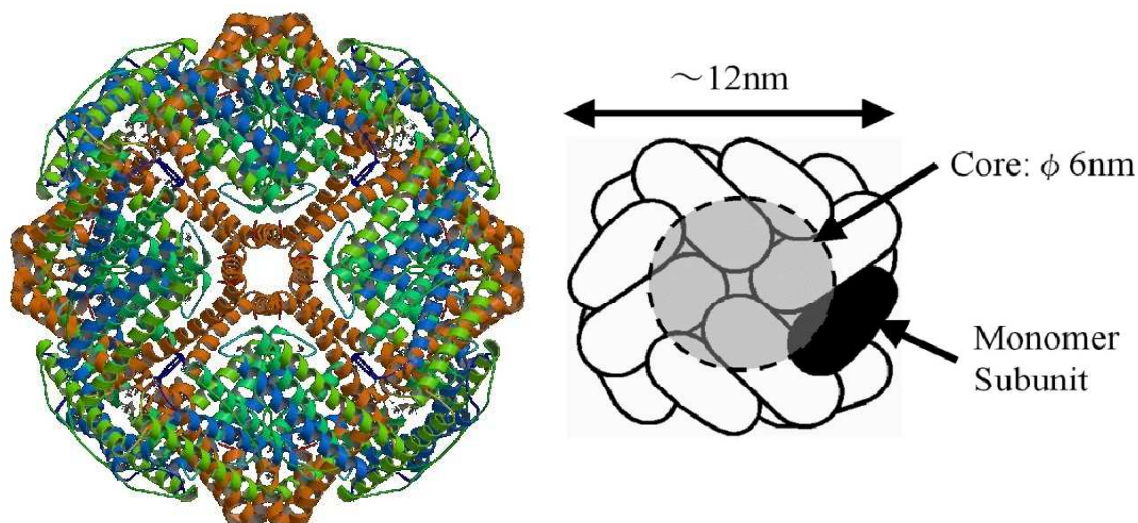

Figure 5.14: Ribbon diagram and structural schematic of horse spleen ferritin. Schematic drawing reproduced from [54].

Nano-Processes' have been proposed, which use protein molecules as scaffolds for the production of inorganic, functional nanostructures [54, 55].

As in the case of bovine albumin, two different approaches were used to deposit the protein onto the substrates. Either directly, by the dripping method under ambient conditions, or by using the ESI deposition source, where the sample preparation is performed under high vacuum conditions. HOPG, and **t**ransmission **e**lectron **m**icroscopy grids (**TEM**-grids) coated with a thin organic film, were used as substrates. All combinations of deposition variant and substrate are presented in the following.

5.6.1 Direct Deposition of Horse Ferritin on HOPG

Iron saturated horse spleen ferritin was purchased from Fluka (product number: 96701) in the form of a sterile filtered solution in 150 mM NaCl. The deposited solution consisted of 75 μl ferritin base solution, 6 ml H_2O, 10 ml CH_3OH, and 150 μl glacial acetic acid. The sample preparation technique was similar to the one used with bovine albumin (see page 72). Figure 5.15 shows tapping mode AFM images of horse ferritin on HOPG. Sample a) was rinsed with H_2O after solvent evapora-
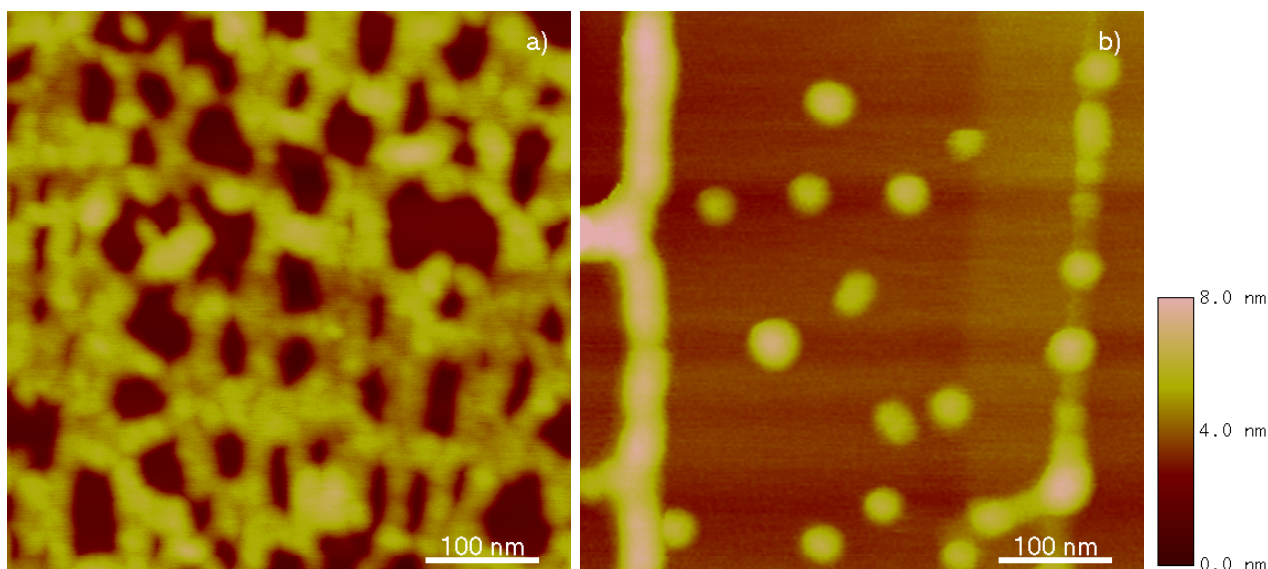
Figure 5.15: Direct deposition of horse ferritin on HOPG. Sample a) after rinsing with H$_2$O, Sample b) diluted solution, without rinsing. Image size: 500 nm $\times$ 500 nm, each.

tion, unlike the direct deposition of bovine albumin. A net shaped protein pattern, $3 - 5$ nm in height, can be observed. Similar to the observed wetting film in the case of bovine albumin (see figure 5.10b), rinsing of the sample might lead to the presence of a solvent film wetting the substrate. Although sample a) was rinsed, it cannot be excluded that NaCl precipitates that stem from the ferritin base solution were integrated into the protein pattern.

Figure 5.15b was obtained after diluting the 'mother solution' by a factor of 100. The corresponding sample b) was imaged as prepared, without further rinsing. Nearly identical to the highly diluted bovine albumin on HOPG, dot-like structures can be observed on top of HOPG terraces (height range: $1.5 - 4.5$ nm). Furthermore, a preferential attachment to step edges of the substrate is visible. While the ferritin molecules on the HOPG terraces are well resolved, this is not true for those adsorbed to the step edges, which is possibly due to NaCl being accumulated and transported by the retracting solvent front. The differences in size and shape of the dot-like structures might be due to the presence of NaCl, either imaged as an individual dot or attached to the ferritin molecules during the final stages of solvent evaporation.

analyte:	Horse Spleen Ferritin	
product number:	96701 (Fluka)	
spray solution:	6 ml	H_2O
	10 ml	CH_3OH
	150 μl	CH_3COOH
	75 μl	Horse Ferritin solution
spray solution flow:	8 $\frac{\mu l}{min}$	at 0 bar
countergas flow:	8 $\frac{l}{min}$	at 150 °C

Table 5.5: Composition, supply, and atomization parameters of the horse ferritin solution used for ESI.

5.6.2   Electrospray Deposition of Horse Ferritin on HOPG

During sample preparation, a current of ~ 10 pA was deposited for 7 h, while the HOPG substrate was at room temperature. The corresponding composition, supply, and atomization parameters of the spray solution are displayed in table 5.5. The operational parameters of the ESI source used during deposition are close to those listed in table 5.2 on page 67.

Figure 5.16 shows tapping mode AFM images of the electrosprayed ferritin on HOPG. The ferritin molecules align preferentially along the step edges, which indicates that these are preferential adsorption sites, such as in the case of BSA (see figure 5.12). Image b) shows the homogeneous distribution of ferritin molecules on HOPG terraces in more detail. Unlike to bovine albumin, no larger island-like ferritin aggregates can be found, although the mean molecule-to-molecule distance is only 3 times larger than the imaged lateral molecule dimension. Both the homogenous coverage and the absence of islands point to a short range repulsive intermolecular interaction.

The height distribution of the ferritin molecules in image b) ranges from $2-7$ nm, and is centered around ~ 4 nm, which matches well with the corresponding height distribution in the case of the direct ferritin deposition. Although tip-convolution effects do not allow a direct comparison of the lateral dot sizes in figures 5.15b and 5.16b, the morphology of the single dots seems to be quite similar. Moreover, the complex
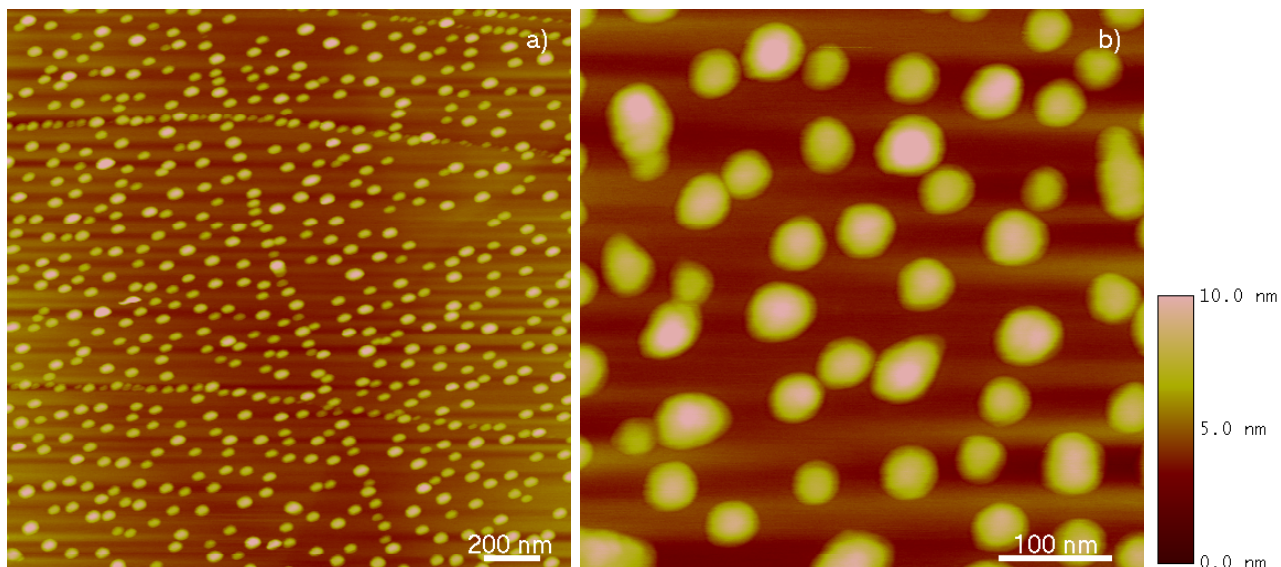
Figure 5.16: Electrospray deposition of horse ferritin on HOPG. Image size: a) 2 μm $\times$ 2 μm, b) 500 nm $\times$ 500 nm.

composition of the analyte solution used in both experiments, the direct dripping of solution and the ESI deposition of the analyte onto the substrate, support the proposition of ferritin molecules that are e.g. partially covered by a crust of preservative substances stemming from the base solution. This might explain the differences between an ideal deposition of monodisperse and pure ferritin molecules, and the ferritin structures observed in figure 5.16 under experimental conditions.

5.6.3   Electrospray Deposition of Ferritin onto TEM-Grids

As in the previous cases on HOPG, the simple drip-and-dry preparation method is compared with the ESI deposition under vacuum conditions. TEM-grids[4], coated by a thin organic Formvar film, are used as substrates for transmission electron microscopy measurements. The TEM-imaging contrast between the organic support film and the iron saturated ferritin molecule itself, results from the large scattering cross-section of the Fe atoms located inside the protein shell, compared to that of the organic environment.

---

[4]The TEM-grids used have 400 meshes per inch and are made of Cu. The diameter and thickness of the TEM-grids are $\sim$ 3 mm and 0.05 mm, respectively.

Figure 5.17 compares directly deposited (image a) with electrosprayed[5] (image b) ferritin TEM-samples[6]. Single molecules, as well as dimers, oligomers, and aggregates of horse spleen ferritin molecules can be observed in image a), while only randomly placed single molecules are visible in image b). This is a clear indication that the
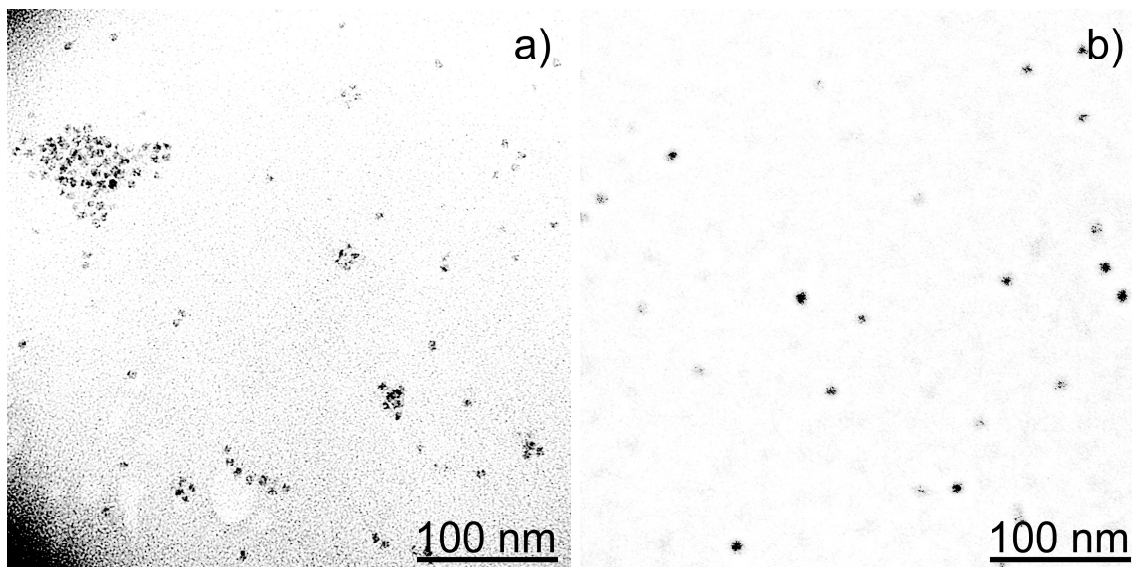

Figure 5.17: Comparison of direct deposited (a) and electrospray deposited (b) TEM-samples of horse spleen ferritin. Image size: 400 nm × 400 nm, each.

ionized ferritin molecules are deposited as single entities, and do not form aggregates due to the hindered diffusion on the organic film. A diameter of ~ 6 nm is obtained for the ferritin cavity, independent of the preparation method[7], which agrees well with diameter values of $5.0 - 5.5$ nm reported by [54].

Finally, it should be emphasized that already at the present stage the ESI deposition source could be a very useful tool. This novel deposition approach circumvents the deposition of larger analyte clusters stemming from in-solution clustering, in contrast to the standard deposition out of the liquid phase. Furthermore, it is possible to deposit multiply charged, dry analyte ions that generally might be partially denatured

---

[5]The composition, supply, and atomization parameters are nearly identical to those of the ESI deposition on HOPG. The same holds for the operational parameters of the ESI source.

[6]The TEM measurements were done on a Philips CM 200, owned by the Max-Planck-Institute for Metal Research, Stuttgart.

[7]A contrast enhancement during image processing leads to an apparent size difference of the ferritin cores in images a) and b).

during the course of ESI (compare section 5.5.2). Moreover, the full controllability of the ESI deposition process enables the precise adjustment of the sample coverage at the deposition spot. The source-intrinsic possibility of a multiple sequential deposition of different electrosprayable analyte substances allows the controlled 'growth' of adsorbate-substrate systems of increasing morphological complexity. After the setup of the UHV-ESI deposition source is completed, the above mentioned advantages will permit the in-situ scanning probe investigation of interaction mechanisms between the adsorbate and the underlying substrate, as well as among the adsorbate molecules themselves.

Chapter 6

UHV–STM study of di-L-Phenylalanine deposited on Cu(110)

During each deposition experiment presented in chapter 5, all analyte ions had to pass the final opening of the funnel lens system before being deposited on the substrate (see figure 5.2). The passing of this pinhole (ID $\sim$ 2 mm) proves that the ion beam is sufficiently well defined, and that it is possible to pass the ions without significant intensity losses through very narrow apertures, such as those that are typically needed in between neighboring vacuum stages of a differential pumping system (typical size: ID $\sim$ 2 mm). Hence, no fundamental problem remains on the way when transferring the ion beam into UHV environment. Therefore, once the complete ESI deposition apparatus is fully operational, it will allow the UHV deposition of sensitive thermolabile molecules of biological interest onto atomically defined and chemically clean substrates.

Such an ESI-based deposition apparatus has a much broader range of application compared to conventional OMBE-based deposition techniques. These are limited to smaller molecules like amino acids [56, 57] and small oligopeptides [58, 59], due to the thermal nature of the underlying sublimation process. Large molecules tend to dissociate before subliming, due to their numerous degrees of freedom and their increased thermolability. In contrast, the technological concept of ESI is able to

circumvent the thermal limitation and to vaporize sensitive analytes of biological interest, such as carbohydrates and lipids [9], amino acids [60, 61], peptides and proteins [9], into the ionized gas phase. Even the ESI-MS of viruses up to a molecular mass of 40.5×10^6 Da has been reported by Fuerstenau et al. [62].

Therefore, the coupling of ESI with an UHV deposition machine will constitute a completely new deposition apparatus, offering new challenges in the maturing field of biological surface science [1]. We will be mainly interested in the in-situ structural investigations of various (biological) adsorbate-substrate systems, performed by means of STM and AFM. In-vacuo scanning probe microscopy in combination with further UHV compatible surface science techniques will allow precise answers to fundamental questions such as how biomolecules bind to atomically defined surfaces and how they interact mutually.

A short description of the UHV system that will constitute the deposition and analysis chamber of the complete ESI deposition apparatus was already presented in section 2.1. Since this system is already fully operative, it is presently used for conventional OMBE deposition studies of small molecules on metal surfaces. In the following we will give an example of such a more traditional type of deposition experiment, applied to a small biological molecule, which can still be sublimated. The interactions among single adsorbate molecules themselves and between the biomolecules and the underlying substrate, as well as the influence of the adsorbate's chirality on the formation of supramolecular structures, will be investigated. This section is intended to be a taste of what will be possible once the ESI deposition source is fully operational, and a soft deposition of large biomolecules under UHV conditions is feasible.

6.1 Vapor Deposition of di-L-Phenylalanine on Cu(110)

While the UHV-ESI deposition source is still incomplete, the two-chamber system just described is fully operational, and can be used for studying the deposition of small organic molecules which are still sublimable by conventional evaporation techniques. In the remaining part of this chapter we will present an example of such a

study for the case of a dipeptide, which can be considered to be the first step in the complexity ladder that characterizes biological molecules. Once the assembly of the ESI deposition source is completed the same type of studies will be done with larger molecules.

We decided on di-L-Phenylalanine (di-L-Phe) which is close to the upper range of molecular mass accessible by the thermal sublimation technique. In principle, it is necessary to regard each molecule as a case on its own due to the dependence of the 'sublimability' on various factors such as the type and the strength of the inter- and intramolecular binding forces. In any case, when comparing di-L-Phe with reported OMBE-based deposition experiments of amino acids and small oligopeptides [58, 59, 63], it can be regarded as lying close to the 'limit' where OMBE starts to be impossible.

Figure 6.1 shows the structural model of di-L-Phe, a dipeptide formed by the condensation of two L-Phe molecules, having a central peptide bond. Phenylalanine
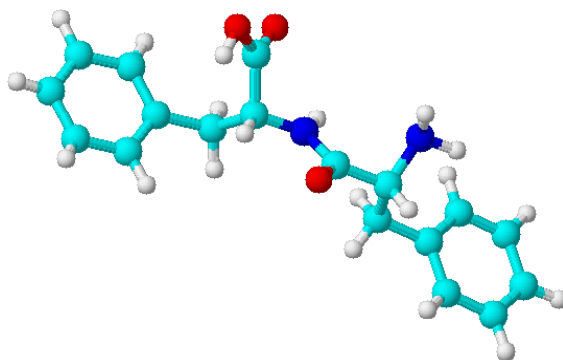

Figure 6.1: Structural model of di-L-Phenylalanine, a dipeptide with a molecular mass of 312 amu. Color code: H = white, C = cyan, O = red, N = blue.

itself is one of the 20 proteinogenic amino acids occurring in nature, and plays an important role in a multitude of biological processes [64]. Each single Phenylalanine molecule consists of one amino group, one carboxylic group, and one Phenyl-residue bond via a further C atom (benzyl group) to the central C_α atom. Depending on the spatial arrangement of groups bonded to the cental C_α, two different chiral forms (D and L) can be distinguished, whereas only the L-form is naturally occurring. Therefore, intrinsically two chiral centers are present per single di-L-Phe molecule.

We chose the Cu(110) single crystal surface as substrate, as it is known to interact strongly with amino and carboxylic groups of organic molecules [63]. Figure 6.2 depicts a model of the Cu(110) single crystal surface, showing the rectangular surface unit cell spanned by two non-equivalent crystallographic directions. The Cu(110) surface is characterized by an alternating sequence of atomic rows and troughs oriented in the $[1\bar{1}0]$ direction. The non-equivalence of the two high-symmetry directions of
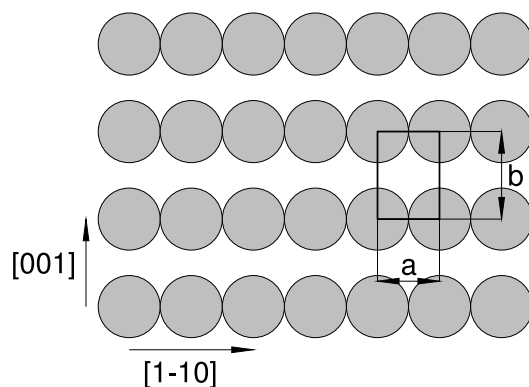

Figure 6.2: Structural model of the Cu(110) surface. The rectangle marks the surface unit cell of a = 2.56 Å and b = 3.61 Å. The arrows indicate the main crystallographic directions.

the Cu(110) surface results in a stronger modulation of the adhesion potential in [001] direction compared to the $[1\bar{1}0]$ direction. Due to this intrinsic one-dimensionality (1D) the Cu(110) surface can be used as a one-dimensional nanotemplate, offering an interaction potential that is strong enough to transfer the 1D nature of the substrate to the adsorbed structures [65].

We have prepared di-L-Phe samples in the submonolayer coverage regime, in order to study the interactions among single di-L-Phe molecules and between the molecule and the underlying nanotemplate. This analysis was done be means of STM measurements from which we inferred the formation of supramolecular structures as well as the adsorption geometry of single di-L-Phe molecules.

The Cu(110) crystal was cleaned by Ar^+ bombardment at 0.9 kV for 15 min, followed by annealing to $800 - 850$ K. Before being inserted in the UHV evaporator, the di-L-Phe molecules had been put into a desiccator for ~ 24 h, in order to remove the water and to facilitate the degassing under UHV. Afterwards, they were filled into a ceramic crucible of a Knudsen-cell-type evaporator, and degassed for several

hours in UHV for further purification. During evaporation the Knudsen cell was heated to 425 K, while the deposition time of $2 - 10$ min was controlled by means of a mechanical shutter. The background pressure always stayed below $3 \cdot 10^{-10}$ mbar during di-L-Phe deposition.

The deposition of di-L-Phenylalanine was done while holding the Cu(110) crystal at room temperature. In the first class of experiments this step concluded the sample preparation, while in a second one, the samples where further annealed at $370 - 380$ K for 1 min. After preparation, the sample was transferred under UHV to the AFM/STM analysis chamber, where room temperature STM investigations were performed.

Figure 6.3 shows STM images of the Cu(110) surface with a submonolayer coverage of di-L-Phe. The formation of extended di-L-Phe chains is observable, showing a high degree of coherence. It is important to note that the chains are not directed along the two high symmetry directions of the substrate[1], which are indicated in the figure. Instead, only one chain direction exists which is tilted by an angle of $55° \pm 2°$ counterclockwise from of the $[1\bar{1}0]$ high symmetry direction. On the contrary, based on simple symmetry arguments, one would expect that chains would form also along the mirror symmetric chain direction with respect to the $(1\bar{1}0)$ plane. From the fact that only one direction of the chains is observed, one can already conclude that the chirality of the di-L-Phe molecule plays a fundamental role in the molecule-substrate and/or the molecule-molecule interactions.

A closer look into the molecular chains (figure 6.3b) reveals an intrinsic substructure. This can be ascribed to the two Phenyl-rings of the di-L-Phe molecule, explaining the observed pattern as a single molecular row structure, in which each molecule appears as a double bump. The individual di-L-Phe molecules are tilted by $53° \pm 2°$ in counterclockwise direction with respect to the orientation of the dipeptide chain (therefore $108° \pm 2°$ with respect to $[1\bar{1}0]$). This can be seen in image b) of figure 6.3 and even better in figure 6.4. The di-L-Phe chains are thus formed by the periodic alignment of individual molecules next to each other. The simple structure

---

[1]The orientation of the high symmetry directions of the Cu(110) crystal has been determined independently on images showing atomic resolution.
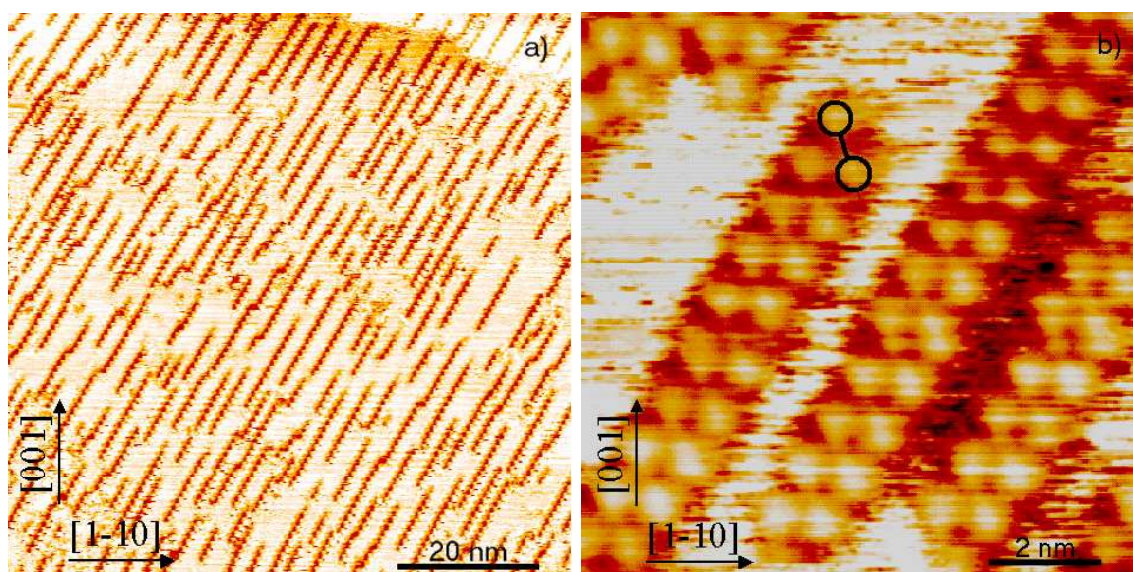
Figure 6.3: Di-L-Phenylalanine adsorbed to Cu(110) as observed by STM. a) Unidirectional single molecular di-L-Phe chains, aligned close to the $[1\bar{1}2]$ direction are visible. b) Higher magnification image of the same sample. A single di-L-Phe molecule is schematically indicated within a chain. Typical bias voltage and current values are -1.2 V and 1.1 nA. The coverage in these images is $\sim 30\%$. We note that the apparent lower height of the molecular chains with respect to the the bare substrate is caused by the STM tip picking up an adsorbate (probably Cu adatoms) between the chains. The right part of image b) shows an instance in which this does not happen between two closely spaced chains: the substrate in between them appears lower than the molecules. This effect depends on the tunneling conditions and has been reported for different systems, see e.g. reference [66]. Image size: a) 80 nm $\times$ 80 nm, b) 10 nm $\times$ 10 nm.

and the regularity of the chain, as well as the STM images in which the bare substrate was imaged with atomic resolution together with the chains, allow the conclusion that the molecules occupy equivalent crystal sites. As a consequence, the chain direction corresponds to the $[1\bar{1}2]$ direction of the Cu(110) substrate. It is interesting to note that in the case of (R, R)-tartaric acid adsorbed to Cu(110) [67], chiral organic films have been proposed as enantioselective substrates for heterogeneous catalysis.

Based on highly resolved STM images such as that in image a) of figure 6.4, we have measured the sizes and distances between individual di-L-Phe molecules in order to construct a model of the corresponding adsorption geometry (see figure 6.4b). Due to the many degrees of freedom for the internal configuration of the molecule and also the exact adsorption sites on the surface, several further assumptions have to be made. As already said, we attribute the observed double bump structures to the Phenyl-residues, and we therefore assume that they are facing the vacuum, whereas the central part of the molecule is attached to the surface. This 'hypothesis' is supported by the STM data, but for a precise determination of the orientation of the Phenyl-rings, further structural measurements (such as **n**ear **e**dge **x**-ray **a**dsorption **f**ine **s**tructure, **NEXAFS**, or **x**-ray **p**hotoelectron **d**iffraction, **XPD**) are needed. Moreover, the assumption that the central part of the molecule is in direct contact with the substrate fits well with the strong reactivity of its carboxylic and amino groups with Cu [63]. In addition, several chemical arguments are incorporated into the model. The actual binding is in fact supposed to be mediated by both the O atoms of the carboxylic group and by the N atom of the amino group. The carboxylic group is typically assumed to bind in its anionic form (that means having lost the hydrogen atom, the so called deprotonated form) with its two O atoms close to on-top sites of the substrate surface. Such a local bonding geometry has already been found for several amino acids and small peptides adsorbed on Cu(110) [58, 63]. The amino group typically binds with the plane, formed by its three atoms, nearly parallel to the substrate surface [58, 59]. Finally, the central peptide part is assumed to stay in a rigid planar form parallel to the surface [58, 59]. Using all these assumptions, a model of the di-L-Phe adsorption is obtained, which is shown in image b) of figure 6.4. The model is coherent with STM observations, so that all measured characteristic features

such as angles, distances, and orientations are exactly reproduced. Within this model, the formation of chiral supramolecular structures can be clearly attributed to a chiral adsorption of the single molecules. In fact, if the interaction with the substrate really does take place at the chiral part of the molecule, the actual observed molecular orientation ($\sim 108°$ with respect to $[1\bar{1}0]$) and its mirror symmetric one ($\sim -108°$ with respect to $[1\bar{1}0]$) are no longer equivalent.
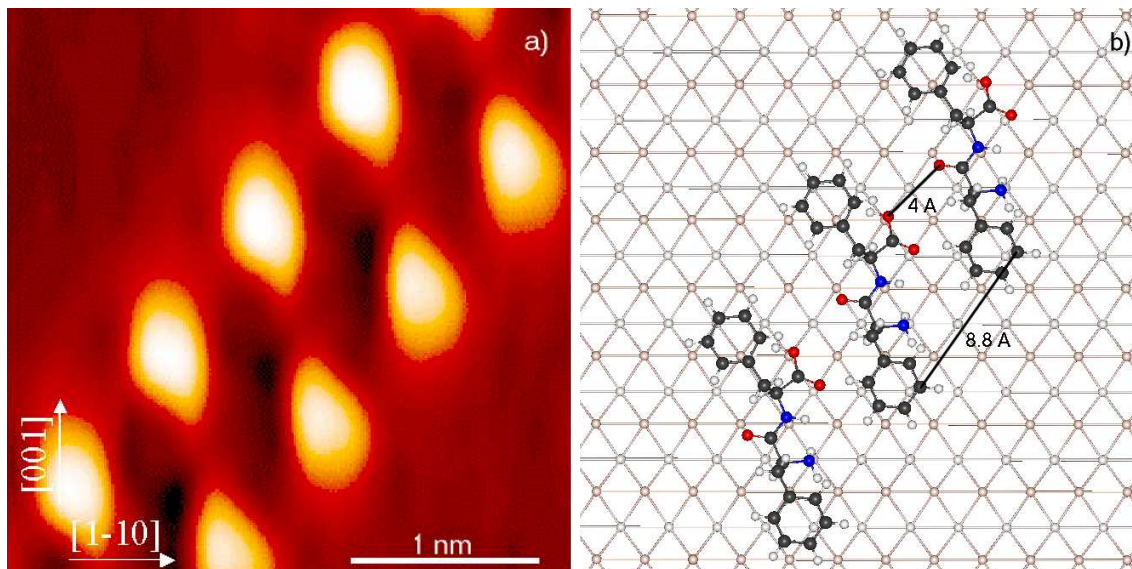

Figure 6.4: a) Highly resolved STM image (size: 3 nm $\times$ 3 nm) of a di-L-Phe molecular chain. The contrast has been enhanced in order to highlight the two Phenyl-rings that form each molecule. b) Adsorption model of di-L-Phenylalanine on Cu(110).

I. Stensgaard [58] recently performed similar STM experiments on the same single crystal substrate, Cu(110), having deposited di-L-Alanine, whose molecular structure can be obtained from that of di-L-Phe by replacing its Phenyl-rings with single H atoms. Interestingly, a different adsorption geometry was deduced from the STM data, indicating that the bonding to the substrate is not only determined by the central peptide region, but also by the $\cdot$ CH$_3$ residue.

In our case the Phenyl-residues seem to play a minor role in the interaction with the substrate, although it is impossible to completely exclude some remaining influence of the residue type on the choice of the adsorption site. Nevertheless, if our model is correct, a very similar behavior can be expected for conceptional similar dipeptides such as e.g. di-L-Tyrosine.

One open point within the model concerns the origin of the formation of the di-L-Phe chains. In fact, from molecular resolved STM images we get the distances that are shown in the model (see figure 6.4b): An in-chain periodicity of ~ 8.8 Å along the [$1\bar{1}2$] direction and an intermolecular distance of ~ 4 Å between O atoms of neighboring di-L-Phe molecules. These distances are too large for any type of known direct interaction, such as covalent and hydrogen bonding or even weak electrostatic interactions. In order to explain why the di-L-Phe molecules align into a chain at this large distance, different interaction scenarios have to be assumed, all being characterized not by being direct, but by being mediated by the underlying substrate. It is possible for example, that the adsorption of a di-L-Phe molecule leads to a local reconstruction of the substrate surface, as reported in the case of HtBDC adsorbed to Cu(110) surface [68]. This reconstruction could then influence the adsorption probability over several substrate lattice units, and therefore determines the adsorption site of the neighboring molecules. Instead of a surface reconstruction, a similar effect could be also produced by an adsorption-induced local variation of the electronic properties of the substrate. A similar explanation, based on the creation of charge density waves, has been recently proposed for the formation of supramolecular structures of pentacene on Cu(110) [69]. Finally, the formation of an metal-organic complex, integrating Cu adatoms in the structure of the molecular chains (similar to what has been observed in the case of trimesic acid deposited on Cu(100) [70]), might be able to explain the large in-chain periodicity.

So far, all presented results were obtained on samples onto which the deposition of the molecules and the STM measurements occurred at room temperature. If instead, the samples are annealed to $370 - 380$ K for 1 min after deposition, a second direction of molecular alignment appears, which forms an angle of roughly 105° with the [$1\bar{1}0$] direction (see figure 6.5). This second direction has no direct relation with the previously observed [$1\bar{1}2$] orientation and results from a different adsorption geometry of the molecules within the chains, as well as from a different molecule-molecule separation. This effect can only be observed on relatively few and short chains of figure 6.5 (corresponding coverage $\leq 2\%$).

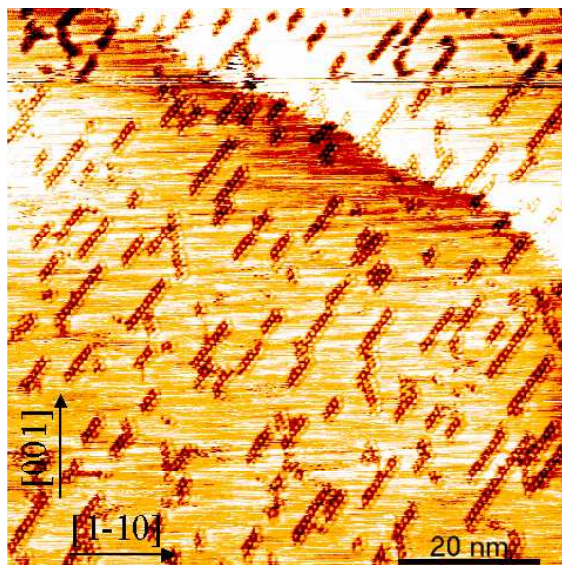At present, the precise origin of this second orientation is not completely clear.

Figure 6.5: Di-L-Phe adsorbed to Cu(110) after post-annealing at $370-380$ K for 1 min. A less dominant second direction of alignment can be observed. The bias voltage and current values applied during STM imaging were -0.6 V and 0.9 nA. The total coverage of the sample is $\sim 13\%$. Image size: 80 nm $\times$ 80 nm.

One could imagine, that in order to bind in this unequal adsorption geometry, a molecule needs to overcome a certain energy barrier, so that this orientation can only occur during annealing. In this case the effect of different annealing times and temperatures should be investigated; such experiments are already under way. In the case of the second direction of orientation, the effect of chirality is also evident, since the mirror symmetric direction, which would be at an angle of about 75° to the [1$\bar{1}$0] direction, is not observed. In order to verify this, further deposition experiments will be performed with the D-D form of the same dipeptide, di-D-Phenylalanine, from which we expect exactly the same scenario presented here, but mirror symmetric. And of course, it would also be interesting to explore the behavior of the D-L and L-D forms of the dipeptide when adsorbed to the Cu(110) single crystal surface.

In conclusion, it has been possible to evaporate di-L-Phe as an intact dipeptide under UHV conditions onto a Cu(110) single crystal surface. STM has been used to characterize the resulting structures, where the formation of chiral di-L-Phe chains was observed. With the help of highly resolved STM pictures, the adsorption of individual dipeptides was found to be chiral. Using these results in combination with

established views on the adsorption geometry of amino acids and small peptides, a model of adsorption was constructed. For the explanation of the intermolecular interactions within the observed single molecular chains, direct molecule-molecule bonding can be excluded, and substrate mediated interactions have to be assumed. By annealing after deposition, a second, less dominant adsorption geometry is obtained.

These results show what a powerful technique is offered by in-vacuo STM investigations. It is possible to gain profound information on the interaction mechanisms between the adsorbed molecules and the underlying substrate as well as among the molecules themselves. This type of investigation will be done on larger biomolecules, as soon as the complete ESI deposition source is fully operational. With increasing intrinsic structural complexity of the analyte via peptides up to proteins, each step in increasing analyte complexity is also a step closer to 'real' biological systems. Sample preparation by means of UHV-ESI deposition, in combination with various ex-situ and in-situ state-of-the-art analysis techniques, will allow to find answers to deep lying questions concerning the relation between the structure of the adsorbate-substrate system and its biological functionality.

Based on the nearly independent contribution of ESI and AFM/STM to their individual research fields, one could guess that the coupling of an ESI-based deposition apparatus for the soft-landing of sensitive analytes with in-situ scanning probe investigations within the highly controlled UHV environment will be an extremely powerful tool.

Chapter 7

Summary and Outlook

During the course of this thesis, a novel ESI deposition source has been developed, assembled, and characterized with respect to its operational principles as well as to the definition of the analyte ion beam. Furthermore, the feasibility of the in-vacuo ESI deposition process has been demonstrated for rather different analytes such as rhodamine 6G and bovine serum albumin. The morphology of the resulting molecular ultra thin films has been examined by means of atomic force microscopy, and the results have been interpreted in terms of the interactions of the single molecules with each other as well as with the different substrates.

Moreover, di-L-Phenylalanine has been adsorbed onto a Cu(110) single crystal surface by means of traditional OMBE. The molecular self-assembly of the adsorbate led to the formation of chiral chains that have been investigated by STM within an UHV environment. This examination was intended to give an example of the same type of investigations that will be done once the UHV-ESI deposition source is fully operational.

In order to link the high vacuum of the TOF-chamber with the UHV of the deposition chamber, a further differentially pumped pressure adjustment chamber in between these vacuum stages is needed (see figure 4.1). When transferring the ions toward the substrate two different solutions of the remaining ion transport question are possible. Either transporting the ions by purely electrostatic means (lenses), focusing and dragging the ion beam through the $\sim$ 2 mm inner diameter orifice of connecting aperture plates, or by another electrodynamic transport (ion guides),

delivering the analyte ions up to the substrate. In both cases, a final electrostatic deceleration right in front of the sample will be necessary in order to accomplish the intended soft-landing of the analyte ions within the UHV environment.

After having achieved this, it will be possible to directly compare the traditional OMBE-based analyte deposition and the novel electrospray deposition technique under identical vacuum conditions as well as with the same adsorbate-substrate combination. Possible analytes could be di-L-Phenylalanine and Trialanine which should be electrosprayable due to their peptide architecture, and which can still be evaporated by thermal means (chapter 6 and [59, 63], respectively).

A new experimental route for the preparation of periodically arranged biological structures will be offered by the electrospray deposition of biological molecules onto patterned substrates that can be prepared by e. g. epitaxial means. A possible experiment could be the electrospray deposition of e.g. BSA onto the epitaxial system Au/Ni(111), which can be exploited in order to pattern the substrate with an island superlattice of monatomic height [46]. During soft-landing of the molecules on the substrate, the protein molecules might prefer to adsorb at the periphery of the trigonal shaped Au islands. Hence, the protein pattern might adapt the periodicity of the substrate. Possible experimental variable parameters are the periodicity of the island superlattice, the temperature of the substrate during deposition, as well as the duration and the ESI deposition rate of the protein.

Recently Z. Ouyang et al. [8] reported about the preparation of protein microarrays by soft-landing of mass-selected ions. By comparing ESI mass spectra recorded during deposition and mass spectra obtained after renewed ESI-MS of the previously deposited analyte material, the authors showed that their deposition process is at least as soft as the ESI-process itself. Moreover, they mentioned that it is still unclear whether the deposited proteins unfold while undergoing 'ionization', mass selection, and soft-landing, and refold again when being solvated, or if they retain their secondary-tertiary structure throughout the whole deposition procedure. In order to answer this fundamental question, it might be helpful to perform systematic studies of various adsorbate-substrate systems, prepared under well defined UHV conditions and examined by means of in-situ AFM/STM measurements, which will be possible

by means of our system.

Furthermore, the controlled serial electrospray deposition of different biological analytes will enable the investigation of biological self-recognition phenomena. In particular, new insights could be developed in the field of protein folding, which is of fundamental importance for the understanding of this building block of life. When dosing ultra clean water onto the sample surface, it should be possible to examine complex biological processes such as the folding and unfolding behavior of proteins within a local environment of increased in-vivo character. It might be possible to examine possible intermediate states of protein configurations as well as their interplay with the surface, as a function of the water coverage.

In conclusion, the softness and the full controllability of the UHV-ESI deposition process will offer unique experimental possibilities. One might foresee that such an ESI-based deposition technique in combination with in-situ scanning probe investigations, will provide a powerful tool for investigations (not only) within the field of biological surface science [1].

Bibliography

[1] B. Kasemo, *Surf. Sci.* **2002**, *500*, 656.

[2] H. Tanaka, T. Kawai, *Surf. Sci.* **2003**, *539*, L531.

[3] W. Kleinkofort, J. Avidiev, B. Brutschy, *Int. J. Mass Spectrom. Ion Proc.* **1996**, *152*, 135.

[4] A. Charvat, E. Lugovoj, M. Faubel, B. Abel, *Eur. Phys. J. D* **2002**, *20*, 573.

[5] M. Karas, F. Hillenkamp, *Anal. Chem.* **1988**, *60*, 2299.

[6] J. B. Fenn, M. Mann, C. K. Meng, S. F. Wong, C. M. Whitehouse, *Science* **1989**, *246*, 64.

[7] R. D. Smith, J. A. Loo, C. G. Edmonds, C. J. Barianaga, H. R. Udseth, *Anal. Chem.* **1990**, *62*, 882.

[8] Z. Ouyang, Z. Takáts, T. A. Blake, B. Gologan, A. J. Guymon, J. M. Wiseman, J. C. Oliver, V. J. Davisson, R. G. Cooks, *Science* **2003**, *301*, 1351.

[9] R. B. Cole, *Electrospray Ionization Mass Spectrometry*, John Wiley & Sons, **1997**.

[10] T. Dülcks, R. Juraschek, *J. Aerosol Sci.* **1999**, *30*, 927.

[11] D. Duft, T. Achtzehn, R. Müller, B. A. Huber, T. Leisner, *Nature* **2003**, *421*, 128.

[12] M. Wilm, M. Mann, *Anal. Chem.* **1996**, *68*, 1.

[13] J. Jeng, J. Shiea, *Rapid Com. Mass Spectrom.* **2003**, *17*, 1709.

[14] A. Jaworek, A. Krupa, *J. Aerosol Sci.* **1999**, *30*, 873.

[15] G. Taylor, *Proceedings of the Royal Society of Londen A* **1964**, *280*, 38.

[16] P. Kebarle, *J. Mass Spectrom.* **2000**, *35*, 804.

[17] R. B. Cole, *J. Mass Spectrom.* **2000**, *35*, 763.

[18] P. Kebarle, M. Peschke, *Anal. Chim. Acta* **2000**, *406*, 11.

[19] M. Gamero-Castaño, *Phys. Rev. Lett.* **2002**, *89*, 147602.

[20] F. J. Higuera, *Phys. Rev. E* **2003**, *68*, 016304.

[21] J. F. de la Mora, *Anal. Chim. Acta* **2000**, *406*, 93.

[22] J. B. Fenn, S. C. Rutan, *Anal. Chim. Acta* **2000**, *406*, 1.

[23] S. L. Kaufman, *Anal. Chim. Acta* **2000**, *406*, 3.

[24] T. L. Constantopoulos, G. S. Jackson, C. G. Enke, *Anal. Chim. Acta* **2000**, *406*, 37.

[25] G. Wang, R. B. Cole, *Anal. Chim. Acta* **2000**, *406*, 53.

[26] M. Gamero-Castaño, J. F. de la Mora, *Anal. Chim. Acta* **2000**, *406*, 67.

[27] M. Labowsky, J. B. Fenn, J. F. de la Mora, *Anal. Chim. Acta* **2000**, *406*, 105.

[28] G. Cooks, R. Caprioli, *J. Mass Spectrom.* **2000**, *35*, 761.

[29] G. J. V. Berkel, *J. Mass Spectrom.* **2000**, *35*, 773.

[30] M. Gamero-Castaño, J. F. de la Mora, *J. Mass Spectrom.* **2000**, *35*, 790.

[31] R. Juraschek, F. W. Röllgen, *Int. J. Mass Spectrom.* **1998**, *177*, 1.

[32] G. Scoles, *Atomic and Molecular Beam Methods*, Oxford University Press, **1988**.

[33] C. M. Lock, E. W. Dyer, *Rapid Com. Mass Spectrom.* **1999**, *13*, 422.

[34] P. H. Dawson, *Quadrupol Mass Spectrometry*, Elsevier Scientific Publishing Company, **1976**.

[35] J. F. O'Hanlon, *A User's Guide to Vacuum Technology*, John Wiley & Sons, **1989**.

[36] P. Milani, S. Iannotta, *Cluster Beam Synthesis of Nanostructured Materials*, Springer Verlag, **1999**.

[37] J. Mathews, R. L. Walker, *Mathematical Methods of Physics*, Addison-Wesley Publishing Company, **1970**.

[38] D. A. Dahl, *Simion 3D Version 7.0 User's Manual*, Idaho National Engineering and Envirionmental Laboratory, **2000**.

[39] S. Rauschenbach, *private communication*, **2004**.

[40] T. Peters, *All about Albumin: Biochemistry, Genetics, and Medical Applications*, Academic Press, **1996**.

[41] A. A. Spector, *Journal of Lipid Research* **1975**, *16*, 165.

[42] R. Kurrat, J. E. Prenosil, J. J. Ramsden, *J. Colloid. Interf. Sci.* **1997**, *185*, 1.

[43] O. Mori, T. Imae, *Colloid. Surface. B* **1997**, *9*, 31.

[44] A. P. Quist, L. P. Björck, C. T. Reimann, S. O. Oscarsson, B. U. R. Sundqvist, *Surf. Sci.* **1995**, *325*, L406.

[45] A. S. Paulo, R. Garcia, *Biophysical Journal* **2000**, *78*, 1599.

[46] H. Brune, C. Ramainczyk, H. Röder, K. Kern, *Nature* **1994**, *369*, 469.

[47] H. Brune, *Surf. Sci. Rep.* **1998**, *31*, 121.

[48] A. N. Verentchikov, W. Ens, K. G. Standing, *Anal. Chem.* **1994**, *66*, 126.

[49] K. Bromann, H. Brune, C. Félix, W. Harbich, R. Monot, J. B. Buttet, K. Kern, *Surf. Sci.* **1997**, *377-379*, 1051.

[50] D. C. Carter, J. X. Ho, *Adv. Protein Chem.* **1994**, *45*, 153.

[51] T. Peters, *Adv. Protein Chem.* **1985**, *37*, 161.

[52] T. C. Ta, M. T. McDermott, *Colloid. Surface. B* **2003**, *32*, 191.

[53] P. M. Harrison, P. Arosio, *Biochimica et Biophysica Acta* **1996**, *1275*, 161.

[54] I. Yamashita, *Thin Solid Films* **2001**, *393*, 12.

[55] E. Mayes, A. Bewick, D. Gleeson, H. Hoinville, R. Jones, O. Kasyutich, A. Nartowski, B. Warne, J. Wiggins, K. K. W. Wong, *IEEE Transactions on magnetics* **2003**, *39*, 624.

[56] J. Williams, S. Haq, R. Raval, *Surf. Sci.* **1996**, *368*, 303.

[57] A. Kühnle, T. R. Linderoth, B. Hammer, F. Besenbacher, *Nature* **2002**, *415*, 891.

[58] I. Stensgaard, *Surf. Sci.* **2003**, *545*, L747.

[59] S. M. Barlow, S. Haq, R. Raval, *Langmuir* **2001**, *17*, 3292.

[60] Z. Takats, S. C. Nanita, R. G. Cooks, G. Schlosser, K. Vekey, *Anal. Chem.* **2003**, *75*, 1514.

[61] C. Pepe, S. Rochut, J.-P. Paumard, J.-C. Tabet, *Rapid Com. Mass Spectrom.* **2004**, *18*, 307.

[62] S. D. Fuerstenau, W. H. Benner, *Angew. Chem. Int. Ed.* **2001**, *40*, 541.

[63] S. M. Barlow, R. Raval, *Surf. Sci. Rep.* **2003**, *50*, 201.

[64] L. Stryer, *Biochemie*, F. Vieweg & Sohn, **1983**.

[65] T. Classen et al., to be published.

[66] M. Böhringer, W.-D. Schneider, R. Berndt, K. Glöckler, M. Sokolowski, E. Umbach, *Phys. Rev. B* **1998**, *57*.

[67] M. O. Lorenzo, C. J. Baddeley, C. Muryn, R. Raval, *Nature* **2000**, *404*, 376.

[68] M. Schunack, L. Petersen, A. Kühnle, E. Lægsgaard, I. Stensgaard, I. Johannsen, F. Besenbacher, *Phys. Rev. Lett.* **2001**, *86*, 456.

[69] S. Lukas, G. Witte, C. Wöll, *Phys. Rev. Lett.* **2002**, *88*, 028301.

[70] N. Lin, A. Dmitriev, J. Weckesser, J. V. Barth, K. Kern, *Angew. Chem. Int. Ed.* **2002**, *41*, 4779.

Danksagung

Zum Schluß möchte ich mich bei allen ganz herzlich bedanken, die direkt oder indirekt zum Gelingen dieser Arbeit beigetragen haben:

Vielen Dank an Herrn Prof. Dr. Klaus Kern für die interessante Aufgabenstellung, sowie die Möglichkeit mich in seiner Abteilung auf die Promotion vorbereiten zu dürfen. Den Teamgeist innerhalb der Abteilung für Nanowissenschaften gilt es besonders hervorzuheben.

Da ohne funktionierende Infrastruktur vor Ort eine derartige Entwicklungs- und Aufbauarbeit nicht zu bewerkstelligen ist, sei an dieser Stelle stellvertretend für ihre Mitarbeiter, Hr. Frey (Mechanische Werkstatt), Hr. Bleder (Eletronik), Hr. Wendel (Kristallpräparation), Hr. Dr. Habermeier (Technologie) und Hr. Kammerlander (Glastechnik) für ihre unkomplizierte Zusammenarbeit gedankt.

Ein herzlicher Dank an Dr. Giovanni Costantini für seine Unterstützung sowie sein Engagement, vor allem in der Schlußphase, in der er sich mit dem Bleistift bewaffnet durch die noch unfertige Doktorarbeit gekämpft hat.

Dr. Anatoly Verentchikov und Dr. Sergei Koltsov (Institut für analytische Instrumentierung, Russische Akademie der Wissenschaften, St. Petersburg) möchte ich für ihren Wissenstransfer im Rahmen unserer Zusammenarbeit danken. Ein besonderer Dank gebührt Dr. Sergei Koltsov, für die vielen Stunden, die wir gemeinsam an der Apparatur verbracht haben.

Bei Dr. Marco Burghard möchte ich mich dafür bedanken, das DI AFM jederzeit benutzen zu dürfen. Dr. Eugenio Lunedei sei für das Erstellen der Datenerfassungssoftware gedankt. G. Huber (Abteilung Prof. Dosch, Max-Planck-Institut für Metallforschung, Stuttgart) möchte ich für die Messungen am JPK AFM danken. Ein herzliches Dankeschön geht an Dr. Mato Knez für seine Unterstützung bei den

104

Curriculum Vitae

3. April 1973   Geburt in Ichenhausen, Deutschland.

1979 - 1983   Besuch der Grundschule in Harburg

1983 - 1985   Besuch des Gymnasiums in Donauwörth.

1985 - 1989   Besuch der Knabenrealschule Heilig Kreuz Donauwörth.

1989 - 1991   Besuch der Hans-Leipelt-Fachoberschule Donauwörth.

1991 - 1992   Studium der Physikalischen Technik an der
Fachhochschule München.

1992 - 1995   Studium der Physik an der Universität Augsburg.

1995 - 1998   Studium der Physik an der Universität Würzburg.

1999 - 2000   Wissenschaftlicher Mitarbeiter bei Prof. Dr. K. Kern
an der ETH Lausanne.

2000 - 2004   Wissenschaftlicher Mitarbeiter sowie Anfertigung der
vorliegenden Dissertation bei Prof. Dr. K. Kern am
Max-Planck-Institut für Festkörperforschung in Stuttgart.